MECHANICS OF ACCELERATED AUTOGENOUS HEALING OF CONCRETE WATER DISTRIBUTION SYSTEMS DAMAGED BY CRACKING AND DECALCIFICATION

A Dissertation

by

JEFFRYD ROSE LIVINGSTON ROSE

Submitted to the Office of Graduate and Professional Studies of
Texas A&M University
in partial fulfillment of the requirements for the degree of

DOCTOR OF PHILOSOPHY

Chair of Committee	Zachary Grasley
Co-Chair of Committee	Anol Mukhopadhyay
Committee Members	Marcelo Sanchez
	Sara Abedi
Head of Department	Robin Autenrieth

May 2018

Major Subject: Civil Engineering

ABSTRACT

The research discussed herein contains details about exploring a method for healing damaged drinking water pipe distribution systems. Two types of damage in the systems were considered, namely cracking and decalcification. Radial permeability of the pipes was considered as the metric to measure the damage in the pipe systems. Highly scaled down miniaturized samples were used to study the effects. The effects of different types of flow in the permeability measurement were studied first. The difference in the types of permeability measurement, namely poromechanical method (Hollow Dynamic Pressurization) and accelerated flow through method (Radial Flow Through), showed that for cement paste having a unimodal pore network there is no measured difference. For materials with multimodal pore network distribution, namely cement mortar and concrete, there is a significant difference in permeability measurement between the two methods. The Radial Flow Through measures the flux of fluid across the cross-section of a material while the Hollow Dynamic Pressurization measures the flux of fluid *into* the smallest pore network of the material. Thus, the Radial Flow Through is primarily influenced by the largest pores in the cross section while the smaller pores primarily influence the Hollow Dynamic Pressurization. The Radial Flow Through method was chosen as the testing method for damage caused by cracking and Hollow Dynamic pressurization was chosen as the method for measuring permeability in damaged specimens caused by decalcification.

The hollow cylindrical pipe section specimens were damaged in a controlled manner by cracking and decalcification. The damaged samples were healed by a healing solution that was seeded with calcium and carbonate ions to help accelerate the autogenous healing process in the samples. The

effect of the healing was determined by measuring the permeability of the samples before and after healing. The results showed a permeability decrease of up to a factor of 4 for decalcified samples and up to a factor of 12.5 in the case of cracked samples. It was also determined that permeability loss due to cracking was significantly higher that caused by decalcification. The healed samples were imaged using X-ray Computed Tomography to provide more details of the healing precipitation. The resulting images were too sensitive to thresholding effects to provide a clear result. Scanning Electron Microscope assisted Energy Dispersive Spectroscopy was used to isolate the precipitation location of the healing precipitates in the samples. The precipitation was primarily determined to be present along the inner surface of the hollow cylindrical pipe section specimen covering up the crack mouth of the damaged specimen and healing the sample.

ACKNOWLEDGEMENTS

I would like to thank my committee chair, Dr. Zachary Grasley for his support, guidance, advice, and patience in my work. He enabled my creativity to flourish and helped me nurture my ideas and convert them in to interesting results. I would like to thank my committee co-chair, Dr. Anol Mukhopadhyay for encouraging my random ideas and helping me facilitate fulfill them. I also thank my committee members Dr. Sara Abedi and Dr. Marcelo Sanchez for their support and encouragement.

I would like to thank my friends and colleagues in the department. My friends were a constant form or support for my work and a great source of help when I needed it the most. My colleagues in the department played a vital role in ensuring the entire process for my research went smoothly without any glitches. I would like to tank Ms. Laura Byrd from the graduate office for putting up with my never-ending stream of questions and making sure that I followed all the procedures and paperwork that were needed for the program and for my research.

Finally, I thank my family for being the rock of stability and support without whom I would not have been able to complete this endeavor. My parents, who encouraged me to always pursue my dreams without questioning my choices, let me become the engineer that I am today. My sister, for always being there to support me for my choices and to keep reminding me that I have a target that I needed to achieve.

CONTRIBUTORS AND FUNDING SOURCES

Contributors

This research was conducted under the supervision of an advising committee consisting of Professors Dr. Zachary Grasley, Dr. Anol Mukhopadhyay and Dr. Marcelo Sanchez from the Civil Engineering department and Professor Dr. Sara Abedi from the Petroleum engineering department.

Dr. Marc Edwards of Civil Engineering from Virginia Tech provided the healing solutions used in this research mentioned in Table 6. Dr. Kai Wei Liu from Civil Engineering at Texas A&M helped perform all the X-ray CT scanning and imaging used for the research. Ignacio Rodriguez of University of Chile helped me setup the controlled cracking experiments. Use of the Texas A&M Materials Characterization Facility is acknowledged. All other work was performed independently by the student.

Funding Sources

This research was supported by the National Science Foundation under grant number 1336616. Any opinions, findings, and conclusions or recommendations expressed in this material are those of the author(s) and do not necessarily reflect the views of the National Science Foundation.

TABLE OF CONTENTS

LIST OF TABLES

LIST OF FIGURES

Page

1 INTRODUCTION

1.1 Problem statement

A significant fraction of the United Stated potable water distribution system is on the verge of failure and needs immediate attention and represents one the most urgent societal infrastructure challenges. Conventional repair involves removing pipes from service to access them for relining or replacement. But in some situations, repair and replacement is very difficult, for instance, with some pipes buried 300-1500 feet deep, and there is also widespread interest in new and transformative methods of extending the lifetime of pipelines or preventing their degradation in the first place.

Concrete is second most used material in the world after water. Use of concrete in water distribution systems can be dated to 1st century AD by the Roman empire[1]. The technology was lost in the middle ages and gained immense popularity in the early 20th century. Concrete by itself is not completely impervious to water as 100% water tightness cannot be achieved due to the porous nature of concrete. The permeability of concrete is low enough that the amount of water leaking through a concrete pipe is negligible. The assumption holds true in a perfect world scenario where the concrete is free from cracking and weathering actions. Concrete is a very brittle material that is strong in compression and weak in tension. The design of any structural members has to take into account for multiple modes of failure and to design every structure to take only compression loads would not be economically feasible. Therefore, concrete members have to be designed to withstand tensile forces too.

Adding steel reinforcement to concrete alleviates the problem of bearing the tensile stresses in the member. However, the design philosophy behind adding steel reinforcement is allowing the concrete to crack under the tensile forces and allowing the reinforcement to carry the tensile forces after the concrete is damaged. This design philosophy works great for high load bearing members where the reinforced concrete member carries the brunt of the load. The members include beams, columns, slabs, and footing and mats for foundations. Reinforced concrete is also very commonly used in water distribution systems that span over hundreds of miles as it is significantly cheaper to the alternative piping systems that could be used.

Cracks are unavoidable in reinforced concrete structures, as the design method itself assumes that cracking will occur. Once cracks start to form in concrete the permeability of the pipe increases significantly, which has been corroborated by previous work done in the area [2-5]. This problem is severely exacerbated when the cracking occurs in concrete pipe systems. There are several common causes for the formation of cracks in reinforced concrete pipe systems. Bending stresses, thermal stresses, shrinkage stresses and stresses induced due to concrete creep are the most important sources for tensile stresses which induce cracking in concrete pipe systems. The effect of cracked pipes in a drinking water distribution system is twofold. Firstly, there is a significant amount of loss of drinking water that leaks out of the pipes due to the increased permeability of the concrete pipe systems. Secondly if the pipe system is laid in regions where the soil surrounding the concrete pipes contain harmful chemicals there is a chance of the chemicals infiltrating the drinking water.

The basic microstructure of concrete is made up of two major phases of hydration products calcium silica hydrate (C-S-H) and calcium hydroxide (C-H). C-S-H is a porous amorphous phase that is held together by Wan-der-Waals forces contributing to the load bearing strength of portland cement concrete. C-H is a crystalline phase that acts like a filler material which fills up the spaces left in the cement matrix. C-S-H alone is a phase that has high water permeability. The packing of C-H phases in the pore network causes the permeability of the matrix to go down significantly to the point where concrete can be considered an impermeable substance for all practical purposes. C-H phase acts like a seal for the concrete. Calcium hydroxide is soluble in water, so in a water distribution system comprised of concrete pipe systems the water flowing through the pipes will dissolve the C-H phase. Over the course of the life of a water distribution system C-H is slowly leached out of the concrete and thereby creating scenario where the seal is corroded away over time. The loss of C-H phase in concrete increases the permeability[6] of the concrete pipes and compounds to the water leakage problem observes in concrete pipe systems. This effect of leaching C-H phase over a sustained duration is called decalcification of concrete. Decalcification increases permeability of concrete exponentially as C-H is dissolved by water, pores are opened up in the matrix and more C-H is exposed to further decalcification effects. Eventually this leads to problems with the structural integrity of the concrete too.

In a concrete pipe water distribution system, the leaks start as soon as the cracks start to form due to the tensile stresses. As time goes on decalcification starts becoming prominent as the pore network becomes more accessible to the water that is flowing through the pipe. This increases the permeability of the water flowing through the walls of the pipe. As the C-H phase is depleted the structural integrity of the concrete matrix phase is also affected leading to more cracking.

1.2 Scope of dissertation

From an economic standpoint it would be desirable to be able to repair concrete pipes in water distribution systems without having to excavate buried pipes or replace pipe sections that have been deemed as damaged. The primary objective of this dissertation is to investigate the viability of a method to rapidly repair damage of concrete pipes in water distribution systems without having to access the damaged region. The next objective would be to determine if the method could be used without interrupting the water supply that is the functional purpose of the pipes in question. To be able to achieve the above stated objectives the repair process must be able seal cracks that form in the concrete water distribution pipes and be able to fill up holes caused by the decalcification process.

Self-healing of concrete has become prominent with the development of various biomineralization and chemical methods where bacteria and chemicals are embedded into fresh concrete and are used to heal the concrete that gets damaged. Autogenous healing of concrete is another repair technique which uses the intrinsic properties of concrete to heal itself with water exposure over a long period of time. Self-healing techniques remove the need for human interaction with the damaged water distribution system made of concrete pipes. There were several steps needed to investigate the viability of the technique.

The first step is to determine an effective way to quantify damage in the concrete caused by cracking and decalcification. Concrete that has been damaged has vastly different physical properties compared to undamaged concrete. Damaged concrete has lower strength, modulus, and

transport properties. Measuring transport properties as a metric for damage would be ideal for this study. As damage increases permeability of concrete increases therefore permeability will be used as the metric to quantify damage. Direct permeability testing for 28-day old concrete is a very long process. To accelerate the process, first the specimens used for the study are scaled down versions to facilitate faster testing of permeability. This can be done by making cement mortar pipe sections specimens and testing for their water permeability. Secondly innovative methods to test for permeability that would significantly reduce the time taken for the test process would be employed. The second step would be to induce controlled damage in the pipe section specimens by inducing controlled cracks and controlled decalcification in the specimen. Work done in previous research have discovered ways to induce controlled cracking and accelerated decalcification in portland cement concrete materials. Choosing the best method would depend on the repeatability and stability of the specimens damaged. The permeability of the sections would be measured before and after the damage. The most severe damage level that could be simulated in the controlled damaged process without compromising the stability of the specimen would be would be used for the healing purposes.

The third step would be to induce healing without having to repair with external aids. The method used would have to work on pipe section specimens without disrupting the function of the pipes or with very minimal disruption. Another important factor for the healing method is it should be an economically better option to having the pipes replaced or excavated and repaired. The method to repair/heal the damage would be tested on the damaged pipe section specimens that haven been exposed to controlled cracking and controlled decalcification. The healed specimens would be then

tested for permeability to see if the healing process reduced the permeability. Loss of permeability would be used a quantitative measurement for the effect of the repair process.

The final step would be to use imaging and surface analysis techniques to verify the effectiveness and the mechanism behind the healing process. X-ray computed micro-tomography analysis will be performed on cracked samples before and after the healing process to observe changes that have occurred in the crack regions. Scanning electron microscopy will be used in tandem with energy dispersive spectroscopy to identify areas of precipitation of healing precipitates or coatings in the cracked regions to identify the mechanism behind the healing process.

The primary contributions of research towards this dissertation are summarized as follows:

- Expanded upon previous research on poromechanical methods to identify the mechanics involved in using those methods for determining the permeability of cement-based materials
- Determined the specific conditions for permeability measurement where poromechanical methods are preferred and the specific conditions for permeability measurement where conventional flow methods are preferred.
- Determined the effect of accelerated decalcification towards its contribution for permeability gain on cement mortar specimens
- Determined that by seeding calcium and carbonate ions into water flowing through a hollow mortar pipe section specimen it is possible to accelerate precipitation of calcite crystals on the inner surface of the pipe.

- Determined that accelerated autogenous healing is an effective method in reducing permeability of damaged cement mortar pipe sections for damage caused by both cracking and decalcification.
- Determined that the coating of calcite is too thin to be visible on X-ray computed micro-tomography images of healed pipe sections.
- Determined the mechanism of calcite coating on cracked pipe sections using Scanning electron microscope assisted electron dispersive spectroscopy.

2 LITERATURE REVIEW

This chapter will discuss research that has been already completed and provides the knowledge base for the background information for the topics related to the dissertation. The major topics covered in this literature review include - self-healing concrete, autogenous healing of concrete, accelerated decalcification methods, concrete permeability measurement, dynamic pressurization technique, radial flow through technique, X-ray Computed Tomography, and Scanning Electron Microscope – Energy Dispersive Spectrometry (SEM-EDS).

1.1 Self-healing concrete

Self-healing in concrete was first reported in 1836 in the French Academy of Science. Self-healing in concrete is achieved using, chemical or biological, reagents in concrete [7-14]. The biological or chemical components are packed in capsules and placed into the concrete when pouring. Concrete is a brittle material and weak in tension therefore when tensile forces are applied on the concrete cracking occurs. When cracking occurs, the capsules containing the chemical or biological reagents are broken apart and the components within them released as shown in Figure 1. The reagents are designed in such a way that they will react with water and air entering the cracked region. The components react with the surroundings and deposit chemicals which act as a binder or sealant in the damaged regions of the concrete.

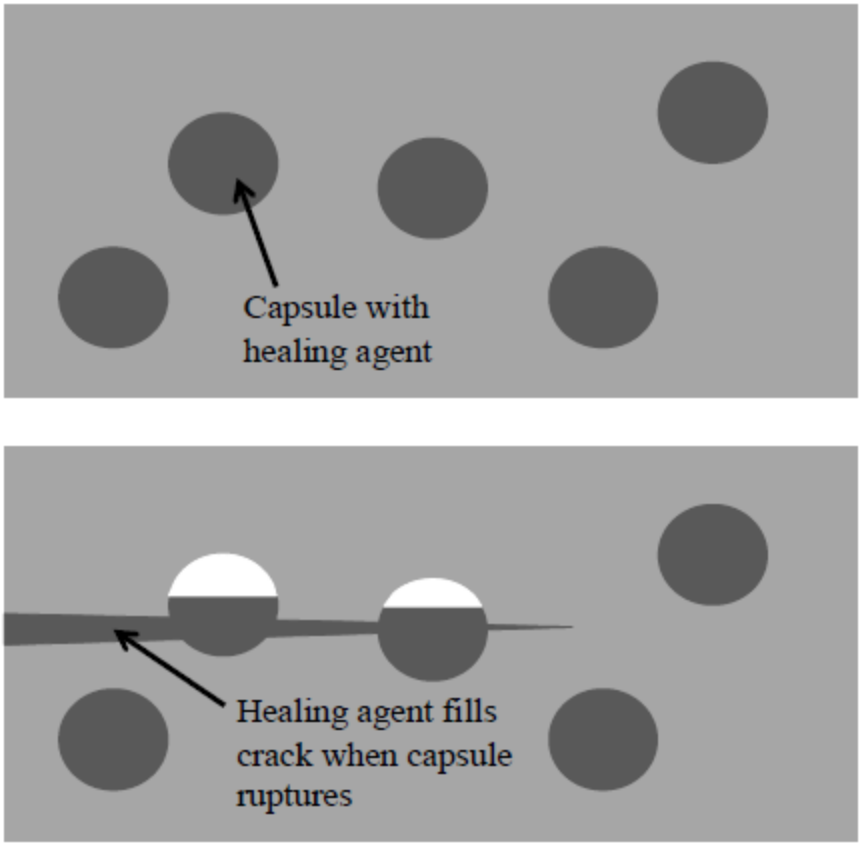

Figure 1 – Schematic of self-healing in concrete. Capsules containing healing agents are placed into concrete and cracks cause the capsules to rupture which in turn activates the healing agents and fill up the cracks reprinted from [13].

Mineral producing bacteria is one of the most common techniques used for healing concrete. One of the ways to achieve self-healing is by using biomineralization bacteria. Biomineralization is the process in which living organisms are used to produce mineral deposits when exposed to certain conditions. The effect of biomineralization bacteria on healing effect in damaged concrete has been explored extensively in previous research [13, 15-19]. The result of biomineralization is precipitation of relatively inert solids such as calcium carbonate in the damaged areas of the

concrete thereby healing the concrete[7, 20]. Biomineralization bacteria are a promising self-healing option for newly laid concrete pipes.

Bacterial spores are sealed into capsules and placed into the concrete when the concrete is poured. As the concrete cracks, the capsules are broken and as water reaches the spores they are activated. The bacteria act as a catalyst and result in the formation of calcium carbonate, which is a great filler material to seal up cracks and holes in the concrete microstructure as shown in Figure 3.

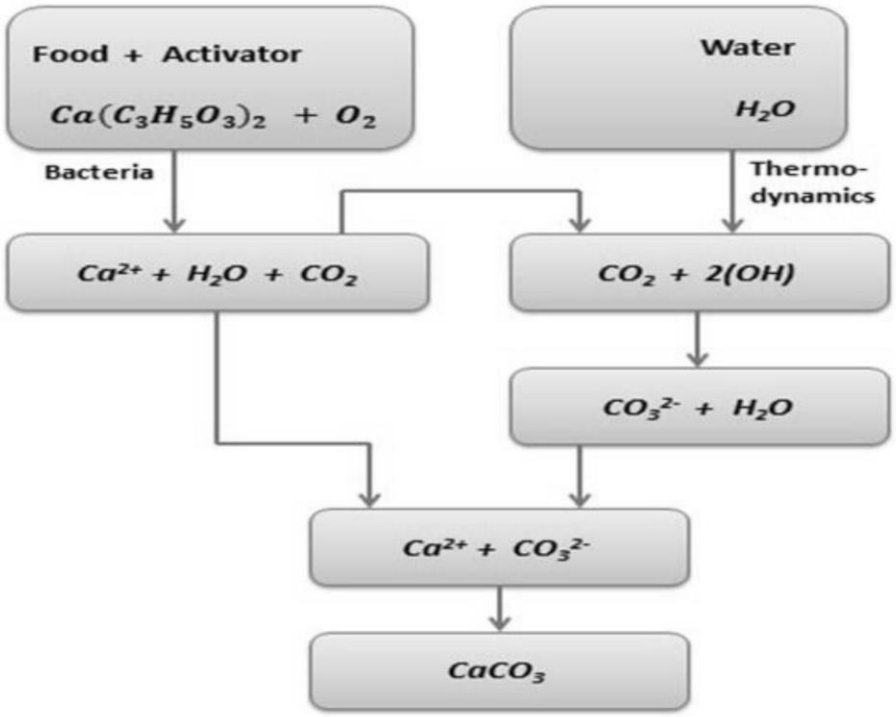

Figure 2 – Flow chart of reaction kinetics of bacterial activated self-healing concrete. Bacteria gets activated and in the presence of water that reaches it through the cracks in concrete reacts to form calcium carbonate precipitates reprinted from [21].

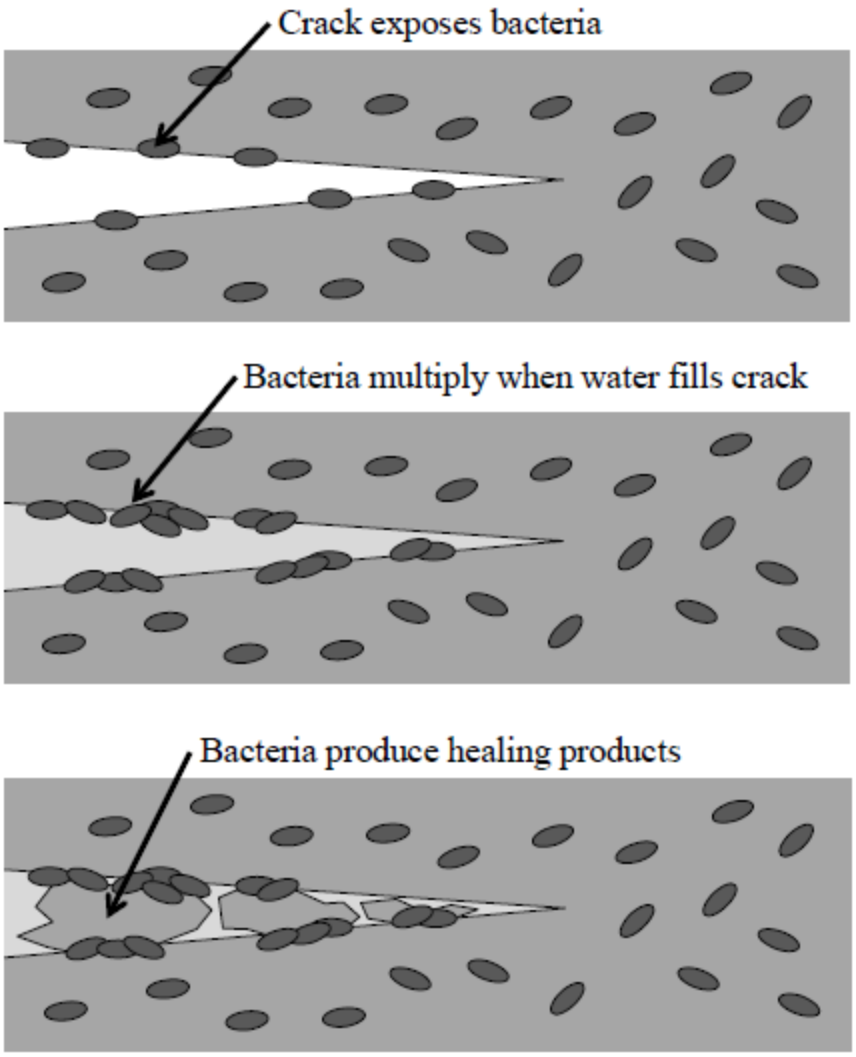

Figure 3 – Bacterial Self-healing schematic, bacteria gets activated when water fills cracks and they multiply and deposit calcium carbonate as a result of their metabolic activities sealing cracks reprinted from [13].

Chemical agents released from the capsules seal cracks in case of chemical method. The chemicals used vary from swelling geo materials and expansive agents that precipitate calcium carbonate as shown in Figure 4.

The self-healing methods work only when the healing reagents are placed in concrete when casting and are not applicable in existing concrete.

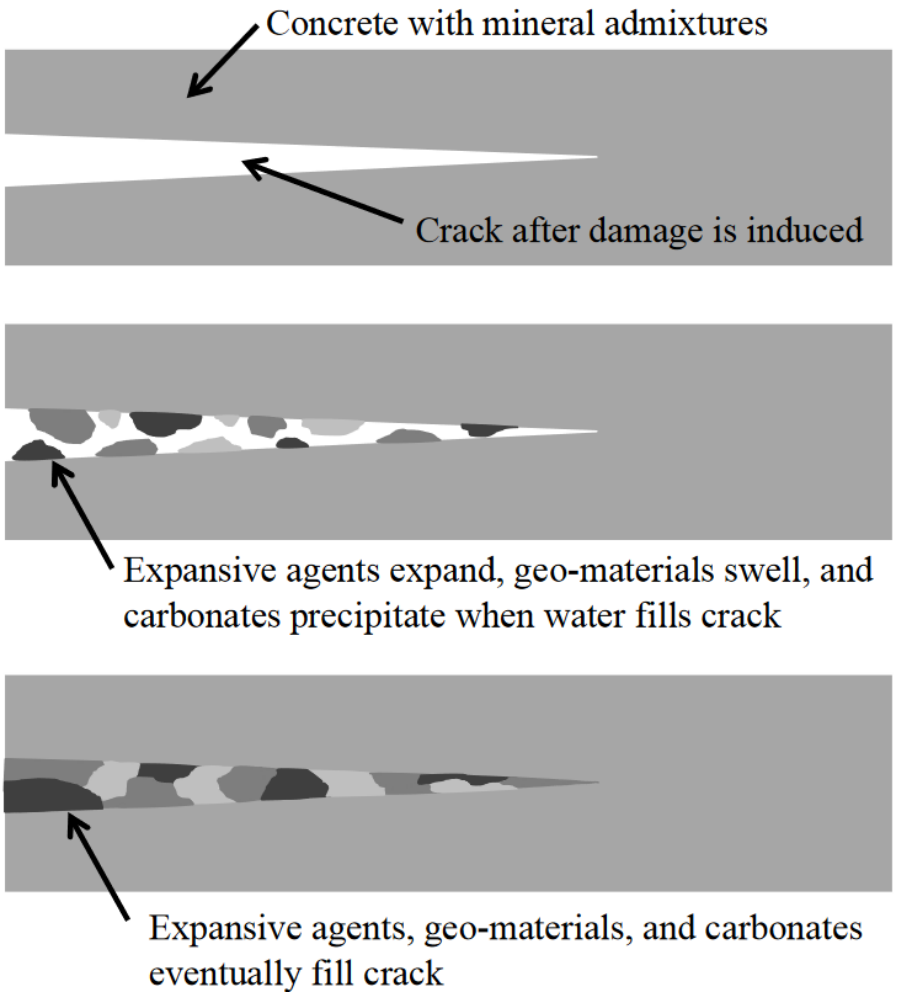

Figure 4 – Chemical Self-healing schematic, swelling geo materials and expansive agents that precipitate calcium carbonate when water fills cracks reprinted from [13].

2.1 Autogenous healing

Autogenous healing of concrete is a natural process in which cracked concrete is exposed to water that deposits calcium carbonate (CaCO3), essentially sealing the crack after long periods of exposure. Autogenous healing is possible due to the reaction between calcium hydroxide and carbon dioxide resulting in the formation of calcium carbonate. The calcium carbonate formed is deposited on the concrete surface and eventually after many layers of deposition it hardens up enough to form a protective seal on the concrete.

Figure 5 – White calcium carbonate traces at concrete surface, indicating autogenous healing of cracks reprinted from [22].

There are several conditions required for active autogenous healing reaction to occur. It requires constant supply of carbon dioxide and calcium hydroxide.

In damaged concrete systems the cement hydration provides the calcium hydroxide. Calcium hydroxide is one of the primary products of cement hydration and is always available in plenty for the reaction to occur. Carbon dioxide is supplied to the reaction by water flowing through the cracks. Water contains dissolved carbon dioxide and it reacts with the calcium hydroxide to form calcium carbonate.

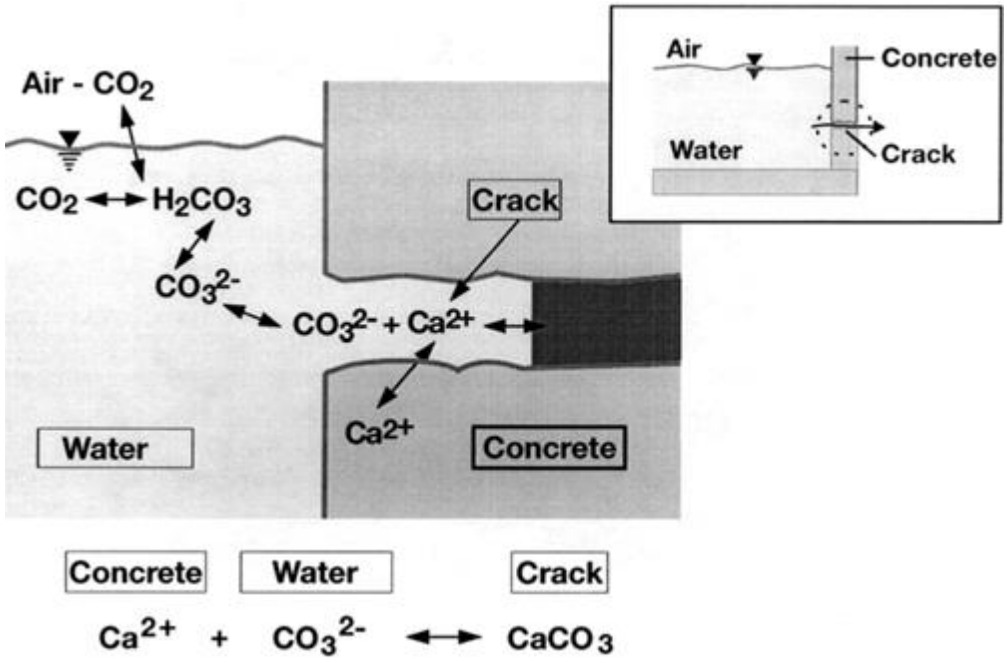

Figure 6 – The kinetics of the autogenous healing reaction is explained in the above figure. Carbon dioxide from the air dissolves in water and reacts with the calcium hydroxide in the hydrated cement. The reaction produces calcium carbonate which is precipitated in the cracks and crevices that water can reach in the concrete reprinted from [22].

The earliest modern study about autogenous healing of materials dates back to 1925 [23] and was expanded upon by the studies made by several concrete researchers and expanding upon our knowledge in the field [8, 22, 24-26]. Since then several attempts have been made to study the effects of autogenous healing of cracked concrete and its effect of the physical properties of concrete [9, 25, 27]. The healing effects are particularly useful in water distribution systems where you have a constant supply of water to help provide the carbon dioxide supply to the cracked in the cracks and crevices. Thereby allowing the healing reaction to occur continuously and letting calcium carbonate precipitate in the cracks and crevices.

Autogenous healing of concrete takes a significant amount of time before the results are evident. Previous work done on the subject of autogenous healing shows that the process can be accelerated by altering the water chemistry[28, 29]. The process designed to accelerate the precipitation involves adding chemical salts into the water distribution system and allowing the salts to react in water forming calcium carbonate. Essentially the process of acceleration involves supersaturating the water flowing through the pipes with calcium carbonate to clog the microscopic leaks in the concrete. Supersaturated calcium carbonate has a higher chance of getting precipitated and deposited in the damaged areas of the concrete. The characteristic diameter of leaks is in the 10-20 μm range, and the precipitated calcium carbonate will reduce the size of these holes and thereby reducing the leaking of the pipes.

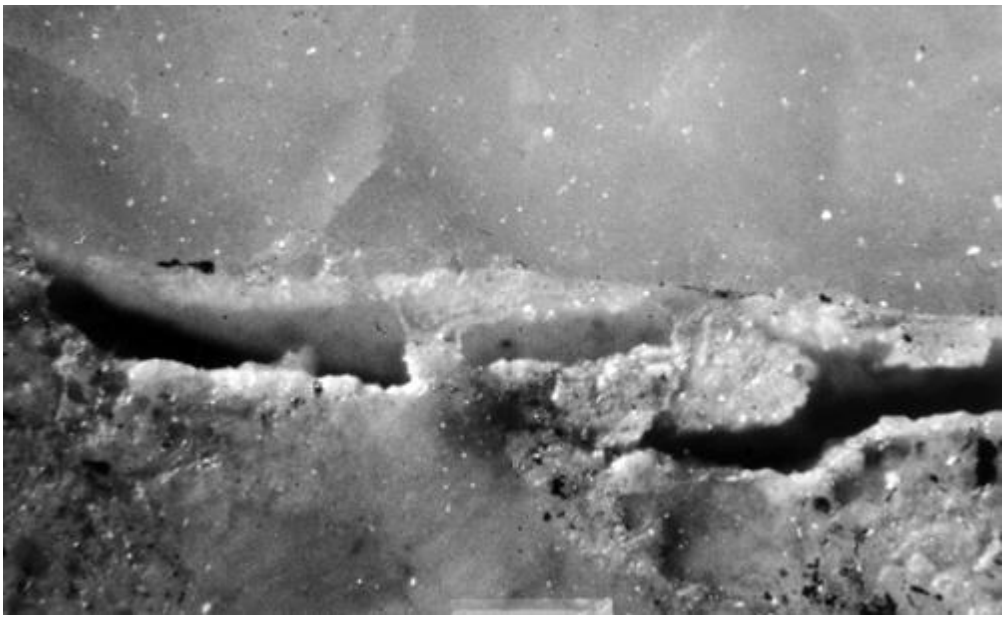

Figure 7 – A crack section 20 μm wide that is getting healed with the deposition of calcium carbonate precipitates from autogenous healing of concrete reprinted from [22].

2.2 Decalcification

The binder part of concrete, hydrated cement, is primarily comprised of two hydration products calcium silica hydrate (C-S-H) and calcium hydroxide (C-H). The C-S-H is an amorphous phase which provides strength to the concrete and helps with the load bearing properties. The C-S-H phase has an undefined stoichiometry and is made up of a distributed pore network in the form of capillary pores and gel pores. The porous nature of C-S-H reduces its ability to provide significant resistance to transport of fluids across its volume in hydrated cement.

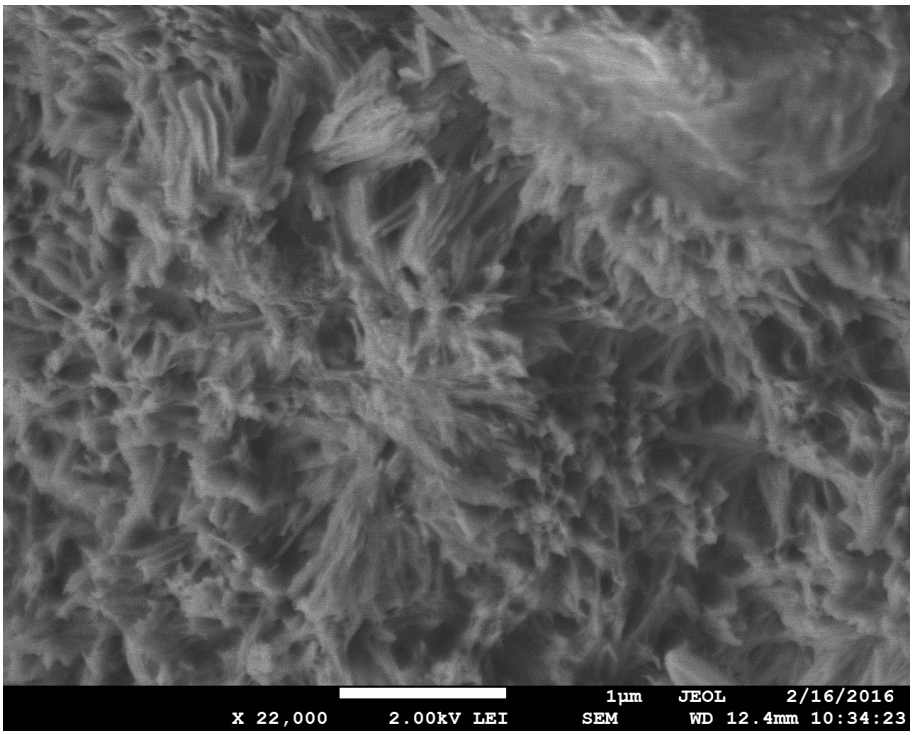

Figure 8 – Hydrated cement paste viewed under a scanning electron microscope showing the porous nature of the amorphous C-S-H phase

The C-H phase is a crystalline phase found in hydrated cement. C-H phase doesn't provide any significant help in load bearing capacity of hydrated cement, but it fills up the capillary pores between the C-S-H particles. Thereby, C-H directly contributes in increasing the resistance to transport of fluids across the hydrated cement and provides the low permeability that concrete has. The CH phase crystals are hexagonal in structure and tend to grow around the capillary pores surrounding the C-S-H regions of hydrated cement.

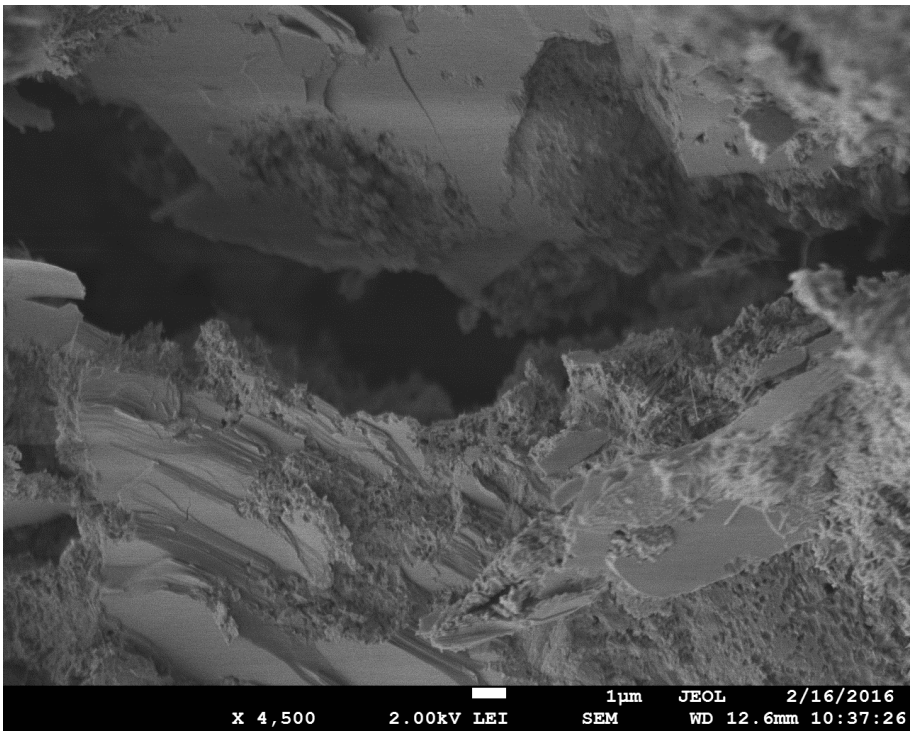

Figure 9 – Hydrated cement paste viewed under scanning electron microscope showing the crystalline C-H phase.

The C-H phase is soluble in water therefore permeability of concrete can be increased by dissolving the C-H particles. The effect of dissolution of the calcium hydroxide in concrete is called decalcification or leaching of concrete. The effect of decalcification on the transport properties and durability of concrete has been studied in detail in several previous researches done on this topic [30-35]. Figure 10 shows a simple Schematic of leaching kinetics of a porous material showing how an aggressive solution can cause the diffusion of a soluble material from the porous material outwards to the solution[36].

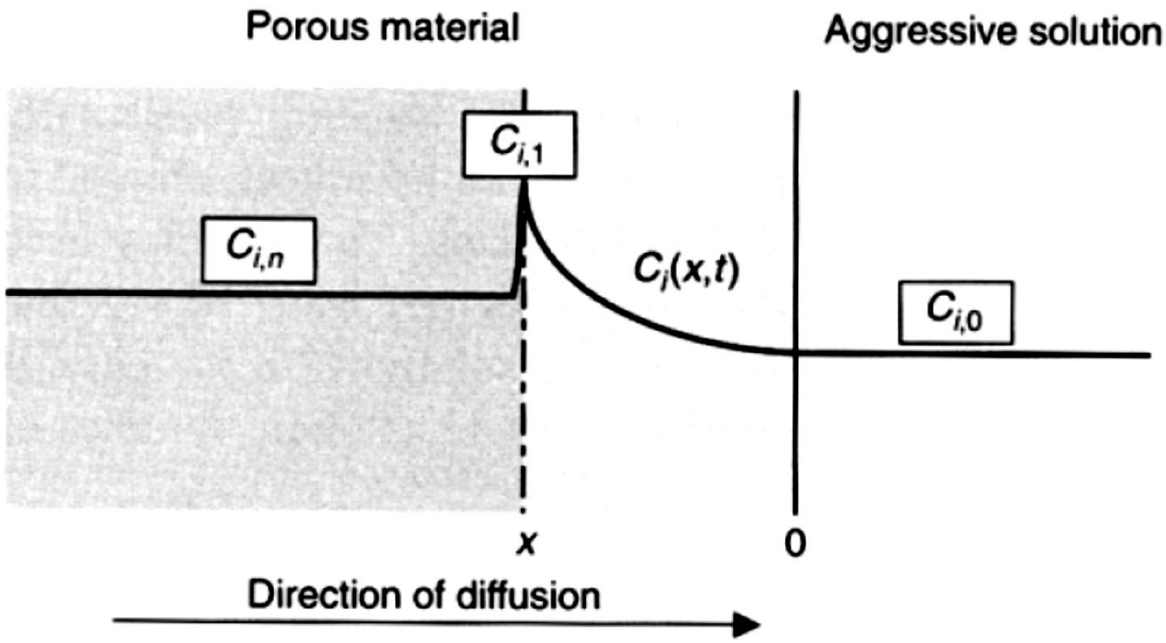

Figure 10 – Schematic of leaching kinetics of a porous material showing how an aggressive solution can cause the diffusion of a soluble material from the porous material outwards to the solution reprinted from [36].

2.2.1 Accelerated decalcification

Decalcification is a very slow process and takes years to fully impact a concrete water distribution system. To fully examine the effects of decalcification the mortar specimens used in this study were subject to accelerated decalcification in a controlled environment. Work done by Carde et al 1997 and Gerard et al in 2002 show that the leaching process can be accelerated significantly by exposing concrete to 6M ammonium nitrate solution. [32, 36]. The reaction equation is shown in (1).

$$Ca(OH)_2 + 2NH_4NO_3 \rightarrow Ca^{++} + 2OH^- + 2NH_3 + 2NO_2^- \rightarrow Ca(NO_3)_2 + 2NH_3 + 2H_2O \quad (1)$$

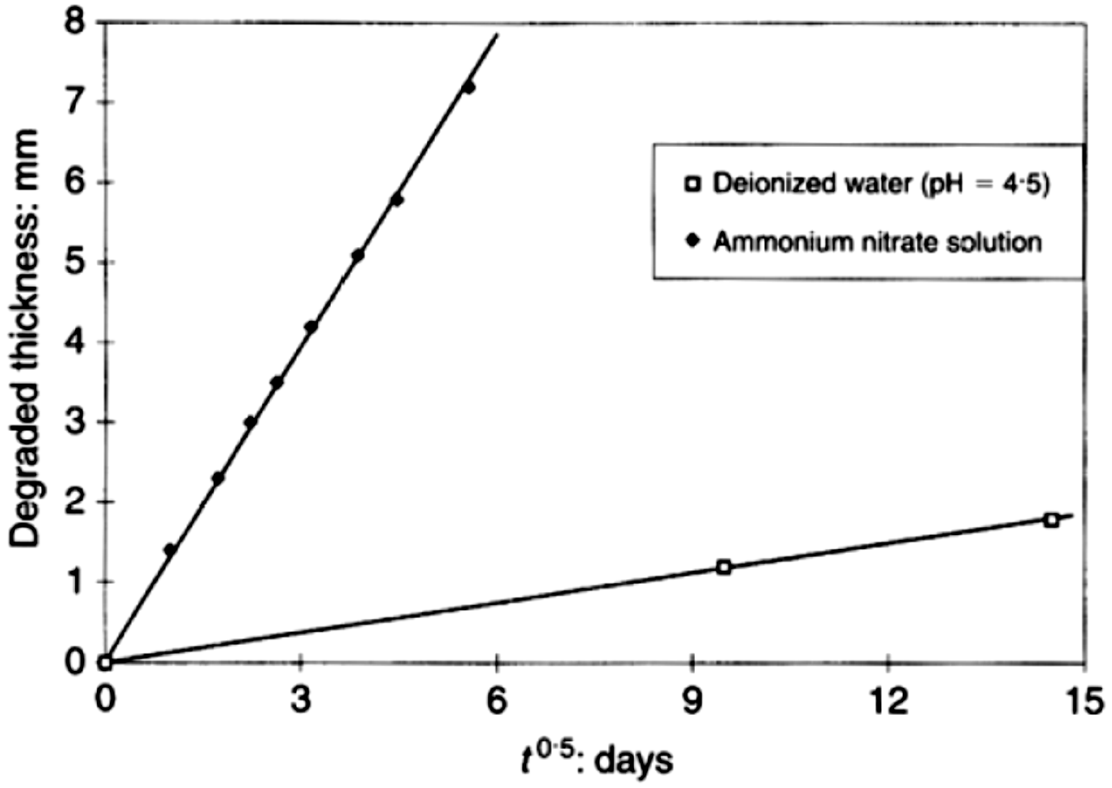

Figure 11 – Comparison of degraded thickness as a function of square root of time between deionized water and 6M ammonium nitrate solution reprinted from [36].

The leaching technique simulates years of decalcification in the field occurring in concrete pipes within a matter of days in the lab. Based on previous work done [36] the rate of decalcification of 6M ammonium nitrate solution is shown in (2).

$$d = 1.31\sqrt{t} \tag{2}$$

Where d is the thickness of decalcification in mm and t is the time of exposure in days. The rate of decalcification for deionized water is shown in (3).

$$d = 0.12\sqrt{t} \tag{3}$$

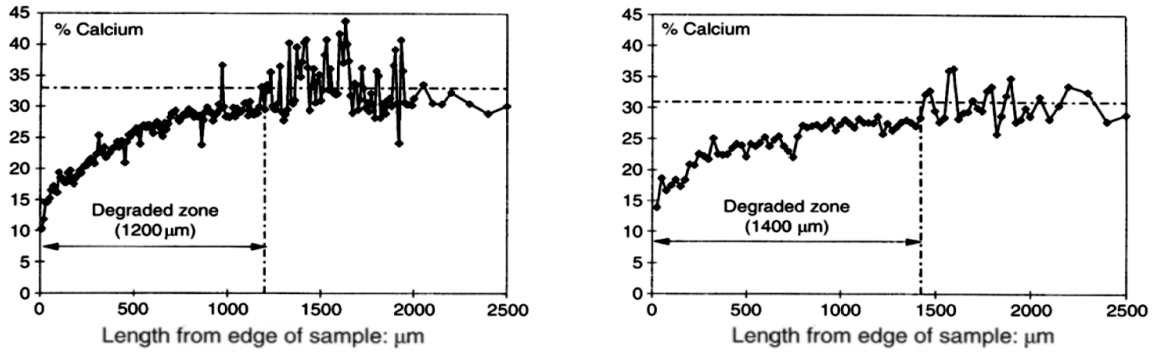

Figure 12 – Comparison of effect of calcium degradation between 3 months exposure of deionized water (left) and 1-day exposure to ammonium nitrate solution (right) reprinted from [36].

The time taken to decalcify a certain thickness of cementitious material is significantly higher for deionized water when compared to ammonium nitrate solution.

2.3 Permeability testing systems

In a traditional permeability test a hydraulic pressure is applied to once side of a disc of porous material. [37-39]. The fluid flux through the specimen is monitored with respect to time; once steady-state flow is achieved, the fluid flux directly indicates the permeability of the material (presuming a linear, Darcian constitutive function relating flux to the pressure gradient). This type of testing works well for materials having a relatively high intrinsic permeability like soil and highly porous rocks. It takes relatively long time to complete for materials having a lower intrinsic permeability like cement paste and concrete. It could take days for the flow to reach steady state condition for such low permeability materials, and once steady state is achieved it might take weeks to months to get reliable permeability results [37, 40]

The duration issue associated with conventional permeability measurement techniques can be solved by using poromechanical techniques. In recent years poromechanics has been identified as a tool which can reduce the time taken for permeability measurements [41]. On applying an external stress to a porous body, the time dependent deformation associated with the fluid flow into the pore network is monitored and used to calculate the permeability in poromechanical techniques. All of these tests have the advantage of being fast (the analysis is performed on non-steady state flow), though in some cases, the requirements for the tests are not practically feasible. Some examples of poromechanical methods include beam bending [42-45], thermal expansion kinetics [46-48], and dynamic pressurization [49-51]. The dynamic pressurization method has the least practical limitations for concrete testing among the listed techniques [52].

2.3.1 Dynamic Pressurization (DP) and Hollow Dynamic Pressurization (HDP)

Among the various poromechanical methods developed, the Dynamic Pressurization (DP) technique was chosen to determine permeability for the purpose of this study. The theory behind the technique was developed by Gross and Scherer [49] and was experimentally implemented on cementitious materials by Grasley et al. [51]. The DP method starts with the rapid (step) hydrostatic pressurization of a cylindrical specimen within a pressure chamber. The cylinder contracts volumetrically which is dependent on the bulk modulus of the specimen and that of the pore fluid [51]. As the solid phases in cementitious materials have a greater bulk modulus than the pore fluid, the dilatational stress field in the specimen is preferentially carried by the solids. Thus, a pressure gradient is established in the pore fluid; at the radial surface of the sample the pressure is equal to the applied pressure in the pressure cell while the pressure is significantly greater in the core of the sample. The cylinder expands as fluid flows into the pores of the specimen causing an increase in the pore water pressure. The rate of the expansion of the cylinder is related to the fluid flux in the pore network.

The DP technique is much faster compared to conventional permeability measurement techniques. However, a limitation of the DP technique is that the specimen must be completely saturated by a low-compressibility fluid (e.g., water or pore fluid) before testing, else re-expansion of the specimen will not occur till the air pockets within the specimen are completely compressed. To address this limitation, Jones et al. [53-55] devised the Hollow Dynamic Pressurization (HDP) technique where instead of using solid cylinders for the technique they used hollow cylinders. The

primary advantages of the HDP technique versus the DP technique are the ability to flush a portion of any entrapped air bubbles, the ability to perform a radial flow through test on the same sample that is tested for permeability via HDP, and a reduction in test duration.

The HDP apparatus involves a pressure chamber, in which both the inner and outer radial faces are pressurized, that can withstand an internal pressure of 13.1 MPa (1900 psi). As shown in Figure 14, the hollow specimen is attached to the top of the pressure chamber and is suspended in the pressurizing fluid. The stainless steel linear variable differential transformer (LVDT) connecting rod runs through the hollow center of the specimen up to the LVDT coil. This LVDT system is completely non-contact, which allows the chamber to be completely sealed with all electrical connections outside the chamber. Hydrostatic pressure is applied using an electric hydraulic pump regulated with a vented, inline pressure regulator. This setup allows both pressurization and gradual, stepped depressurization, which is important to avoid high internal tensile stresses associated with a rapid release of the applied pressure [53]. The pressure is recorded with an electronic pressure sensor capable of 0.05% accuracy and logged along with the displacement data using an electronic data logger. Once the strain-time history is recorded it is fit to

$$\varepsilon_z = \varepsilon_\infty(\varepsilon_0 - \varepsilon_\infty)\Omega(\theta) \tag{4}$$

where ε_z is the axial strain of the cylinder, ε_∞ represents the final axial, ε_0 represents the initial axial strain in the specimen $\theta = \frac{t}{\tau_{DP}}$ the testing time is represented by t, whereas τ_{DP} is the relaxation time of the test and is the single fit parameter. The fit function is given by (5)

$$\Omega(\theta) = e^{\left[\frac{4}{\sqrt{\pi}}\left[1-(1-\beta)b\lambda\right]\left(\frac{\theta^m-\sqrt{\theta}}{1-\theta^n}\right)\right]} \tag{5}$$

b is the Biot coefficient, β and λ are material properties of the porous body defined by equations (6) and (7), the parameters m are n are defined in equations (11) and (12).

$$\beta = \frac{1+\nu_p}{3(1-\nu_p)} \tag{6}$$

$$\lambda = \frac{Mb}{K_p + Mb^2} \tag{7}$$

where K_p and K_s represent the bulk moduli of the whole porous body and the solid skeleton structure (ignoring porosity) defined in equations (8) and (9), M represents the Biot modulus as defined in equation (10) and ϕ is the porosity of the material.

$$K_P = K_S(1-\phi)^2 \tag{8}$$

$$K_s = \frac{P_a}{3\varepsilon_0} \tag{9}$$

$$M = 1/\left(\frac{\phi}{K_l} + \frac{b-\phi}{K_s}\right) \tag{10}$$

The parameters m and n are defined by the equations (11) and(12).

$$m = 5.62\left(\frac{R_o}{R_i}\right)^{-0.196} \tag{11}$$

$$n = 0.401 + 0.00562\ln\left(\frac{R_o}{R_i}\right)^{1.85} \tag{12}$$

R_0 and R_i are the outer and inner radii of the hollow cylinder used. Once the value of τ_{DP} is determined by fitting the re-expansion strain curve the intrinsic permeability 'k' of the specimen is calculated from equation(13), where η_l is the viscosity of the liquid used

$$k = \frac{\eta_l\left(R_o - R_i\right)^2}{\tau_{DP}}\left(\frac{\beta b^2}{K_P} + \frac{1}{M}\right) \tag{13}$$

2.3.2 Radial Flow-Through (RFT)

The Radial Flow-Through (RFT) test is relatively simple flow-through test in concept. Instead of using a disc the method uses a hollow cylindrical sample. A step pressure is applied to the outer face of the cylinder. This method is an accelerated, conventional flow-through method. The test apparatus used borrows components form the test setup used by Banthia et al. and one developed by El-Dieb et al. [39, 56-58]. The setup as shown in Figure 14 is comprised of a hollow cylinder sealed at both ends with steel plates. On application of fluid pressure to the outer radial face, the fluid moves through the pore network of the sample along the wall of the hollow cylinder causing a net increase in the fluid level inside the center hollow "tube." By monitoring the evolution of

this fluid level with an LVDT, a flow rate can be determined. Once this flow rate reaches steady state conditions it can be used to determine the permeability of the material..

By monitoring the rate of flow of the liquid the intrinsic permeability can be determined by (14)

$$k = \frac{q\eta_l \ln\left[R_o / R_i\right]}{2P_a \pi h} \tag{14}$$

where q is the measured flowrate of the liquid, P_a is the pressure applied in the pressure vessel as the driving force, and h is the height of the sample used. Using the intrinsic permeability the water permeability can also be determined by using (15)

$$k_w = \frac{\rho g k}{\eta_w} \tag{15}$$

where ρ is the density of water, g is the acceleration due to gravity and η_w is the viscosity of water

The apparatus shown in *Figure 13* and *Figure 14* allows pressurizing the sample to different levels depending on its particular geometry, its relative permeability, and its strength. For a specimen with lower permeability, the pressure on the outer face can be increased to increase the fluid flux through the sample. Conversely in a highly permeable specimen the fluid flux can be reduced by lowering the pressure applied to the specimen. The merits and demerits of this system is explored in detail in Jones et al. [59]

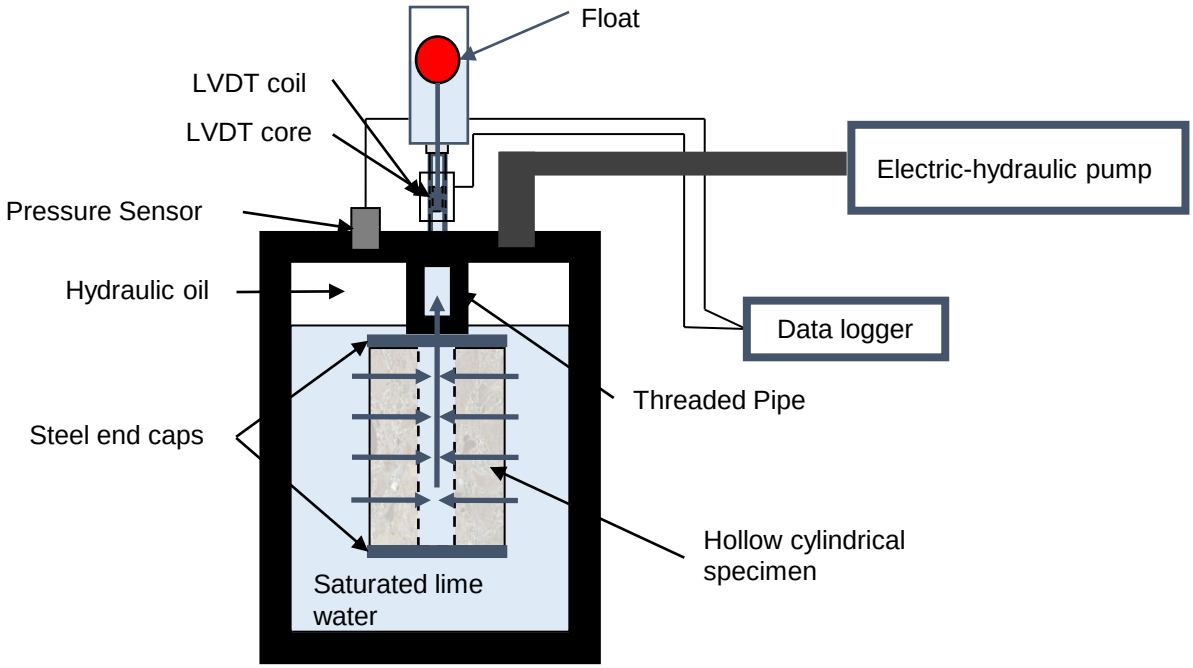

Figure 13 – Schematics of the equipment required to setup Radial Flow-Through Test– A step pressure is applied to the cylinder and this forces the water to flow though the cylinder walls into the inner hole of the cylinder, the rate of flow is measured with a LVDT attached to a float.

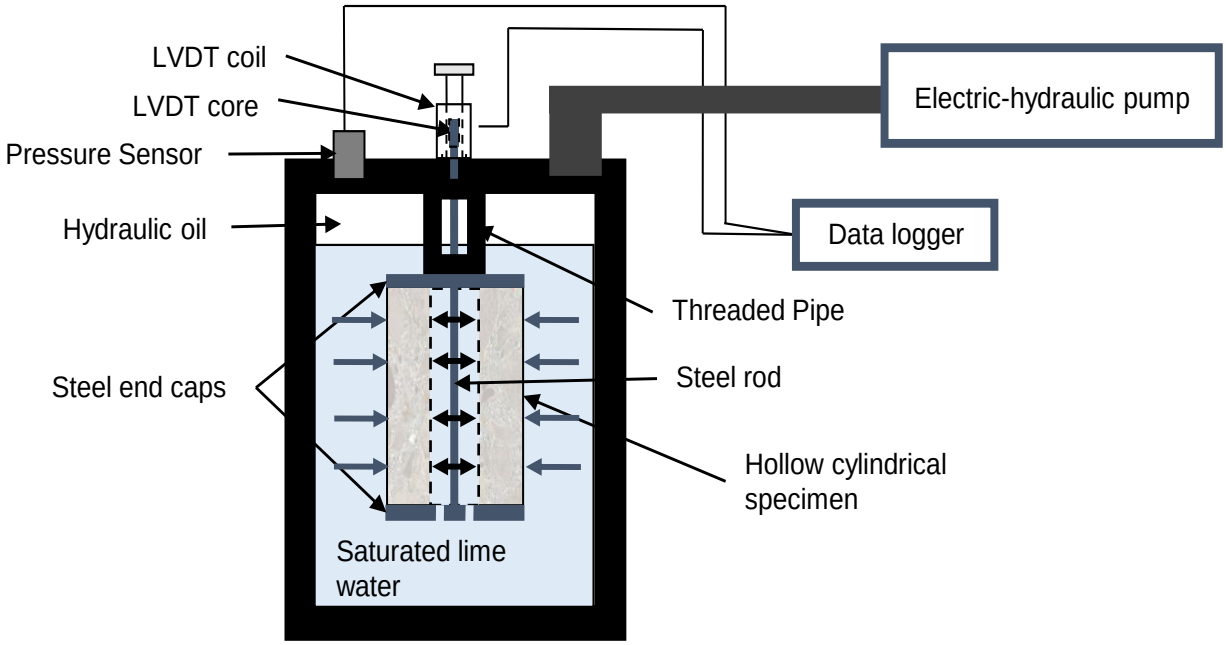

Figure 14 – Schematics of the equipment required to setup Hollow Dynamic Pressurization Test – A hydrostatic step pressure is applied in the chamber which causes the cylinder to contract hydrostatically, the flow of water into the pore network causes re-expansion which is measured by the LVDT.

2.4 X-ray CT

X-ray CT is a non-destructive imaging and characterization technique where x-rays are used to construct a virtual 3-dimensional model of an object. X-rays are passed through the object and a detector receives them and creates a series of 2-dimensional projections of the objects as projection images. These projection images are processed through tomographic reconstruction a series of 2-dimensional slice images of the object is obtained. Using image manipulation software these

images can be stacked to create a 3-dimensional model. The pixel size spatial resolution of these reconstructed images can be as low as 500 nm.

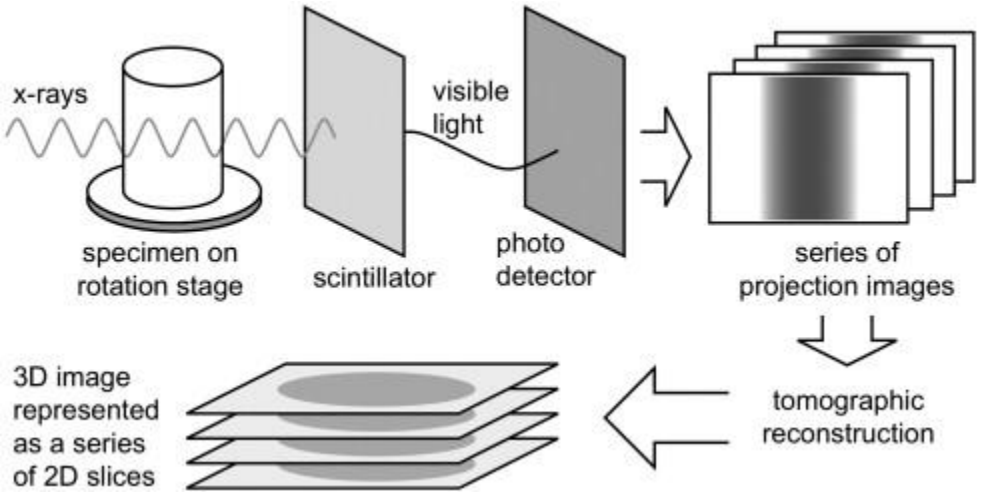

Figure 15 – Schematic of X-ray CT acquisition and reconstruction processes. A series of X-ray projection images are acquired and reconstructed to produce a 2-dimensional map of X-ray absorption as image cross section slices reprinted from [60].

X-ray CT technique was initially used for imaging in the medical field as it provides a 3d images of the human body in a noninvasive method. The use of X-ray CT techniques for study of porous materials gained traction in the early 2000s. There were many studies performed using X-ray CT imaging in the fields of geology[61, 62], asphalt concrete[63], soil analysis and portland cement concrete[62, 64-71]. X-ray CT analysis has become significantly common in analyzing concrete microstructure and its properties.

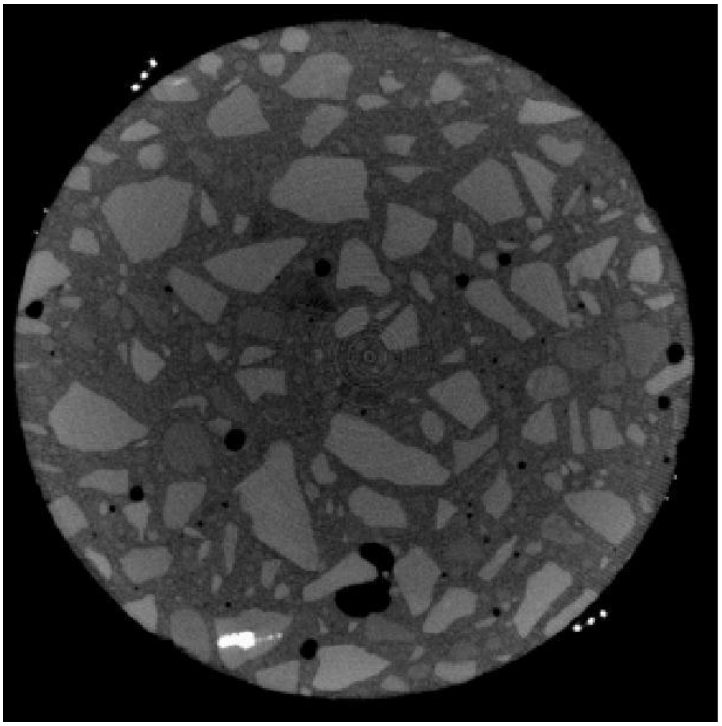

Figure 16 – 2d reconstructed image slice of a concrete cylinder obtained from X-ray CT image analysis.

Figure 16 shows a reconstructed image slice of a concrete cylinder obtained from X-ray CT imaging. It can be seen from the image that the internal properties of cement concrete are visible in the 2d slice. The aggregate distribution, air void spaces, porosity, damage and pose size distribution are some of the information that can be obtained from this technique. This information can be obtained in other ways too, but X-ray CT is a non-destructive testing method and is significantly advantageous when compared to the other techniques when the specimen in question needs to be intact.

Figure 17 shows a section of a 3D generated view of a specimen analyzed by X-ray CT. The 2D image slices can be manipulated to show features of the microstructure or any feature that is of interest and then the manipulated image can be compiled together to form a 3D model that illustrates only the features required. Thus, they can be manipulated to provide a 3-dimensional view of the pore network or even manipulate the damaged areas of the specimen and highlight them in detail.

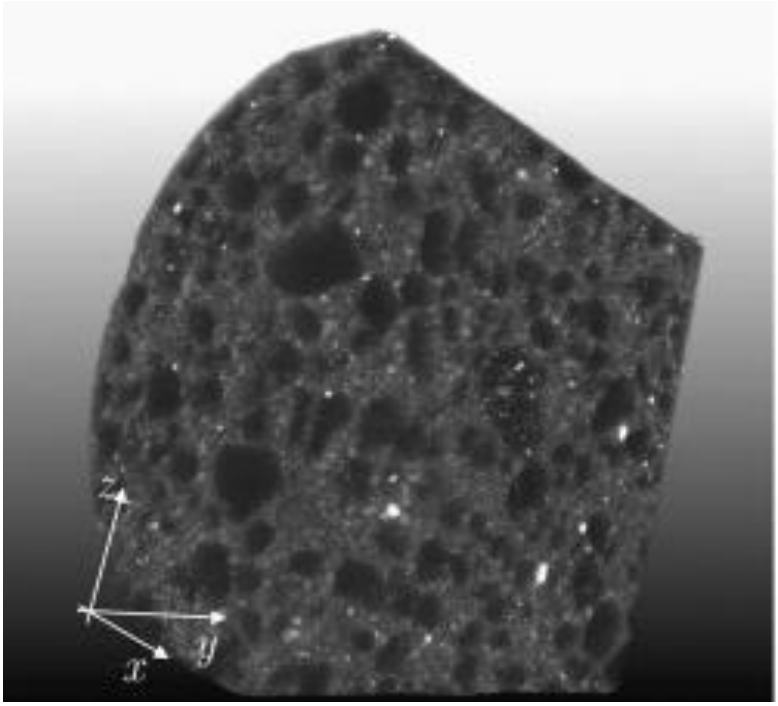

Figure 17 – 3D sectional view of a specimen analyzed using the X-Ray CT method.

The X-ray source and the X-ray beam geometry typically limit the spatial resolution of X-ray CT reconstructed images. If more photons collide with the object, the higher the chance for the detector

to capture all the details of the object without incurring any loss in data. The size of the detector also plays an important role in the sharpness of the image. For a point source of X-ray, the smaller the spot size the less blurring occurs. With a larger spot size different X-ray beams can be traced for a single pixel on the detector. One-megapixel detector is the most commonly found detector while detectors up to 12+ megapixels are used in extreme fringe cases where that level of accuracy is needed. The development of synchrotron radiation as a source of x-rays has improved the proliferation of X-ray CT technology to many research labs [72-74]. It produces a significantly brighter X-ray source and the resulting image has much higher contrast. Conventional sources often resulted in images that were blurry and required significantly longer exposure time to get optimal contrast and image clarity. However longer periods of exposure mean more cost to run the equipment and thereby increase in the cost of performing the analysis.

The primary limitation for a detailed analysis of the microstructure of porous material is the relationship between the size of the object being imaged and the spatial resolution of the image obtained from reconstructed tomography. Modern x- ray micro tomography equipment can scan with a spatial resolution as high as 500nm per pixel. However, the size of object that is needed to produce a spatial resolution of 500nm cannot exceed 1mm in diameter for cylindrical specimens. Thus, X-ray CT is an extremely convenient and useful method in the case of large specimens requiring low spatial resolution of the reconstructed images or specimens where the size can be reduced to millimeter scale to get the highest possible spatial resolution the equipment has to offer. The tradeoff in using it for bigger specimens will be the lower spatial resolution that the imaging analysis can provide.

2.5 SEM EDS

2.5.1 SEM

The principle of a Scanning Electron Microscope (SEM) is to use a focused beam of electrons to bombard a target that is to be imaged. The electrons interact with the atoms in the sample and produces a signal which is used to image the sample. The earliest SEM machines used an electron scanner as the detector for the emitted electrons[75]. . A thermionic gun was used for the electron beam generation. The device had unit magnification and was not able to provide any significant information on the scanned surfaces. Improvements made by Manfred von Ardenne, a British scientist, improved the magnification significantly by applying electrical optics to the system and was able to obtain sub microscopic resolution [76]. SEM still was a very expensive technique and though sub microscopic resolution was possible it still fell short compared to an optical microscope. Pioneering work done in the field in the in the 1960s and 1970s revolutionized the device and made it more accessible for researchers. Improvement of instrumentation like electron sources, electron optics, detectors and signal processing helped tremendously towards this purpose.

A significant improvement in SEM technology was the development of the Field Emission SEM (FESEM). This invention single handedly revolutionized the technology and made it commercially accessible in the 1980s. Field emission guns replaced thermionic guns as a source of electrons. Field emission guns allow the formation of electron probes up to 0.5nm in diameter. Coupled with improvement in electron optics, electron detection and significantly improved specimen

preparation very high resolution FESEM became feasible. Another advantage of using FESEM is that it allows specimens to be operated under low acceleration voltages, i.e, below 5kV and achieve high resolution.

Another significant improvement in instrumentation was the development of Environmental Scanning Electron Microscope (ESEM) in the late 1980s by G.D Danilatos [77]. SEM and FESEM were restricted to high vacuum pressures. ESEM on the other hand could perform analysis on specimens using secondary and backscattered electrons in low vacuum pressure of a10 up to a few thousand Pascals. This was a significant breakthrough as samples containing dirt or fluids as they could be viewed in the partial pressure vacuum range mentioned above. Typical examples include soil and geological samples which contain water, oil, and other fluids in their natural states. The development of ESEMs enabled the imaging of these materials in their natural states without having to dry them up which was needed to micrograph them using FESEM.

Most modern FESEM setups have a high resolution of 0.5-1nm in the energy range of 30keV. This typically corresponds to the smallest size of molecules possible. These high resolutions also enable the imaging of structural surface features for up to 1 mm, i.e., high-resolution SEMs can be used to characterize structural features covering a wide range of six magnitudes. Another advantage of modern SEM setups is the ability to simultaneously acquire different signals generated by the intersection of the local electron beams with the specimens. Each signal carries a different set of information about the surface that is being scanned. Therefore, is it possible to obtain multidimensional level of data from the area of interest. The time required to record this data can range from a few seconds to a minute depending on the signal strength and noise in the data. SEM

is commonly used in material characterization, ceramics, life sciences, mineralogy, geology and several other fields of science where extremely high-resolution micrographs are required.

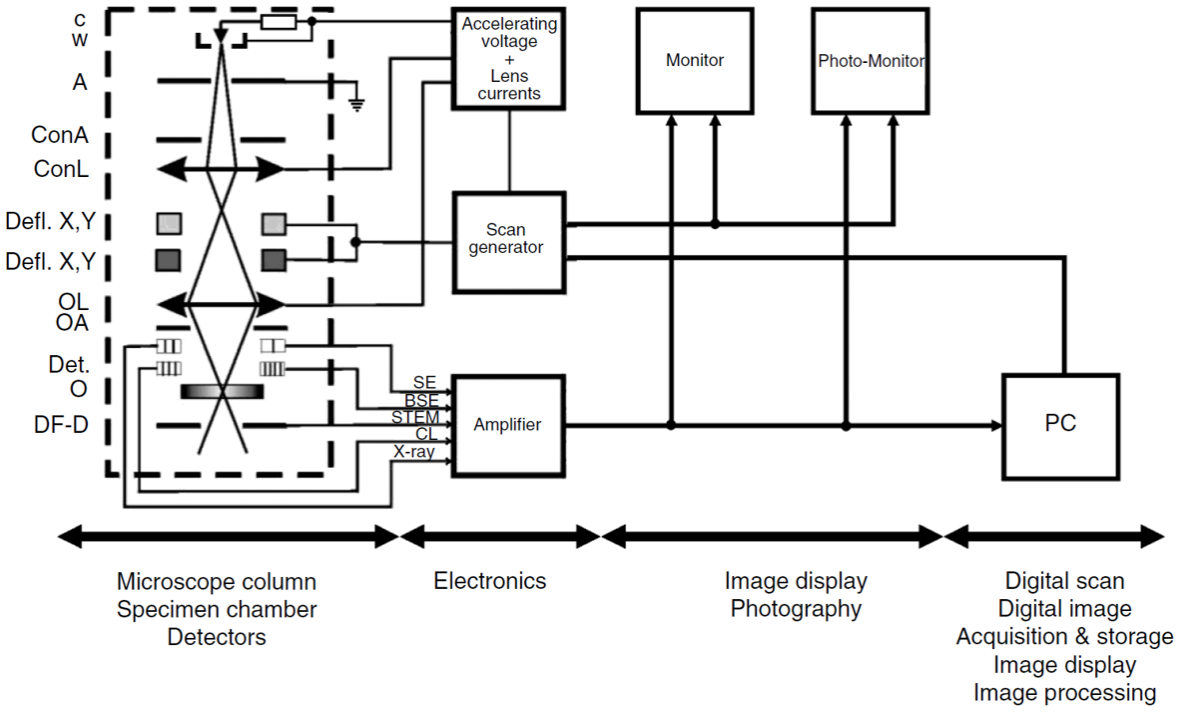

Figure 18 – Schematic of a SEM (conventional). The electron gun, electromagnetic lenses, electromagnetic deflection coils, apertures, the specimen stage, and the detectors are housed in the microscope column. The power supplies for the acceleration voltage and the electromagnetic lenses, the scan generator, amplifiers for the signals, and monitors for display and recording of images are housed in the electronics console. A PC controls modern SEMs. Reprinted from [78].

The basic schematic of a scanning electron microscope is shown in Figure 18. The two major parts of a SEM are the microscope column and the electronics console. The microscope column consists

of the electron gun, electromagnetic lenses, electromagnetic deflection coils, apertures, the specimen stage, and detectors. The electronics console consists of the power supplies for the acceleration voltage and the electromagnetic lenses, the scan generator, amplifiers for the signals, and monitors for display and recording of images. The microscope column is evacuated by using a combination of high vacuum pumps and pre-vacuum pumps. For FESEM setups the pressure in the chamber is around 10^{-4} Pa. The main reason for this level of vacuum pressure is to enable the electrons from the electron source to reach the specimen without having to interact with the atoms of the atmospheric gas molecules. The electron beam generated from the cathode is accelerated using an acceleration voltage of 0.5-30keV between the anode and cathode to form a crossover (small electron beam cross-section) of electrons. The electromagnetic lens system adjusts this crossover to produce a spot size of 5-10 nm on the surface of the specimen.

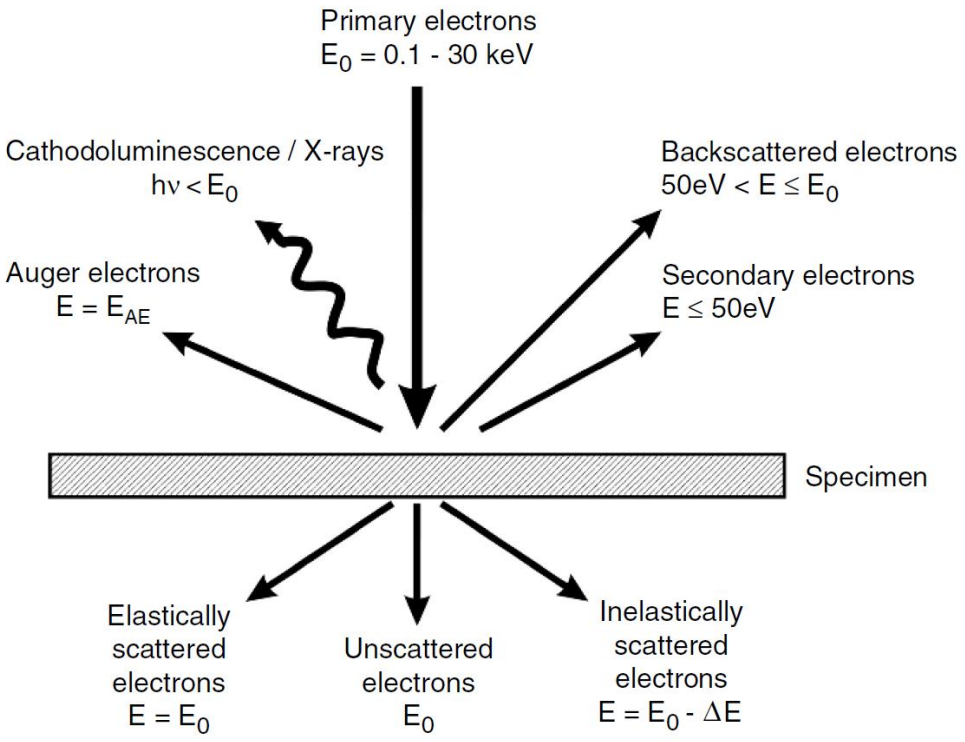

Figure 19 – Drawing of signals generated by a thin film of SEM sample upon being impinged by accelerated electrons. E_O - energy of beam electrons; E - energy of signal electrons; E_{AE} - energy of Auger electrons; ΔE - energy loss of inelastically scattered electrons; $h\nu$ - energy of radiation reprinted from [78].

When the electron beam hits the target, it interacts with the atoms of the specimen by causing elastic and inelastic scattering of electrons. Figure 19 shows a rough schematic of how the interaction from the primary electron on a thin SEM specimen generates various signals caused due to the elastic and inelastic scattering of electrons from the target atom. Elastic scattering is caused by the interaction of the primary electron beam with the nucleus of the atom which is positively charged. Energy loss due to elastic scattering is almost zero. Inelastic scattering of an electron is caused by the interaction of the primary electron beam with the electrical field of the

target electrons. After inelastic scattering the electron beam usually has a different direction and lower kinetic energy. Backscattered electrons are electrons that are reflected towards the source either by elastic or inelastic scattering. In the case of elastic scattering the energy is significantly higher and lower in the case of inelastic scattering. Inelastic scattering inside the target specimen causes the release of secondary electrons, auger electrons and X-rays which can provide significant insight about the structure, topography, and material composition of the target.

Secondary electrons are a set of electrons generated by inelastic scattering of the primary electrons along their atomic trajectories. By definition, secondary electrons are those that have less than 50eV. The only secondary electrons that are observable are those that can escape the energy depth of the surface. Secondary electrons can sometimes also be generated by scattered electrons though the probability of that is very low compared to those that are generated by the incident beam.

2.5.2 EDS

Energy Dispersive Spectroscopy (EDS) also referred to as Energy Dispersive X-ray analysis (EDX) is a commonly used tool in material characterization and analysis. It is used in tandem with a SEM. The basic principle behind EDS is the measurement of X-rays generated when the incident beam electron interacts with an electron present in the inner shell of an atom. The incident beam transfers a part of its energy to the atomic electron due to collision and excites the inner shell electron to a higher electron shell. The atom that had the excited electrons now has excess energy and must lose that energy in order to retain its stability. There are two possible ways in which this excess energy could be dissipated. First method is by emitting an electron from its outer shell with

the characteristic energy (Auger Electron) [79-81] thereby maintaining the energy balance. The second method is by releasing the energy from the excited electron in the form of electromagnetic radiation (X-rays) [82-85] and the excited electron returns to its original shell and maintains the energy balance.

The fraction of X-rays emitted during this electron transition is defined by factor called fluorescence yield ω. This factor is dependent on the atomic number of the atom in question and the inner electron shell involved in the process of excitation. The compliment of the fluorescence yield is called the auger electron yield (1-ω) which defines the fraction of auger electrons emitted during the atomic excitation and stabilization. Figure 20 shows the relationship of X-ray fluorescence yield and Auger electron yield, and the K-, L-, M-shells and atomic number. The X-ray generated are categorized into two types. The first type is caused by the deceleration of electrons generating continuum X-rays. The second type is caused by electron transition from a filled higher state to a vacant lower state generating characteristic X-rays. Figure 21 shows a typical X-ray spectrum emitted from a specimen that was bombarded by accelerated electrons. The X-ray continuum consists of a continuous distribution of intensity vs energy. On the other hand, the characteristic spectrum consists of a series of discrete peaks at element specific energies. The two spectrums are superimposed, and their positions are independent of the incident electron energy. The peaks are only observed if the corresponding atomic energy level is excited. Characteristic X-ray generation occurs in three steps, the incident beam electron interacts with an electron in the inner shell of the atom and ejects the atom to an excite state, then the excite electron relaxes to ground state by the emission of energy equal to the energy difference between the excited

state and ground state, finally this element specific energy difference is released as an auger electron having the excess energy or as a characteristic X-ray with the energy ΔE_{ch}.

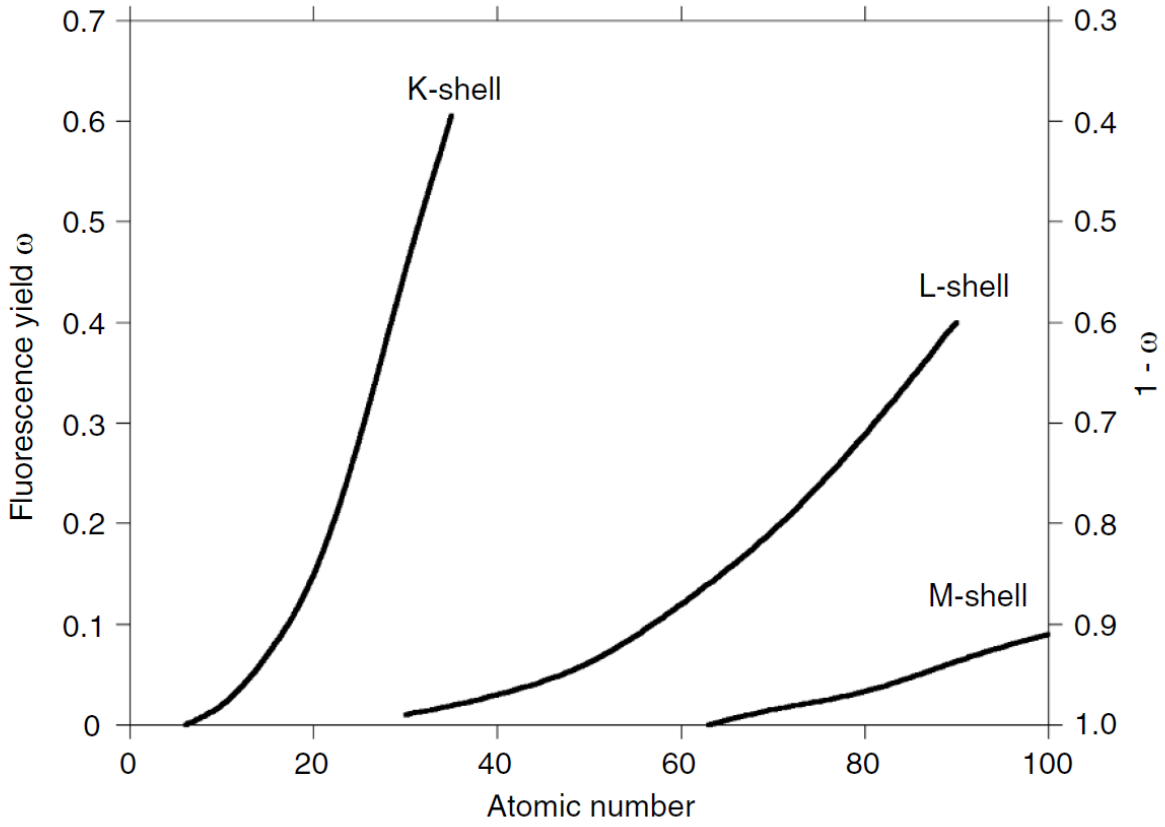

Figure 20 – Graph showing the relationship of X-ray fluorescence yield and Auger electron yield, and the K-,L-,M-shells and atomic number. As the atomic number of the element increases the change from fluorescence yield to auger electron yield increases. Reprinted from [78].

The characteristic X-rays emitted from a specimen carries significant amount of information regarding its elemental composition. With the use of a EDS spectrometer in tandem with a SEM

these X-rays emitted can the collected and measured. The interaction volume of X-rays is slightly higher than the ones for auger electrons, scattered electrons, and back scattered electrons. This is because X-rays have more penetrating power and are absorbed less compared to electrons having the same energy.

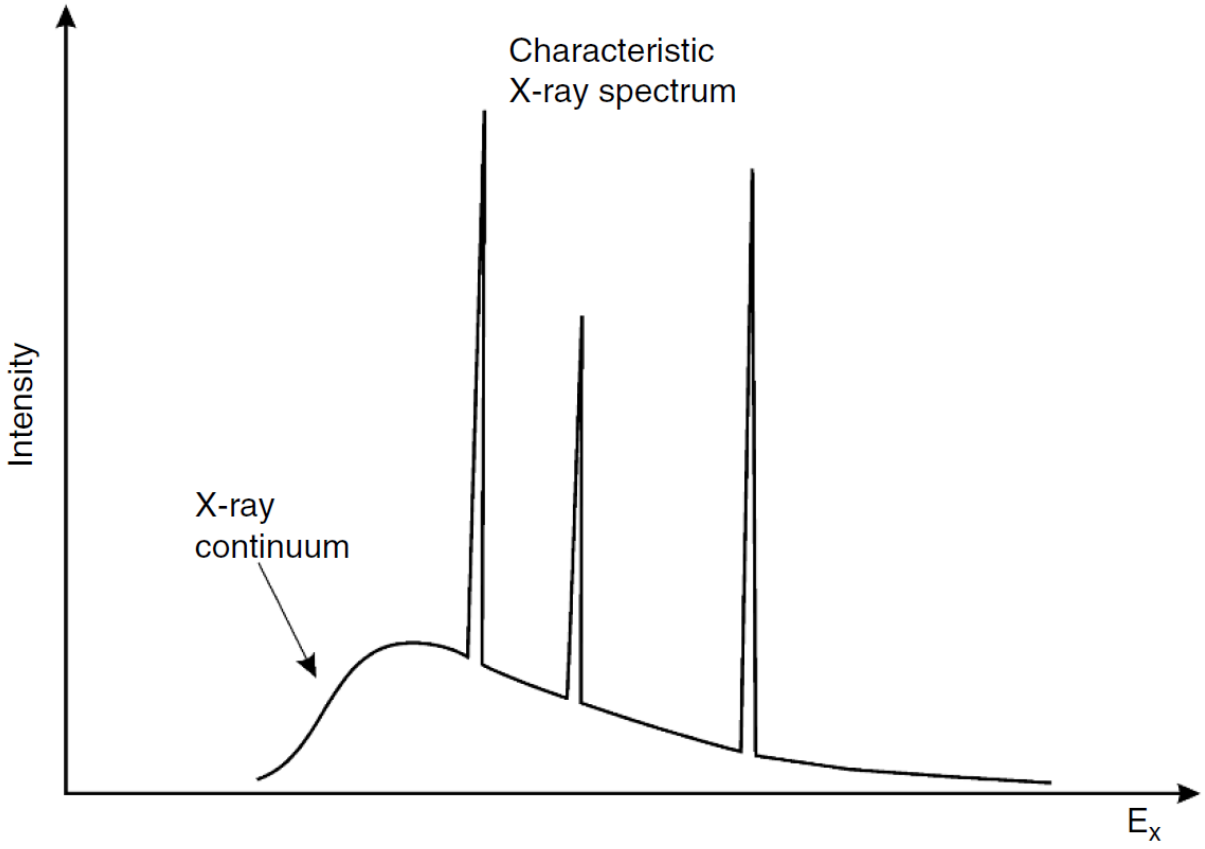

Figure 21 – Graph showing a typical X-ray spectrum emitted from a specimen bombarded with accelerated electrons The X-ray continuum consists of a continuous distribution of intensity vs energy and, the characteristic spectrum consists of a series of discrete peaks at element specific energies reprinted from [78].

In EDS systems the X-rays are measured by using a solid-state semiconductor detector. The absorbed X-rays causes electron hole pairs that creates a current pule to flow thorough the detector circuit. The number of electron pairs produced is directly proportional to the energy of each X-ray photon. The most powerful ability of SEM-EDS analysis is the ability to map elemental composition on a surface that is composed of heterogenous elements. Very high resolutions of up to nanometer levels can be obtained. Another interesting ability is the ability to perform multilayer analysis of the target specimen. By changing the energy of the incident electron, it is possible to change the depth to which the electrons can interact with in the target sample. This allows EDS analysis to be conducted in layers accurate up to 2 nm thickness [86, 87].

It is also possible to perform quantitative analysis of the elemental composition on the specimen surface using SEM-EDS. In quantitative the mass fractions of or weight percentages of the different elements present of the specimen surface are measured and calculated. This is achieved by the use of standard reference materials. Standard reference materials are materials whose elemental composition is well known by using multiple types of analysis techniques. X-rays from the sample are compared against the X-rays obtained from the standard reference material. In a Standardized Quantitative Analysis, the reference spectra are obtained from the same machine that is used to scan the specimen. In a Standardless Quantitative Analysis the reference spectrum stored in the equipment is obtained from another machine than performed the analysis on the standard reference specimen.

Qualitative analysis is first performed to identify the different elements present in the specimen surface before quantitative analysis is performed. High acceleration voltages greater than 15kV is

typically used to excite the electrons in the specimen. For accurate analysis it is necessary to have a specimen that is stable, flat, and homogenous. Some limitation of quantitative analysis includes light elements like hydrogen and helium cannot be accurately detected because of the nature of EDS analysis as they cannot generate characteristic X-rays. Carbon and oxygen are present abundantly in nature and specimens that contain these elements need to be corrected for the naturally occurring percentages.

3 POROMECHANICAL VS. RADIAL FLOW METHODS FOR PERMEABILITY[1]

The differences in approach between conventional permeability tests and poromechanical tests are significant, it was necessary to determine whether the tests yield equivalent measured permeabilities on the same cementitious sample. The objective of this section of the study is to test the hypothesis that the permeability obtained from poromechanical techniques is different when compared to flow-through techniques for certain cementitious materials. Furthermore, if there is a difference detected, the source of the difference in the permeability will be identified.

A pilot study was performed previously by Jones et al [59, 88] comparing the Hollow Dynamic Pressurization (HDP) and the Radial Flow-Through (RFT) results. In the referenced pilot study, the viability of the HDP technique as a replacement for traditional permeability tests was explored. The study was focused strictly on cement paste and Vycor glass – a highly porous, silica glass made by Corning Incorporated [89] occasionally used as a non-reacting laboratory surrogate for cement paste. The pilot study showed that the values for permeability observed by HDP and RFT were similar and the work established that the permeability from HDP is comparable to values obtained from conventional flow-through experiments in the case of cement paste and Vycor glass. Cement mortar and concrete are the main uses of cement in the construction industry and it would be of great interest to observe how the performance of these materials compares in a poromechanical technique and a flow-through permeability test. The current study expands on the

[1] Part of this chapter is reprinted with permission from "Comparison of Permeability of Cementitious Materials Obtained via Poromechanical and Conventional Experiments" by Jeffryd Rose and Zachary Grasley, 2017, *Journal of Materials in Civil Engineering* 29.9: 04017083, Copyright 2017 by Jeffryd Rose and Zachary Grasley.

previous work and compares the results from tests on cement paste, cement mortar, and concrete specimens. The microstructure of mortar and concrete have additional mode(s) in their pore size distribution when compared to cement paste. Previous research has shown that the presence of the interfacial transition zone (ITZ) between the cement paste matrix and the aggregate inclusions has a definite effect on the various physical properties of cement mortar and concrete [90-96]. In particular, it has been demonstrated that the ITZ results in a multimodal or multi-porosity network [94, 97] (see Figure 22). Thus, while cement paste has been shown to yield identical measured permeabilities from conventional flow-through and poromechanical techniques, such may not be the case with mortars or concrete.

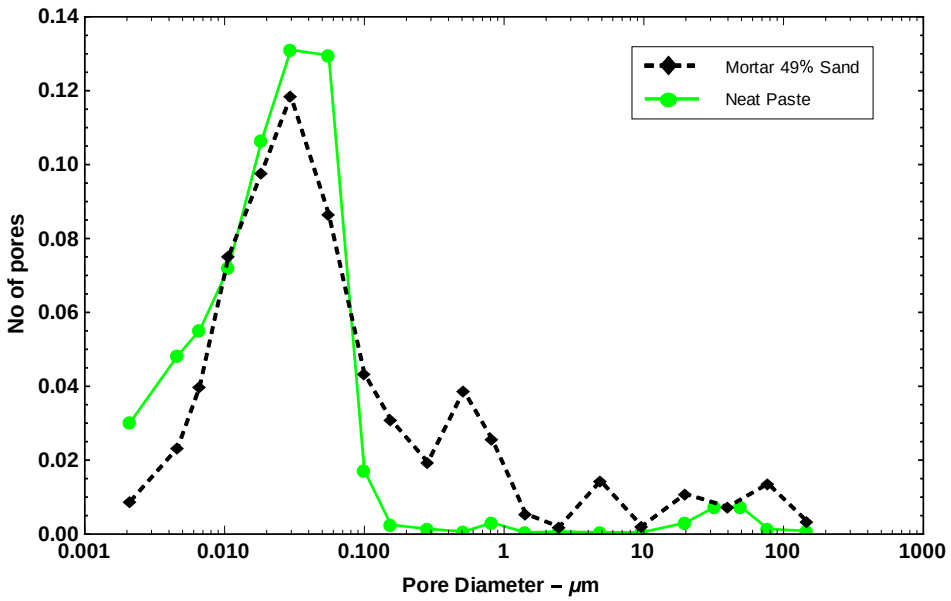

Figure 22 – A comparison of the pose size distribution of cement paste (green solid) and cement mortar (black dashed) showing additional mode(s) in pore size distribution in cement mortar. The presence of the interfacial transition zone (ITZ) contributes to the additional pore size distribution mode(s) in cement mortar. Adapted from [94].

3.1 Specimen preparation

The materials investigated were cement paste, cement mortar, and cement concrete. The test on the cement paste was done to validate the results obtained from the previous pilot study and to provide a baseline for the study to be performed on the cement mortar and concrete. The cement used for the study was regular Type I/II cement. For cement mortar specimens, the sand used was river sand with 100% passing through the No. 16 sieve. For concrete specimens, the coarse aggregates were pea gravel with the largest size passing through No.4 (4.75 mm) sieve.

A water to cement mass ratio (w/c) of 0.6 was chosen for the test in order to ensure a relatively high permeability of the resulting specimens. The high permeability was attractive since it enables shorter test durations for the tests in consideration. For this study, only one w/c ratio was used; previous research indicates that a change in w/c ratio by 0.1 changes permeability by one order magnitude [98]. For the cement mortar specimens, a fine aggregate/cement mass ratio of 2 was used; the concrete used the same fine aggregate/cement mass ratio and also had a coarse aggregate/cement mass ratio of 4. For cement paste and mortar, the samples used for the testing had the following dimensions: 25.4 mm (1 inch) outer diameter, 6.35 mm (0.25 inch) inner diameter and 50.8 mm (2 inch) long as shown in Figure 23. For concrete, the samples used for the testing had the following dimensions: 50.8 mm (2 inch) outer diameter, 6.35 mm (0.25 inch) inner diameter and 101.6 mm (4 inch) long.

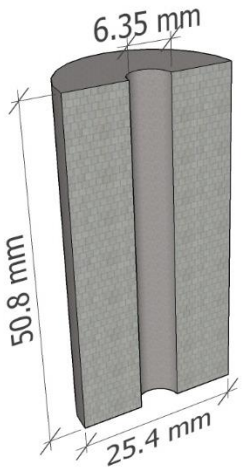

Figure 23 – Dimensions of hollow cylinder specimen cross-section used for paste and mortar permeability testing in Hollow Dynamic Pressurization and Radial Flow-Through methods

The cement paste mortar and concrete specimens were mixed according to ASTM C305-99. Preparing the 0.6 w/c cement paste was a challenge as bleeding tends to result in the formation of different zones with a varying w/c across the height of the specimen. The bleeding issue was overcome by sealing the specimens completely in the mold and then using motor-driven rollers to keep samples rotating until after setting. The presence of fine aggregates prevented the bleeding effects in mortar and concrete observed in the cement paste. The samples were prepared by pouring the cement paste or mortar into a 25.4 mm inner diameter polycarbonate tube molds. The hole in the middle was made by using a 6.35 mm polyethylene tube. The ends of the tube were sealed using 25.4 mm steel washers with a 6.35 mm hole. Concrete samples were prepared by pouring the mix into 2 x 4-cylinder molds and using the 6.35 mm polyethylene tube to create the hole in the middle of the sample.

The specimens were maintained at lab room temperature (about 20° C) in sealed condition until being demolded at approximately 18 hours age. The samples were then immediately placed in a saturated lime water solution to improve the degree of saturation and to prevent calcium hydroxide leaching. The specimens were allowed to cure in the lime water for different ages and then they were tested for permeability.

3.2 Permeability testing

The specimens were tested for permeability using the HDP and RFT methods at different ages. The ages chosen were 7 days, 10 days, 12 days, 15 days and 28 days (7 days, 15 days and 28 days for concrete). One of the limitations of the DP/HDP test is that unless the specimen is completely saturated the re-expansion does not occur. This problem was overcome by performing the RFT test first which enabled the samples to reach a higher degree of saturation than by just being submerged in water. The HDP test was performed on the samples after the RFT test.

The RFT test was run at 2 MPa hydrostatic pressure and the HDP test was run at 8.2 MPa hydrostatic pressure. As the samples are under a state of hydrostatic compression during the tests, the risk of damage is minimal. The greater risk of damage is during depressurization, upon which the samples go into hydrostatic tension. The way we addressed the potential for damage between tests is by depressurizing the pressure chamber with steps smaller than the estimated tensile strength of the material.

Once the HDP test was completed the samples were tested for total porosity as it is an essential component in calculating the permeability from the HDP test. The saturated surface dry mass and

oven dry mass were measured and the total porosity was calculated from the measurements [27]. Porosity measurements were made on the specimens at 29 days and applied to all the specimens since previous research has shown that the total porosity does not show a significant change (with respect to calculating permeability via the HDP experiment) after five days of curing [98]. Three specimens were tested at each age for permeability (using both the HDP and the RFT methods).

3.3 Results

The average total porosity of the paste specimens was measured to be 47%. The results of the permeability tests are graphed in Figure 24. It can be seen from the graph that the permeability values obtained from HDP and RFT tests are essentially the same. The values of the average permeability measured from both the tests are tabulated in Table 1. The average percentage difference between the permeability values is 20%. The results are in agreement with the previous work done by Jones et al [88].

Table 1 – Mean permeability values (units of m^2) measured in HDP and RFT tests for cement paste.

Age	HDP result	HDP SD	RFT result	RFT SD
7 days	9.05E-19	4.9E-19	8.46E-19	3.6E-19
10 days	3.28E-20	1.53E-20	2.11E-20	1.6E-20
12 days	1.61E-20	6.1E-20	1.06E-20	2.3E-21
15 days	6.32E-21	2.09E-21	7.43E-21	1.6E-21
28 days	3.09E-21	1.31E-21	3.38E-21	1.45E-21

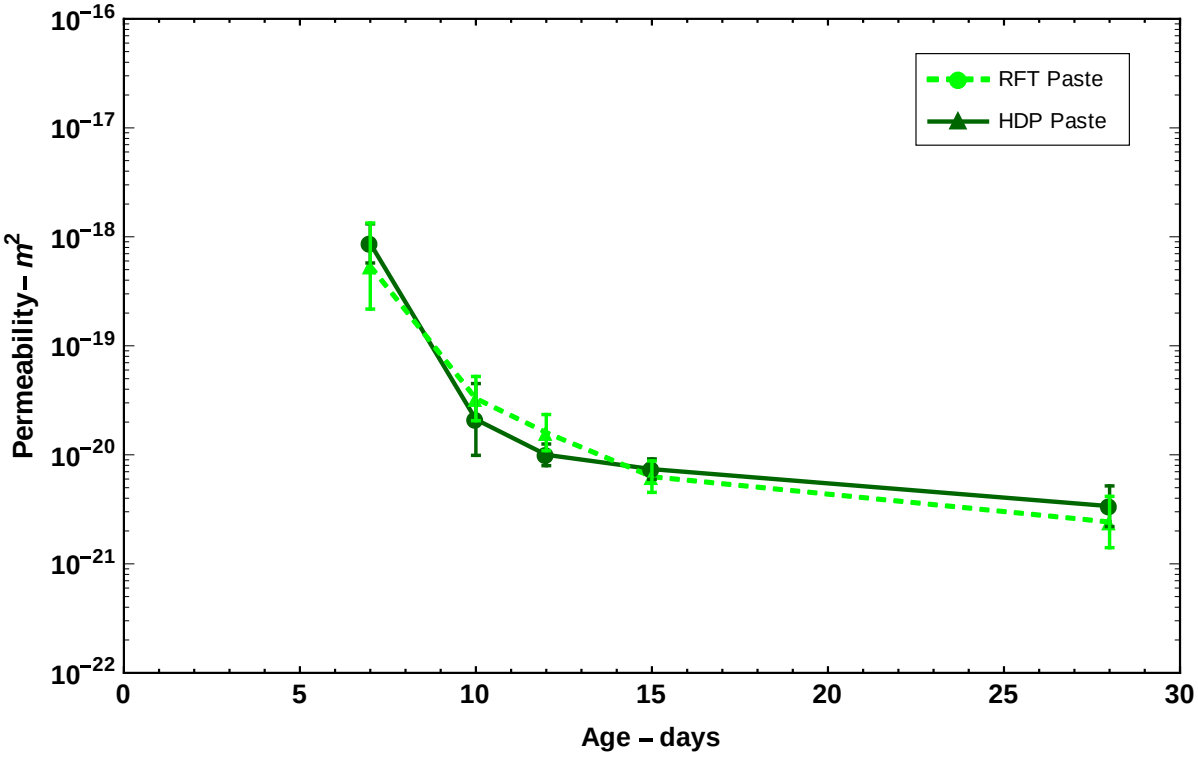

Figure 24 – Measured permeabilities obtained via HDP and RFT methods for **cement paste** at different ages shows that the permeability values obtained between the two techniques are essentially the same. The error bars on the plot points denote one standard deviation from the mean.

As in the case of the cement paste, three mortar specimens were tested for each age for both the HDP and the RFT methods. The average total porosity of the specimen was measured to be 26%. The results of the permeability tests are graphed in Figure 25. It can be seen that the difference in permeability between the two tests in cement mortars is significant (over an order of magnitude). The values of average permeability measured from the two tests are tabulated in Table 2; the

average percentage difference between the permeability values obtained from the two test techniques is over 2000%.

Table 2 – Mean permeability values (units of m^2) measured in HDP and RFT tests for cement mortar.

Age	**HDP result**	**HDP SD**	**RFT result**	**RFT SD**
7 days	2.07E-18	1.87E-18	2.14E-17	1.07E-17
10 days	3.80E-20	1.6E-20	1.74E-18	5.90E-19
12 days	1.30E-20	8.6E-22	2.19E-19	6.25E-20
15 days	5.88E-21	1.67E-21	1.23E-19	5.67E-20
28 days	2.04E-21	1.19E-21	3.91E-20	1.05E-20

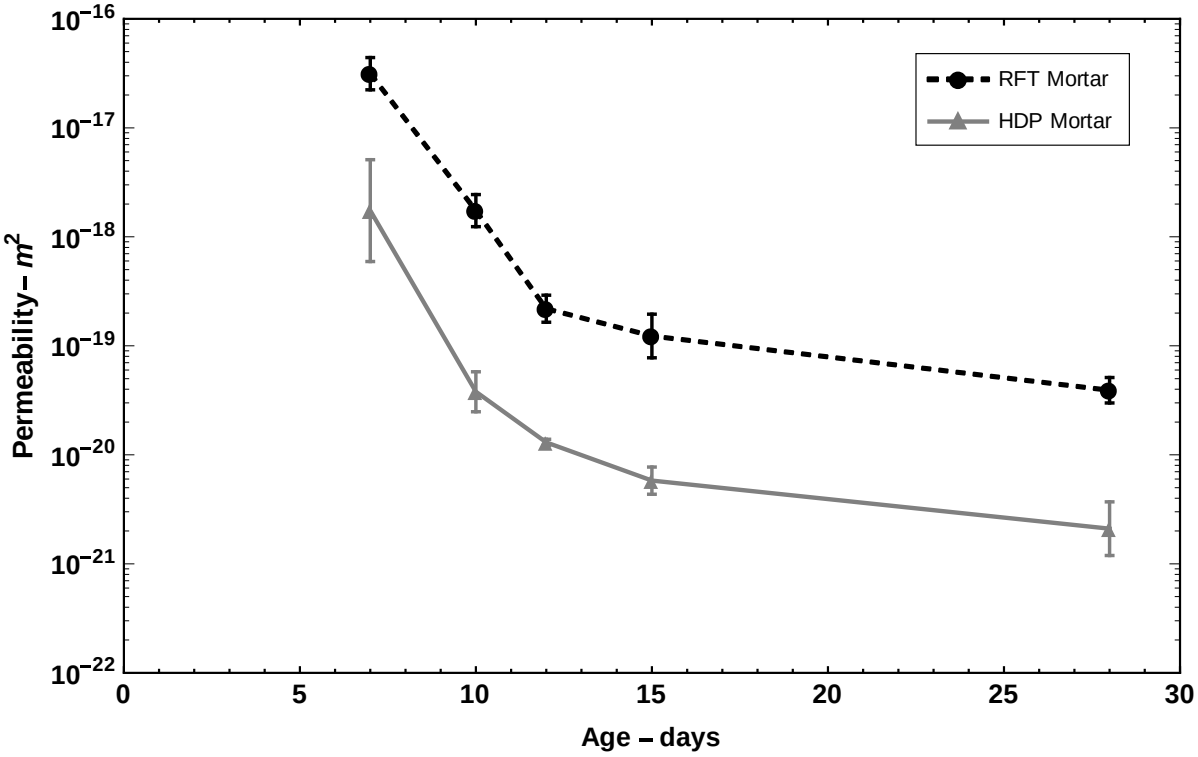

Figure 25 – Measured permeabilities obtained via HDP and RFT methods for **cement mortar** at different ages shows that the RFT method yields a significantly higher permeability than the HDP method. The error bars on the plot points denote one standard deviation.

For concrete, two specimens were tested for each age for both the HDP and the RFT methods. The average total porosity of the specimen was measured to be 20%. The results of the permeability tests are graphed in Figure 26. The difference in permeability between the two tests in concrete is more than that of the cement paste but less than that of mortar. The values of average permeability measured from the two tests are tabulated in Table 3.

Table 3 – Mean permeability values (units of m^2) measured in HDP and RFT tests for cement concrete.

Age	HDP result	HDP SD	RFT result	RFT SD
7 days	5.6E-19	2.3E-19	1.03E-17	1.7E-18
15 days	4.3E-20	2.8E-20	1.8E-19	6.7E-20
28 days	8.8E-21	9.21E-21	8E-20	5.06E-20

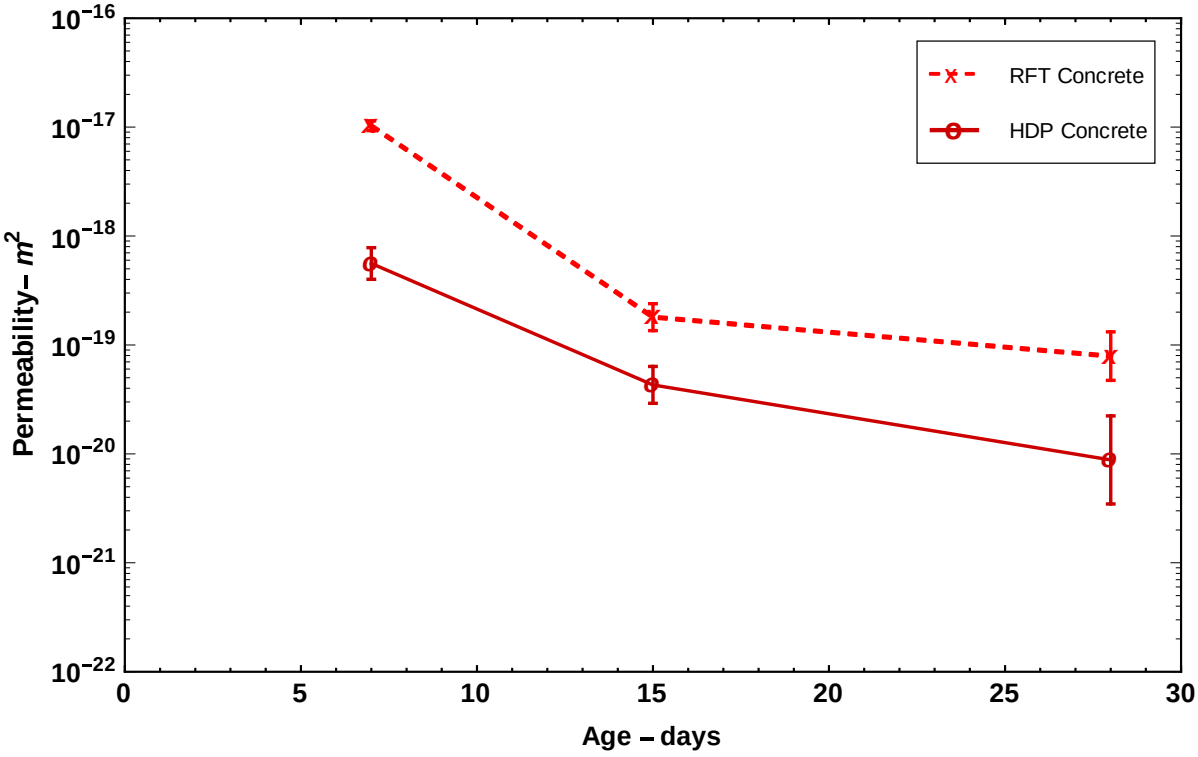

Figure 26 – Measured permeabilities obtained via HDP and RFT methods for **concrete** at different ages shows that the RFT method yields a higher permeability than the HDP method. The error bars on the plot points denote one standard deviation.

3.4 Discussion

The test results of the HDP and RFT measured permeabilities of the three materials (cement paste, mortar, and concrete) yield interesting implications. First, as previously shown, measurements of cement paste permeability obtained with HDP and RFT techniques are essentially equivalent. In the case of cement mortar and concrete we see an order of magnitude difference between the HDP and RFT tests. The HDP gives a lower permeability compared to the RFT tests. Furthermore, as shown in Figure 28, the permeability values obtained from HDP for the cement mortar are very close to the permeability values obtained for cement paste (via either HDP or RFT tests). Thus, the addition of fine aggregate to the cement paste matrix does not result in any significant changes in the kinetics of the poromechanical response but does result in a significant increase in the flux measured in the RFT test. We hypothesize that these results occur primarily because the pores added to the matrix by the introduction of the ITZ – which are larger than those in the paste matrix – have a much more significant effect on the flux *through* the sample (as measured via RFT) than the flux *into* the overall pore network (as captured via HDP). This is mainly because in the HDP technique, re-expansion (which is used to calculate flux) only fully occurs once all water accessible pores are pressurized. However, in the RFT method, the water seeks the easiest path to flow across the wall thickness of the hollow cylinder. The ITZ present in the mortar provides that easier pathway in the case of cement mortar. Expressed another way, in the HDP test the results tend to be dominated by the smaller pores in the matrix whereby in the RFT test the results are dominated by a select few larger pores or pathways present in the ITZ.

The HDP results of concrete however show a higher permeability result in HDP method and an even higher permeability values for the RFT method. The addition of coarse aggregates into the concrete matrix percolates the ITZ and increases the permeability of the HDP method and the percolation also creates more pathways for the fluid to flow across the specimen wall in the RFT method resulting in a higher permeability result.

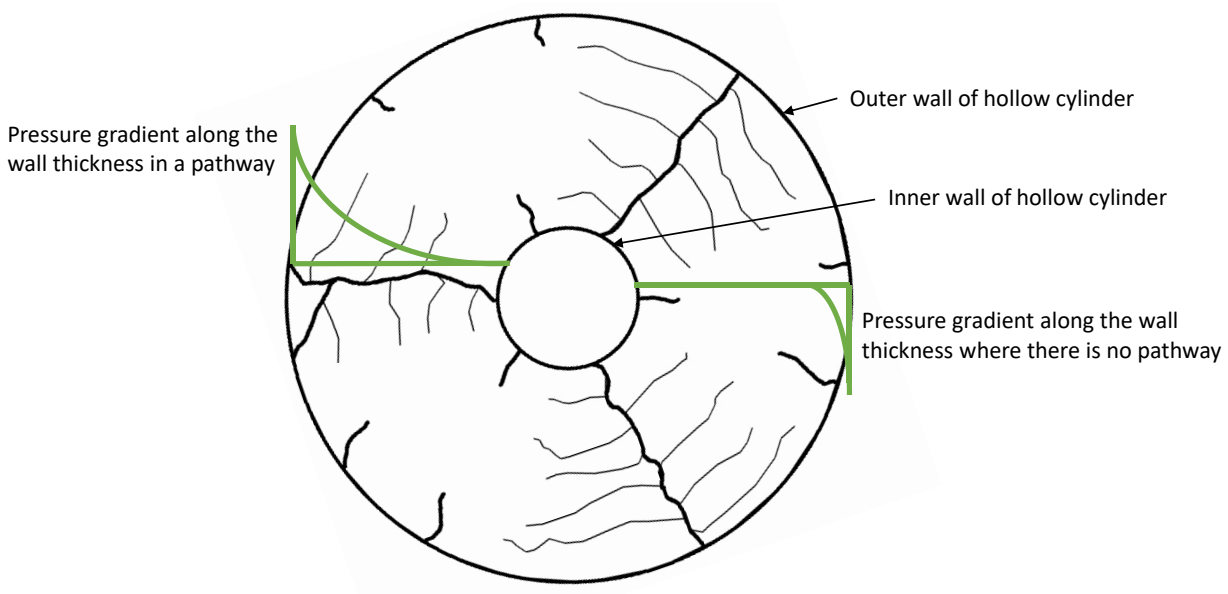

Figure 27 – Illustration of pathways and pore network along the cylinder cross section and how the pressure gradient changes along the wall cross section of the cylinder at a particular point in time after application of fluid pressure on the outer radial surface. The thick black lines represent pathways formed by interfacial transition zones in the mortar.

We suggest that difference in the HDP and RFT results will be the case for any material that has a multimodal pore network that consists of many small pores and a few larger, continuous pores or

pathways. In the case of cement mortar and concrete, the pore network in the hydrated cement and can be considered as one set of modes of the pore network distribution. The ITZ region between the aggregates and the hydrated cement paste would contribute to additional modes of the pore network distribution. The presence of these additional modes enables the creation of a pathway across the wall of the cylinder. Figure 27 shows a rough illustration of this hypothesized effect. The thick black lines depict the pathways created by the ITZ in the specimen. This can be caused by the addition of inclusions in a matrix like aggregates in cement paste or by damaging the specimen causing cracks. If there are a few large pathways that allow the permeating fluid to flow through the cylinder wall faster than the rate at which water flows into the smaller pore network, then the RFT will give substantially higher permeability values than HDP. Thus, in terms of the effect on the RFT measured permeability, the volume of the pores in the ITZ is deemed to be of less importance than the degree of interconnectivity of these pores.

The mortar results here indicate that the presence of ITZ (effectively microcracks in the mortar structure), that is not percolated, have little notable effect on the HDP response. However, Grasley et al. [51] argued that an observed order of magnitude increase in the permeability of a cement paste sample – measured by dynamic pressurization – previously subjected to hydrostatic tension greater than the tensile strength of the material was the result of the establishment of an interconnected network of microcracks. The cause of this hydrostatic tension was a result of depressurizing the pressure vessel by a step greater than the tensile strength of the material being tested. This caused tensile pressures to develop within the pore microstructure thus causing distributed damage throughout the entire specimen.

To reconcile the results of this work and those of Grasley et al. [51], it is important to note that the aggregate volume fraction of the mortars tested here was about 0.46. It has been suggested that percolation of the ITZ occurs once one has an aggregate volume fraction exceeding about 0.6 [Pincigallo, van Bruegel]. Thus, in the mortars tested herein, the ITZ did not establish a well-distributed, interconnecting pore network. Rather, it is likely that a few, select interconnected pathways were developed through the radial thickness of the material. These discrete pathways would have a significant impact on RFT and a much smaller impact on HDP. The aforementioned results and hypothesis are supported by work from Sant [99], who found that drying diffusion rate of cement paste (which is dictated strongly by transport out of the smallest pores) is minimally affected by the addition of aggregates up to a volume fraction of 0.5. In contrast, in the work of Grasley et al. cited above, the microcracking network established in cement pastes that were subjected to uniform hydrostatic tension was likely highly interconnected, well distributed, and uniform – in essence, a relatively large volume of relatively large interconnected pores was added to the pore network by the applied tension.

The aforementioned results establish that the HDP and the RFT tests provide different results in the case of mortar at aggregate volume fractions below the ITZ percolation threshold based on the measured effect of hydrostatic tension induced microcracking on dynamic pressurization measured permeability noted in [51]. It is not possible to achieve percolation in cement mortar as the amount of fine aggregates required to reach percolation would result in a mix that would not be workable enough to pour in the cylinder molds.

The permeability results of the concrete specimens show that the HDP permeability in the case of a percolated ITZ, is greater than that compared to cement paste or mortar as shown in Figure 28. The percolation also increases the RFT permeability compared to cement paste but comparable results to mortar.

The RFT values for mortar and concrete are much higher than that of cement paste. The HDP values of concrete are higher than cement paste and mortar. We hypothesize that the transport mechanisms for the two methods vary for each material. In the case of cement paste the capillary porosity dictates both the HDP and RFT tests. For mortar, capillary porosity dictates HDP and a few discrete connected pathways dictate RFT. However, for concrete the capillary porosity and percolated ITZ concurrently control HDP results and RFT is controlled by the interconnected pathways.

Hydration also plays an important role in the results. It affects concrete more in RFT than HDP. For cement paste and mortar hydration affects the results of the two tests similarly.

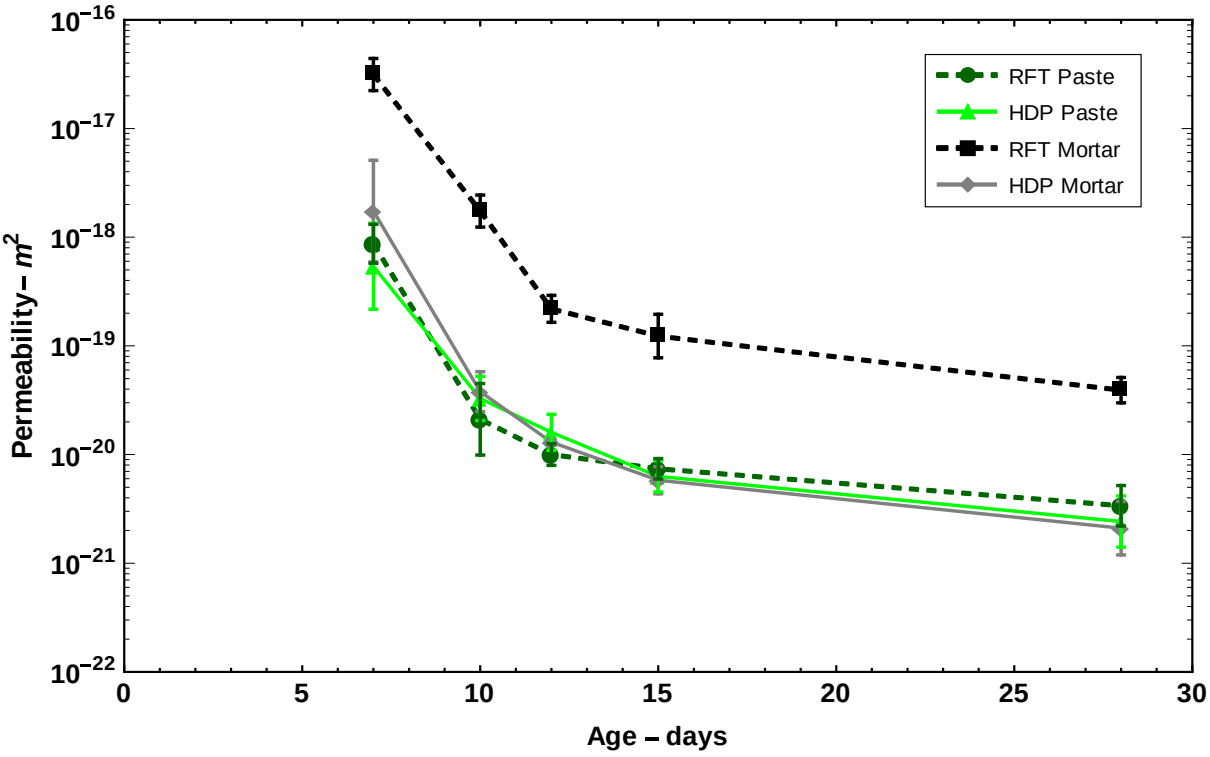

Figure 28 – Comparison of paste and mortar results for HDP and RFT show that the HDP values for cement mortar are essentially equal to the HDP and RFT permeability values obtained for cement paste. The RFT measured permeability on the mortar, however, is more than an order of magnitude greater. The error bars on the plot points denote one standard deviation from the mean.

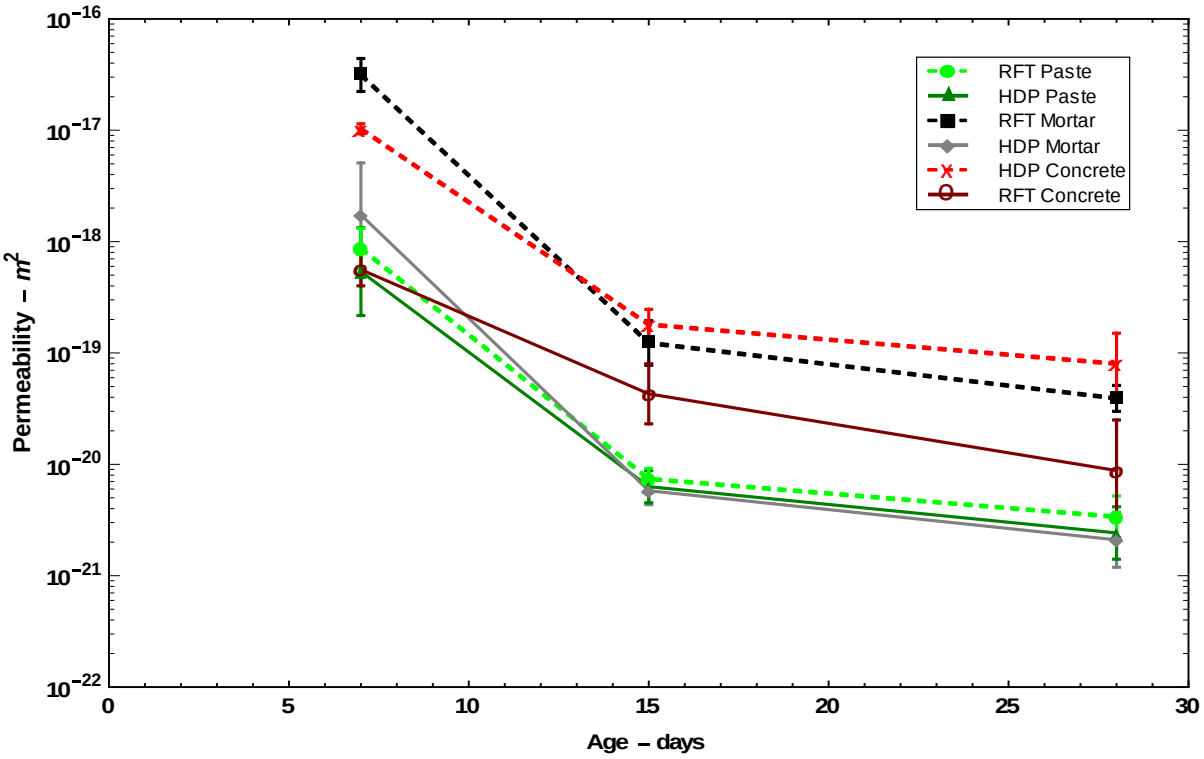

Figure 29 – Comparison of paste, mortar and concrete results for HDP and RFT show that RFT values for concrete are essentially the same as mortar but the HDP value of concrete is higher than that of mortar. The error bars on the plot points denote one standard deviation from the mean.

The RFT method measures the fastest rate at which a fluid can flow through a given section of material. The transport property of the cementitious matrix dictating fluid flux through a material is essential when evaluating durability problems like corrosion of steel rebar. Corrosion happens in the presence of water and chloride ions, so the rate at which water and ions can reach rebar (by flowing through a section of concrete) is important. The HDP method, on the other hand, determines a material resistance to fluid flow into the entire pore network of the material. The transport property dictating fluid flux into the small pores is essential when calculating evaluating

chemical durability problems like sulfate and chloride attack that are well-distributed in the microstructure.

3.5 Conclusions

The measured permeabilities obtained from the poromechanical HDP method and the RFT method were compared for both cement paste, mortar and concrete. The two methods allow evaluation of a material resistance to pressurized fluid flow *into* (HDP) and *through* (RFT) a sample. For the first time, it was shown that for mortars and concrete, the material resistance to these two different pressurized fluid flows are different. The primary results are:

- For cement pastes, the permeabilities measured using the HDP and the RFT method are equivalent, indicating that the resistances to flow into and flow through cement paste are equivalent.

- For a mortar with an aggregate volume fraction of about 46%, the permeability measured via RFT was about an order of magnitude greater than that measured via HDP (which was equal to the paste permeability). This result indicates that the presence of the aggregates served to increase the flow through the material but did not significantly affect the flow into the material.

- For concrete with an aggregate volume fraction of about 62% the permeability measured via RFT was greater than that measured via HDP (which was greater than the paste and

mortar permeability). This result indicates that percolation of ITZ increases the flow into the material while the flow through the material is similar to that of mortar (pathways dominating the permeability).

The significant difference in the resistance to permeation through and into the pore network of the mortar and concrete were attributed to the development of a few discrete transport pathways through the radial cross section by the ITZ. For mortars, the ITZ is likely not fully percolated such that only a few continuous pathways through the material are developed. For concrete the ITZ is fully percolated and this increases the flow into the cross section of the material while the flow across the material is still comparable to that of mortars where ITZ is not percolated.

The fact that mortars and concrete may have a different resistance to permeation through or into the pore network is of practical importance to the myriad durability problems plaguing cement-based materials. As certain durability problems are dependent on moisture or ion penetration throughout the pore network (e.g., sulfate attack or leaching) and other problems (e.g., corrosion) are dependent on passage or moisture or ions through a section of material, the choice of the test method to evaluate such resistance becomes critically important. For example, the utilization of HDP to quantify the resistance to corrosion may lead one to dramatically under predict the flux that reaches reinforcing steel if there are discrete cracks or pathways present. In contrast, the use of RFT or other conventional flow-through tests to quantify permeability may lead one to overestimate the rate at which moisture or ions can permeate into and through the smallest pores, as may be necessary to induce sulfate attack or leaching.

4 ACCELERATED AUTOGENOUS HEALING

The primary focus of this study was to test the viability of autogenous healing as a viable method to heal/repair damaged cement mortar pipe sections. The damage in these sections were induced in a controlled manner which could be replicated to provide a consistent observation. The two types of damage that was focused on in the study were cracking and decalcification. The derogatory effects of cracking and decalcification has been discussed in detail in chapter 2. The permeability of the hollow pipe section specimens is used as a metric for determining the amount of damage that in the specimens.

Controlled decalcification was performed by treating the hollow pipe section cement mortar samples by exposing it to 6M ammonium nitrate solution. Controlled cracking was performed by freeze cracking where the hole in the middle of the specimen was filled with water and allowed to freeze. The difference of the thermal coefficients between the water and cement mortar caused thermal stresses large enough to form cracks. The results obtained from the study comparing poromechanical and traditional flow through permeability test methods were important in choosing the permeability tests required to measure the degree of damage caused by cracking and decalcification. Cracking damage creates a short circuit in the walls of the hollow pipe section specimen. Decalcification damage opens up the pore network of the matrix and creates a distributed damage network in the matrix of the specimen. Since the effects of the two types of damage are different on the specimen transport network different permeability measurements are needed to quantify the damage accurately. Poromechanical method (HDP) was used to measure permeability gain from decalcification damage as it takes into account the complete pore network

of the specimen. The flow through method (RFT) was used to quantify permeability gain from cracking damage as it measures the highest permeability possible in the network which is caused by the presence of cracks in the system.

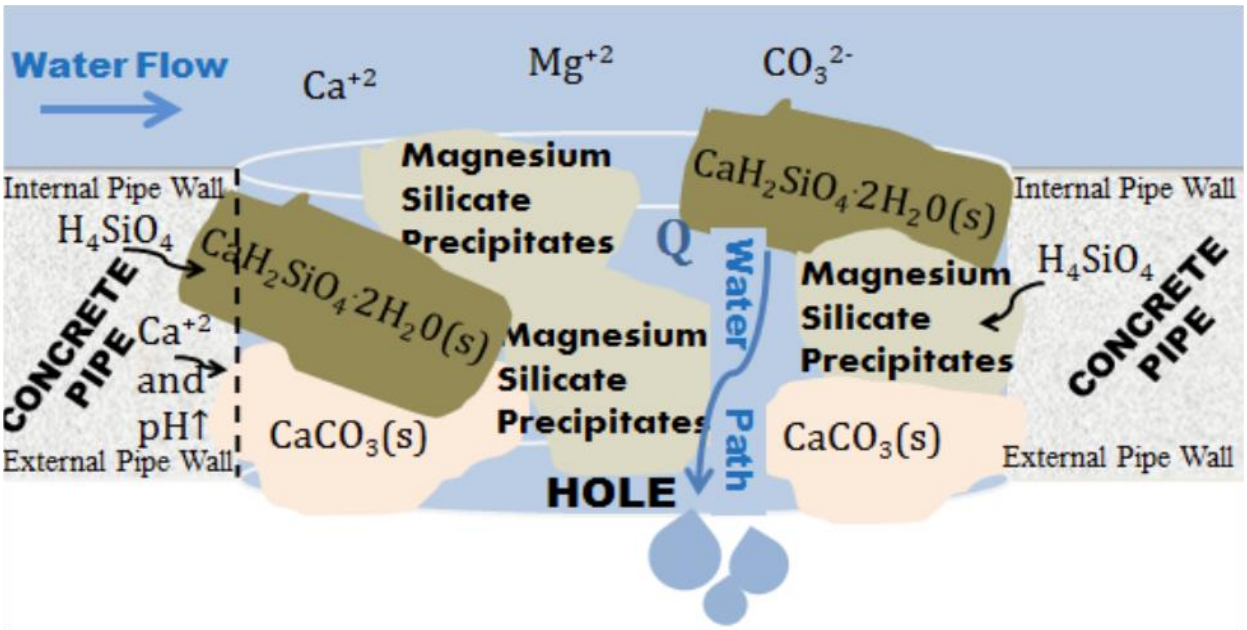

Figure 30 – Schematic showing the leak trajectory with the precipitation kinetics of the healing precipitates. Calcium Silicates and Magnesium Silicates are cement hydration products. Calcium carbonate is the main precipitate for the healing solution.

Previous research has demonstrated that the chemistry of water passing through the leak, can be an overarching control factor, that determines whether leaks grow larger or end up self-repairing [28, 29]. Here, we test the hypothesis that accelerated healing of lab scale concrete water distribution pipes may be achieved by adjusting the water's saturation index of $CaCO_3$. Figure 30

shows a graphic representation of the leak water path and how the precipitates clog up the leak and attempt to heal the damage in the pipe. The hypothesis is evaluated by direct measurements of permeability of the walls of miniaturized, damaged concrete pipe sections both before and after flowing the supersaturated healing water through the sections for fixed time periods.

4.1 Specimen preparation

For this study cement mortar specimens were used. Controlled cracking and controlled decalcification were induced in the cement mortar specimens. Regular Type I/II cement was used along with river sand passing 100% through the No.16 sieve as fine aggregate. A water-to-cement mass ratio of 0.5 and an aggregate-to-cement mass ratio of 2 was used in the sample preparation. The sections used to induce crack damage had 1.5% PVA microfibers by mass of cement to ensure that the samples remained intact after the cracks had formed. The lab scale pipe specimens used in the study had the following dimensions: 25.4 mm (1 in) outer diameter, 6.35 mm (0.25 in) inner diameter, and 50.8 mm (2 in) length. Figure 31 shows the cross section and top views of a sample specimen and shows a pipe section specimen with the end plates attached.

The cement mortars were prepared per ASTM C305-14[100]. The samples were prepared by pouring the mortar mix into 25.4-mm inner diameter polycarbonate tube molds. The hole in the middle was made by using a 6.35-mm polyethylene tube. The ends of the molds were sealed using 25.4-mm steel washers with a 6.35-mm hole. After casting, the samples were maintained at room temperature (20°C) in sealed condition and then demolded after 24 hours. After demolding the pipe sections, steel end plates (with threaded center holes) were attached to both ends to allow connectivity to a hose.

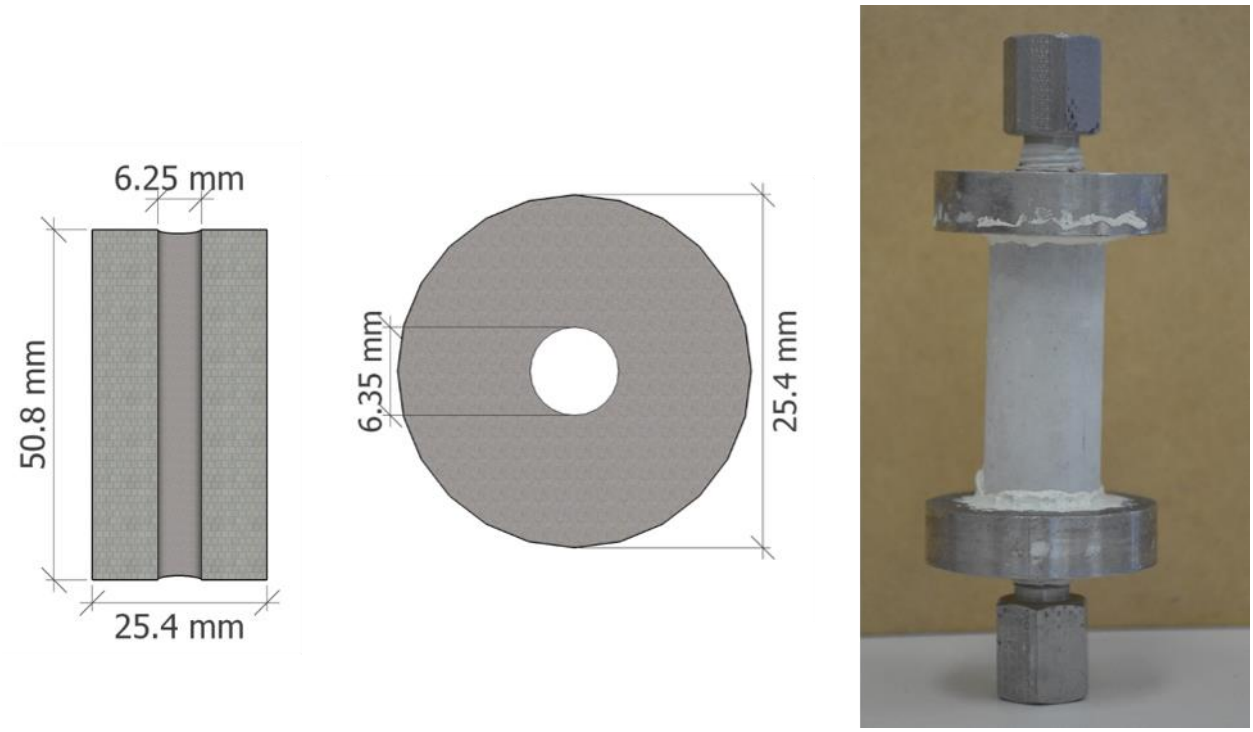

Figure 31 – Cross section and top view of the pipe section specimens. Dimensions of the specimens are 25.4 mm outer diameter, 6.35 mm inner diameter and 50.8 mm in height. On the right is a pipe section specimen prepared for decalcification and cracking with end plates attached with a marine epoxy.

4.2 Controlled decalcification

Accelerated decalcification of the cement mortar specimens was needed to simulate different levels of decalcification in a real-world scenario. The reaction of ammonium nitrate with the calcium hydroxide in the microstructure is significantly faster than deionized water as shown by (2) and (3). The cement mortar samples were cured for 28 days in a saturated lime water solution to improve the degree of saturation and to prevent calcium hydroxide leaching out during the

curing period. The mortar samples were then exposed to different periods of time, varying from 24 hours to 120 hours, to 6M ammonium nitrate solution to allow for different levels of decalcification. Exposure to the ammonium nitrate solution was controlled in a way that only the outer radial surface of the specimens was in contact with the solution. By controlling the exposure, the depth of decalcification within the specimen was also controlled.

The cement mortar pipe section specimens were tested for permeability using the HDP method. HDP method was chosen for decalcification damage because the damage is not focused in a single point and is spread out through the entire microstructure of the specimen. Results obtained from the HDP technique show the permeability of water into the pore network of the specimen thereby providing an accurate depiction of the degree of decalcification that has occurred in the specimen. Five sets of three specimens for each exposure time were tested for permeability and the results of the testing are graphed in Figure 32. From (3) that the amount of ammonium nitrate exposure time needed to fully decalcify the specimens was estimated to be 120 hours. From the results, 120 hours of decalcification shows up to 2 order change in permeability compared to 24-hour decalcification. For this study, all decalcified specimens were exposed for 120 hours to ensure complete decalcification on the pipe section specimens. Table 4 shows the permeability results and the standard deviations for decalcification tests.

Table 4 – Mean HDP permeability values (units of m^2) measured for the specimens with varying amount of exposure to ammonium nitrate solution (exposure time in hours).

Exposure Time	HDP Permeability	Standard Deviation
24	9.48×10^{-21}	2.03×10^{-21}
48	1.20×10^{-19}	4.68×10^{-20}
72	2.12×10^{-19}	1.20×10^{-19}
96	3.15×10^{-19}	9.66×10^{-20}
120	1.03×10^{-18}	4.69×10^{-19}

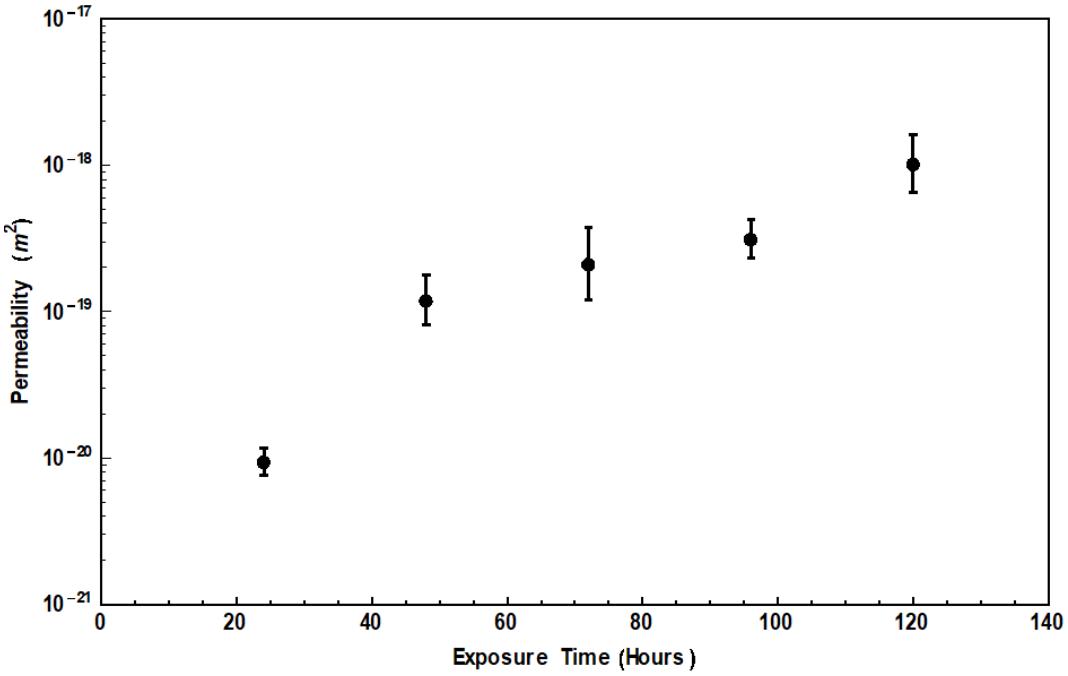

Figure 32 – Measured permeability of the pipe section specimens (m^2) vs the exposure time to ammonium nitrate solution (hours) show that permeability of the decalcified samples increase of several orders magnitude when completely decalcified.

4.3 Controlled cracking

Controlled radial cracks were introduced into the pipe section specimens by freezing water in the middle hole of the cylinders. One end of the specimen was sealed water tight and then the middle hole of the specimen was filled with water. The specimen was then placed in a temperature and humidity environmental test chamber at -20℃. As the water in the middle reached freezing temperature it expands to cause radial stress on the walls of the hollow cylindrical specimen. When the applied radial stress exceeds the strength of the specimen, cracks start to form. Several freeze thaw cycles were required to form cracks big enough. The idea was to create cracks big enough to be visible to the naked eye without the cylinders breaking apart. These cracks would cause significant leaks when water flowed through them.

The cracked specimens were tested for permeability with the RFT method. Unlike decalcification cracking is a localized damage effect. Therefore, RFT method for testing permeability is more suitable as it measures the permeability of water across a material. Results obtained from RFT method give us an accurate depiction of how big the cracks are and how much leakage will occur through those cracks.

Three sets of three specimens for each exposure time were tested for permeability and the results of the testing are graphed in Figure 33. Three different levels of cracked samples were tested and compared for the permeability. From the results, it was observed that experimental variance of permeability for one freeze-thaw cycle was too high and the variance for 3 cycles of free thaw showed consistent permeability results. Therefore, 3 cycles of freeze-thaw3 cycles of freezing and

thawing was chosen as the optimal amount of cracking required to give consistent permeability changes compared to un-cracked specimens. Another interesting observation was that the permeability did not increase after the third freeze thaw cycle as the specimens were too permeable to hold the freezing water in the middle hole of the hollow cylindrical specimen. Table 5 shows the values of the RFT permeability along with the standard deviation.

Table 5 – Mean RFT permeability values (units of m^2) measured for the specimens cracked with varying amounts of freeze thaw cycles.

No of Freeze Thaw cycles	**RFT Permeability**	**Standard Deviation**
1	5.64×10^{-21}	1.51×10^{-17}
2	7.85×10^{-19}	8.01×10^{-16}
3	3.55×10^{-19}	1.72×10^{-15}

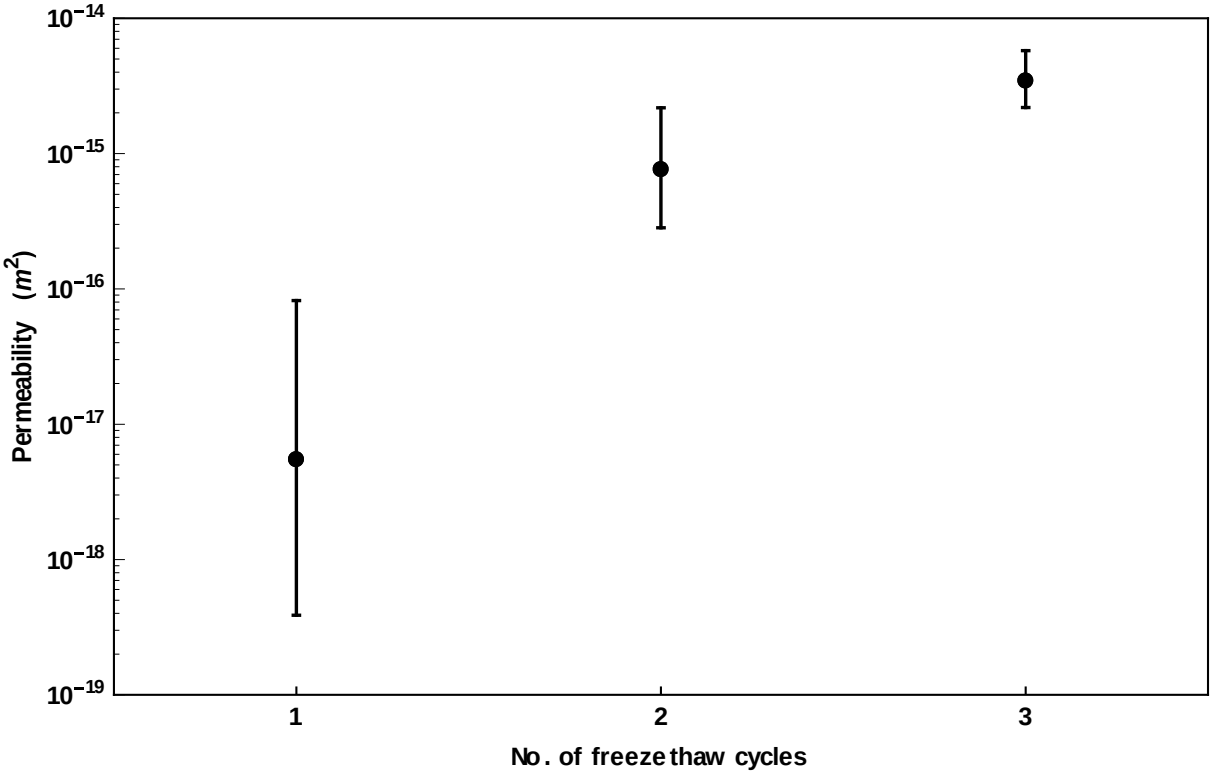

Figure 33 – Measured permeability of the pipe section specimens (m^2) vs the number of freeze thaw cycles show that permeability of the decalcified samples increase of several orders magnitude when completely decalcified.

4.4 Healing rig

The healing rig comprises of a submersible pump capable of pumping water from a reservoir into four 6.35 mm (0.25 in) diameter tubes at a flow rate of 0.6 m/s (2 ft/s). Each flow path is attached to a damaged specimen. The other end of the damaged specimen is connected to tubes which take the flow back into the healing water reservoir. Figure 34 shows image of the rig in action.

Figure 34 – Healing Rig – comprises of a reservoir of the healing water which is pumped through the pipe section specimens by a submersible pump at a flow rate of 0.6 m/s.

4.5 Healing solutions

Four simulate potable waters were designed to examine extremes of calcium carbonate saturation that could be encountered in potable water. Water #1 was a synthesized drinking water with only Ca^{2+}, which lacked any of the naturally occurring inorganic carbon (i.e., HCO_3^-, CO_3^{-2} needed to form $CaCO_3$ after reacting with CH (Table 1). Water #2 used only Ca^{2+} added to a water with a moderate level of inorganic carbon, to a point where the water is just at saturation with $CaCO_3$. . Water #3 included enough Ca^{2+} and inorganic carbon such that the water is slightly supersaturated, giving an increased probability of precipitating solids if in contact with a suitable surface but which would not form CaCO3 in the feed solution whereas water 4 had 5-15 mg/L solid present. Table 6 shows the compositions of the different healing waters.

Table 6 – Composition of the four different healing solutions.

Water	**[$CaCl_2$] (mmol/L)**	**[$NaHCO_3$] (mmol/L)**	**NaCl (mmol/L)**	**pH_{1day}**	**Suspended solid conc.**	**Description**
Control	0	0	0	7	--	Drinking water without any added ions.
#1	0.87	0	1	7.63	--	A synthesized drinking water with only Ca^{2+}.
#2	0.87	0.87	1	8.33	--	Same as #1, but with Ca^{2+} added to a point where the water is just at saturation (no precipitate).
#3	1.30	1.30	1	7.65	--	Same as #2, but with enough Ca^{2+} added, to a point where the water is slightly supersaturated. There is a high probability of precipitates forming on contact with suitable surface.
#4	1.80	1.80	1	7.71	~12.5 mg/L as $CaCO_3$	Same as #3, but with more Ca^{2+} added, so there is obvious precipitate in the water of say 10-15 mg/L.

4.5.1 Decalcification healing

Five sets of four decalcified samples were prepared for healing with the 4 different healing solutions and the control solution. The healing solutions were run through the decalcified samples for 72 hours. The specimens were tested for permeability, using the HDP method, before and after healing. The results for the different healing waters were graphed in Figure 35.

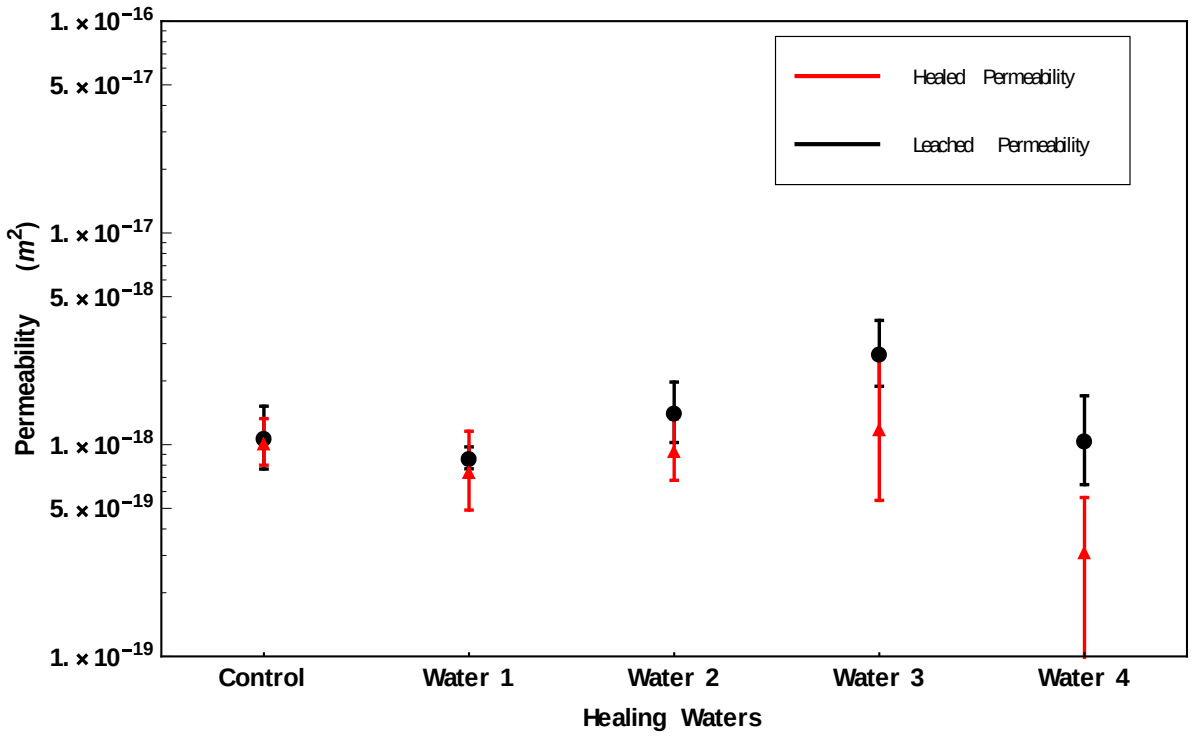

Figure 35 – Measured HDP permeability of damaged pipe section specimens before and after healing for the control and 4 healing waters show that waters 3 and 4 show most decrease in permeability after healing.

Table 7 – Mean HDP permeability values (units in m^2) measured before and after healing of the decalcified specimens.

Solution Used	Damaged Permeability	Standard Deviation	Healed Permeability	Standard Deviation
Control	1.08×10^{-18}	3.68×10^{-19}	1.03×10^{-18}	2.61×10^{-19}
Water 1	8.67×10^{-19}	1.03×10^{-19}	7.54×10^{-19}	3.23×10^{-19}
Water 2	1.42×10^{-18}	4.68×10^{-19}	9.48×10^{-19}	3.17×10^{-19}
Water 3	2.7×10^{-19}	9.66×10^{-19}	1.20×10^{-19}	9.46×10^{-19}
Water 4	1.05×10^{-18}	5.07×10^{-19}	2.15×10^{-19}	2.07×10^{-19}

From the results shown in Table 7, it can be seen for the decalcified samples Water 3 and Water 4 show the most promising results. Permeability reduction of a factor or 3.5 was observed in the case of Water 4. It is interesting to note that both the healing waters 3 and 4 were supersaturated with Ca^{2+} ions.

4.5.2 Cracked healing

Five sets of four freeze-thaw cracked samples were prepared for healing with the 4 different healing waters and the control solution. All the healing solutions were run through the decalcified samples for 72 hours. The healed samples were tested for permeability using the RFT method. The results for the different healing waters were graphed in Figure 36

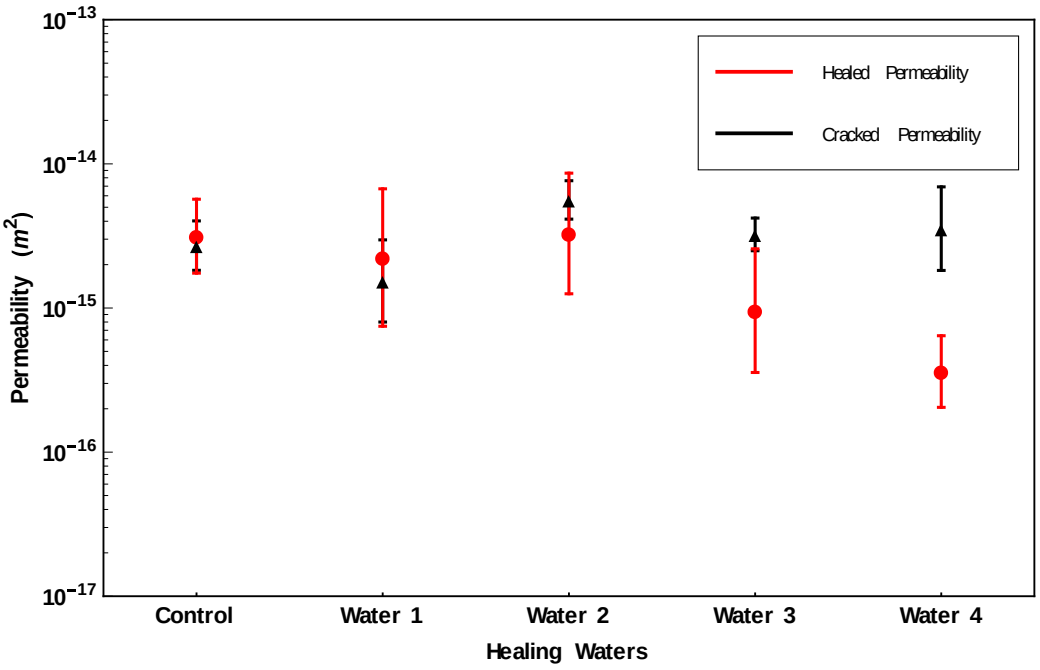

Figure 36 – Measured RFT permeability of damaged pipe section specimens before and after healing for the control and 4 healing waters show that waters 3 and 4 show most decrease in permeability after healing.

From the results shown in Table 8, it can be seen that the Control and the first 2 healing waters do not show any significant reduction in the permeability of the cracked samples. However, the healing waters 3 and 4 show a decrease in the permeability for the healed samples with Water 4 showing the maximum reduction in the permeability. Permeability reduction of a factor or 12.5 was observed in the case of Water 4.

Table 8 – Mean RFT permeability values (units in m^2) measured before and after healing of the cracked specimens.

Solution Used	Damaged Permeability	Standard Deviation	Healed Permeability	Standard Deviation
Control	2.71×10^{-15}	1.07×10^{-15}	3.15×10^{-15}	1.86×10^{-15}
Solution 1	1.54×10^{-15}	1.01×10^{-15}	2.24×10^{-15}	2.46×10^{-15}
Water 2	5.62×10^{-15}	1.72×10^{-15}	3.29×10^{-15}	3.17×10^{-15}
Water 3	3.24×10^{-15}	8.46×10^{-16}	9.58×10^{-16}	9.46×10^{-16}
Water 4	3.55×10^{-15}	2.37×10^{-15}	3.62×10^{-16}	$2.07x\ 10^{-16}$

The permeability results obtained from the cracked and healed specimens for both damage types (i.e., decalcification and cracking) are promising. We observe that the permeability of the healed samples decreased compared to the damaged samples for healing waters #3 and #4. For healing waters #1 and #2 we observe that the permeability of the healed specimens is relatively close to the damaged permeability.

In the case of cracking damage, we observe that the healed samples show over an order magnitude reduction of permeability when healed with water #4. Healing water #3 resulted in a permeability decrease by a factor of 3.4. Healing waters #1 and #2 show minimal reductions in permeability for the flow rate and healing duration considered in this work. Thus, we conclude that the supersaturated solutions are needed to see any meaningful change in the values of permeability in the case of cracked specimens, at least for the crack sizes and healing duration and flowrates considered in this work.

In the case of decalcification damage, a similar trend as in the case of cracked specimens is observed. The permeability decrease for healing waters #3 and #4 are higher than the decrease for healing waters #1 and #2. However, we see that the permeability decrease for even healing water #4 is just by a factor of 3.5. Healing water #3 resulted in a permeability decrease by a factor of 2.25. Thus, we conclude that in the case of decalcification damage the healing effects of the waters are not as prominent as in the case of cracking damage.

The permeability results comparing an undamaged specimen, a leached specimen, and a cracked specimen is graphed in. Comparing the permeabilities of specimens subjected to the two different damage types indicates that cracking is a much bigger threat to cause leakage in a water distribution system compared to decalcification. Cracked samples have a higher permeability than decalcified samples because they have a direct pathway through the pipe section for the water to flow across. In the case of decalcified samples, the damage induced increases the size of the pore network within the specimen which increases the permeability, but it is a much more distributed damage than the few discrete pathways created via cracks. Since permeability scales roughly with the cube of crack width [101], a few larger, discrete cracks will tend to increase permeability much more than a coarsening of pores (which is equivalent in effect to numerous very small cracks). However, decalcification and cracking are not discrete events. Complete decalcification of concrete leads to further cracking. Thereby healing decalcified concrete sections indirectly contribute to the longevity of the pipe section's life.

4.6 Conclusion

The technique of autogenous healing for restoring permeability of damaged cement mortar pipe sections was explored. An accelerated healing technique was used by altering the water chemistry of potable water flowing through these sections. Four different healing waters were used and the pipe sections were subjected to these healing waters for 72 hours. The types of damage considered for the study were cracking and decalcification. The cement mortar samples were damaged in a controlled manner and then tested for permeability before and after healing. The primary results obtained are:

- The difference in permeability between undamaged and damaged sections were compared between two damage types: controlled cracking and decalcification. Cracked sections saw a significantly higher permeability increase compared to decalcified sections.

- The permeability tests revealed that supersaturated healing waters decreased the permeability of the damaged pipe sections.

- Healing waters that were supersaturated with calcium were more successful at reducing permeability than the waters that were not supersaturated.

- Cracked sections that were healed showed a permeability decrease up to a factor of 12.5.

- Decalcified sections that were healed showed a permeability decrease up to a factor of 3.5.

The method of inducing accelerated autogenous healing by altering potable water chemistry has been shown to effectively reduce the permeability of both cracked and decalcified samples. The results also show that cracking is a more significant risk for causing water leaks in concrete or mortar pipe sections compared to decalcification.

5 IMAGE AND SURFACE ANALYSIS

The permeability results confirmed that the healing solutions have a positive effect on damaged pipe section specimens both in cracking and decalcification. The next step was to determine the mechanics of healing in the pipe section. Theoretically calcium carbonate in crystalline form (calcite) should be deposited in the damaged areas of the specimens and thereby healing the damage. The objective behind this part of the study is to determine the mechanism of how the precipitation of the calcite occurs in the hollow cylindrical pipe section specimens during the healing process. X-ray computed tomography (CT) has become increasingly popular to reconstruct 3d images of specimens in a non-destructive method. X-ray CT analysis will be employed to see if the calcite precipitates are visible in the cracked regions of the specimens. Scanning Electron Microscopy (SEM) in tandem with Electron Dispersive Spectroscopy (EDS) will be then used to identify the elemental distribution of the precipitates and to accurately determine the locations of the calcite precipitation.

5.1 X-ray CT imaging

X-ray computed tomography (CT) is a non-destructive imaging and characterization technique where x-rays are used to construct a virtual 3-dimensional model of an object. X-rays are passed through the object and a detector receives them and creates a series of 2-dimensional projections of the objects as projection images. These projection images are processed through tomographic reconstruction a series of 2-dimensional slice images of the object is obtained. X-ray CT method

provides 3-D images of the sample scanned as 2-D slice images. Using image manipulation software these images can be stacked to create a 3-dimensional model.

5.1.1 Sample preparation

The samples prepared for X-ray CT analysis had to be oven dried to minimize distortions and errors in the resulting images produced. The cracked specimens were tested for permeability using Radial Flow Through (RFT) test and then oven dried at 105℃ for 24 hours. The oven dried specimen was then scanned and imaged using the X-ray CT machine. The scans typically take 24 to 30 hours to completely scan the sample. The sample is then run through the healing rig for 3 days to complete the healing process. After the healing process is completed the sample is tested for permeability again using the RFT. The sample is then oven dried again. to remove the moisture from its pores, scanned and imaged using the X-ray CT machine. The two sets of images obtained before and after healing are run through an image processing routine for further analysis.

5.1.2 Image pre-processing algorithm

The reconstructed image slice obtained from the X-ray CT scans are run through a series of Mathematica routines to help isolate the damage in the specimens and to compare the cracked region before and after healing.

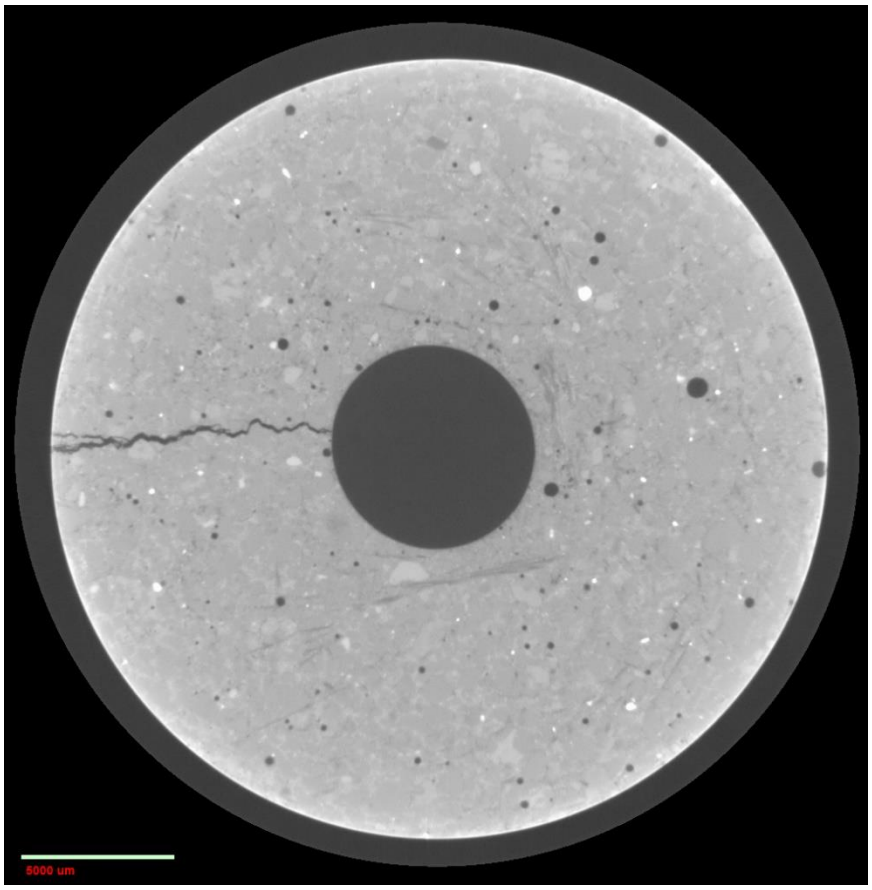

Figure 37 – Raw image slice obtained from tomographic reconstruction of the X-ray CT scan process.

Figure 37 shows a raw image obtained from the X-ray CT scan. The Image slices are first run through a grayscale conversion routine. This changes all the color in the images to grayscale ranging from 0-255. 0 represents black and 255 represents white. The Mathematica function used for the conversion to Grayscale is called ColorConvert. Figure 38 shows a grayscale converted image.

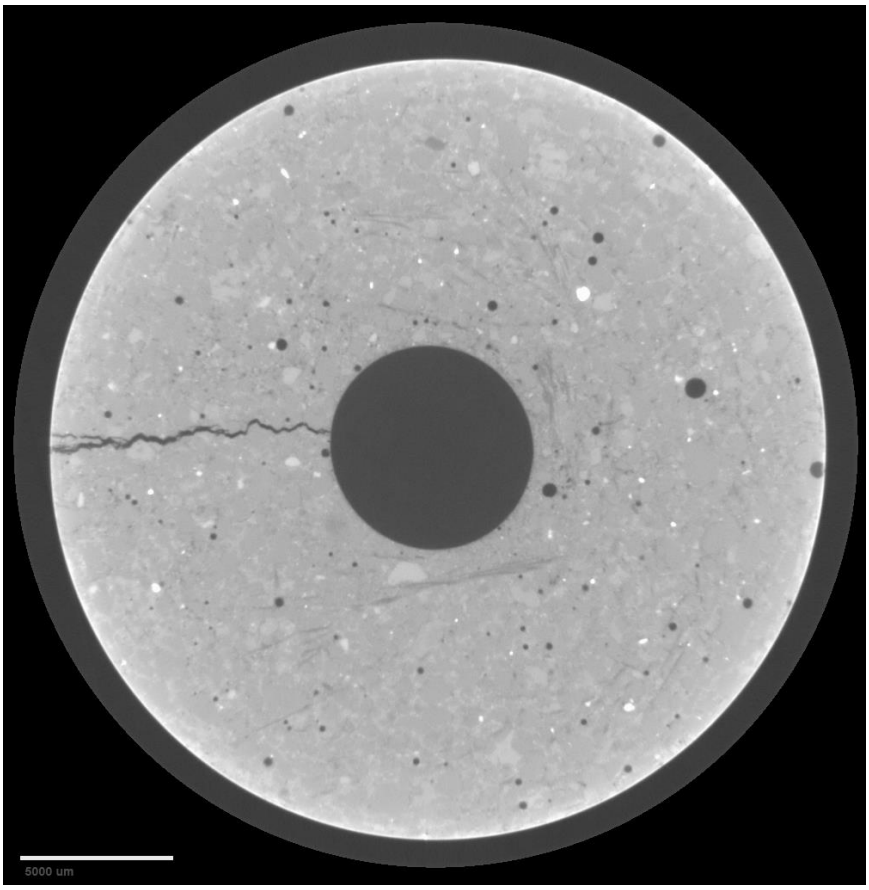

Figure 38 – Image obtained after running though the ColorConvert function in Mathematics to convert the colored image to Grayscale.

After grayscale conversion the images are adjusted for histogram distribution. The color histogram for each image is obtained and peak values are compared. If there is a difference between the peaks the distribution is adjusted to have matching histogram peaks. This process is essential when comparing similar images as different values of histogram peaks could lead to errors when comparing similar images. The Mathematica function ImageLevels is used to obtain the pixel values and counts for each image channel. By using 256 channels as the function parameter we can get the pixel values and counts for each grayscale number of the image.

The location of the highest peak of the histogram of a reference image is then determined and compared with the other images in the set. The histogram peak locations of the other images are adjusted to fall in line with the location of the peak in the reference image. The corrected set of images is saved separately on the disk drive. Figure 39 shows the image corrected for histogram and its scale removed using the DeleteSmallComponents function of Mathematica.

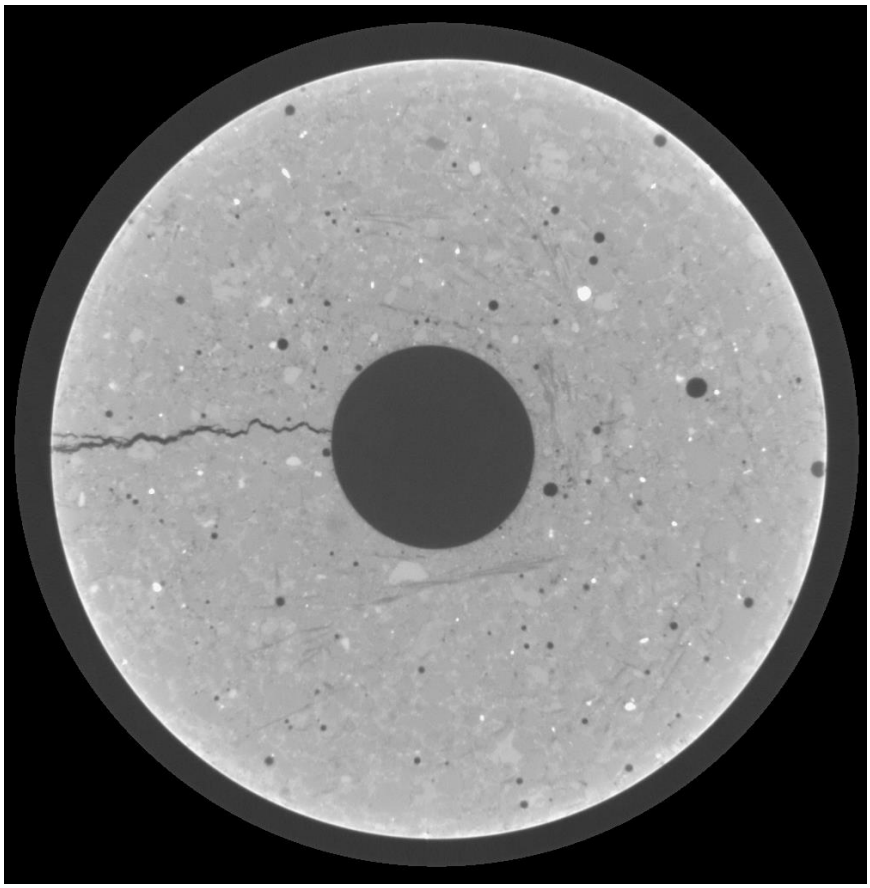

Figure 39 – Image adjusted for Histogram correction in mathematica and then run through DeleteSmallComponents function to remove the scale.

The set of images are run through a routine to crop out the middle hole and the outer region to remove the noise from the X-ray CT scans. Figure 40 shows a cropped image that is ready for the post processing routine.

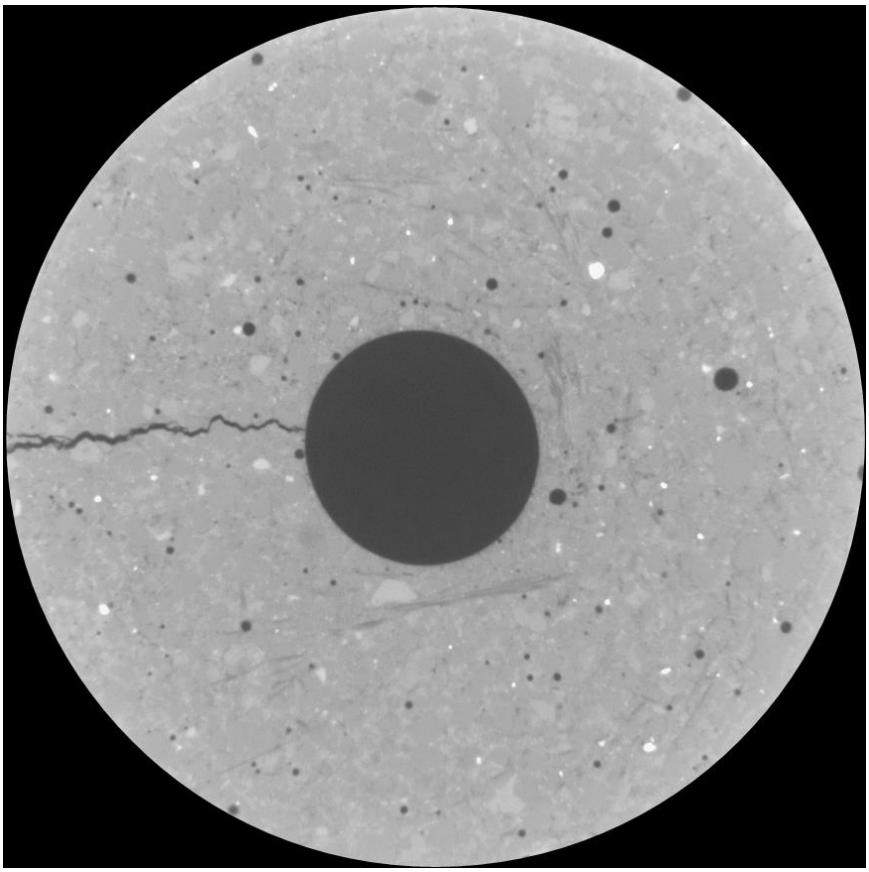

Figure 40 – The histogram adjusted image is cropped to ensure only the specimen area is utilized for the post processing routine.

The image is then binarized into black and white by using a predetermined threshold value. The histogram correction is significantly important to have same thresholds on every image that is

being compared. The Binarize and Threshold functions of Mathematica are used perform this action. Figure 41 shows an image that has been Binarized into black and white using a threshold of at a graylevel of 166. This level was chosen as it provides more clarity in the cracked regions of the specimen though we lose some clarity around the middle hole of the specimen.

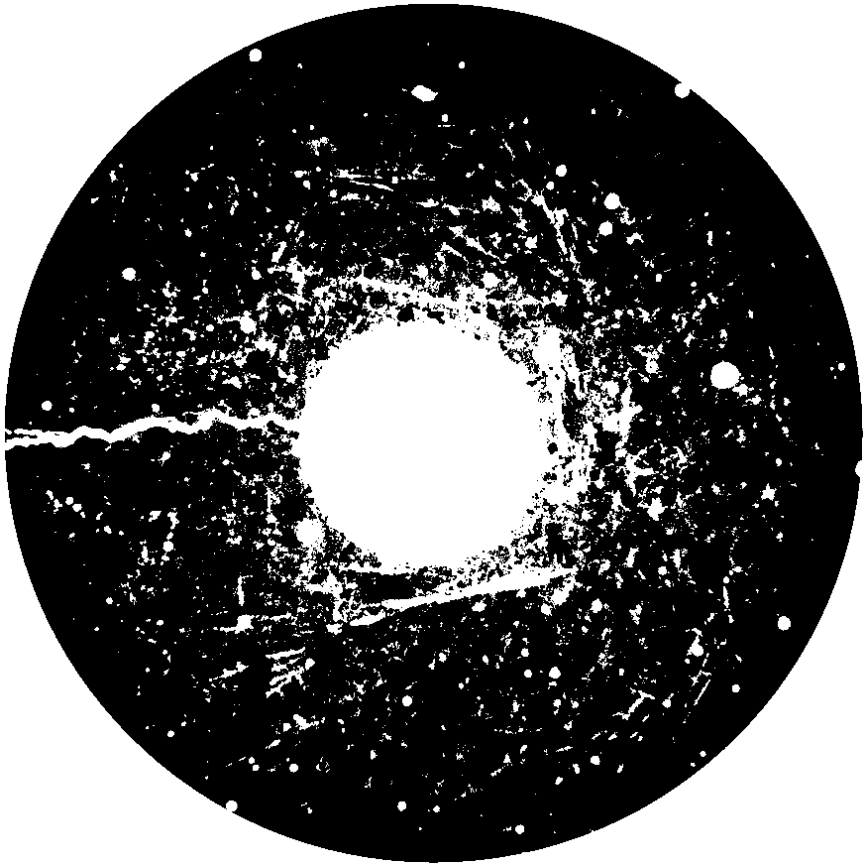

Figure 41 – Preprocessed image that has been converted into black and white (Binarized) at a graylevel of 166.

The binarized image is then run through another routine to change the outer section and the middle hole in the image slice to the background color. This is achieved by using MorphologicalComponents function in Mathematica. The function provides an output of the pixel values of connected features in an image. So, all the holes will be treated as individual components. Using the ReplacePixelValue function of Mathematica part these individual components can be changed to the background color and thereby it serves 2 purposes. Firstly, the middle hole and outside areas of the image are changed to background color. Secondly, the size of the air voids gets reduced and helps easier removal of the air voids and other noise from the image.

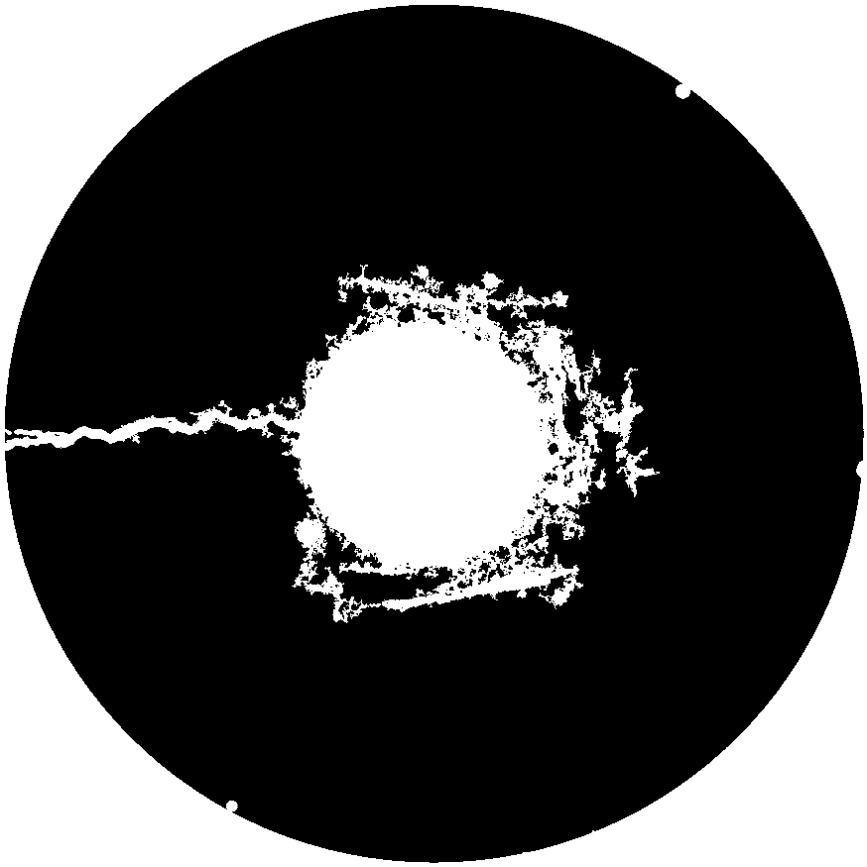

Figure 42 – Binarized image that was run though the DeleteSmallComponents function of mathematica to remove air voids and pores in the image accentuating the craked region and the damaged region connected to the middle hole.

Figure 42 shows a binarized image that was run though the DeleteSmallComponents function of mathematica to remove air voids and pores in the image accenuating the craked region and the damaged region connected to the middle hole. This function replaces small connected components in a binary image with background pixels. Figure 43 shows the resulting image which now shows only the area around the inner surface and the crack in the sample.

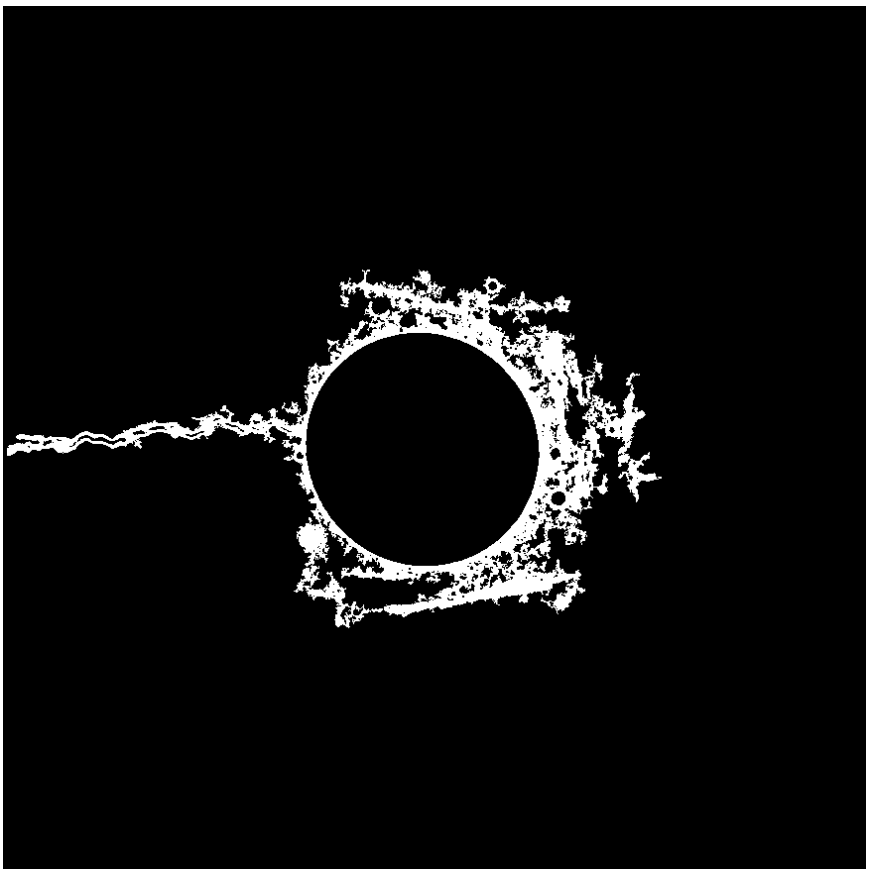

Figure 43 – Image corrected with the MorphologicalComponents and ReplacePixelValue functions as a part of the conversion routine to make the middle hole and the exterior of the cylindrical specimen the same as the background color. This removes a lot of unwanted data from the image to further accentuate the cracked regions and interconnected middel regions.

5.1.3 Image comparison

After pre-processing the image, the damaged regions before and after healing had to be compared. Two approached were attempted for that process. In the first method the entire 3d image of the specimen was reconstructed and then the difference between the number of voxels in the healed

and damaged specimens would be used as a metric to see if healing had occurred. In the second method individual image slices corresponding to each other in the damage and healed specimen set of images were compared.

- The pre-processed image's binary pixel value locations are stored in an array. Each image slice has its pixel values stored in a new row of the 3-dimensional array. This done by using a Mathematica routine. The array is then converted into a 3d image using Mathematica. Figure 44 – shows a specimen with a single slice image and a reconstructed 3d image.

- The pre-processed image set obtained the same sample before and after healing is run through a routine to see which slice of the pre-healed image set corresponds to equivalent slice of the healed image set. The ImageCorrespondingPoints function in Mathematica is used to achieve this. Each image from the pre- healed set is compared with the image set of the healed specimen. The partner images are selected and compared for determining is there is any visual difference between sample image slice before and after healing. The comparison is done with another Mathematica function ImageDifference.

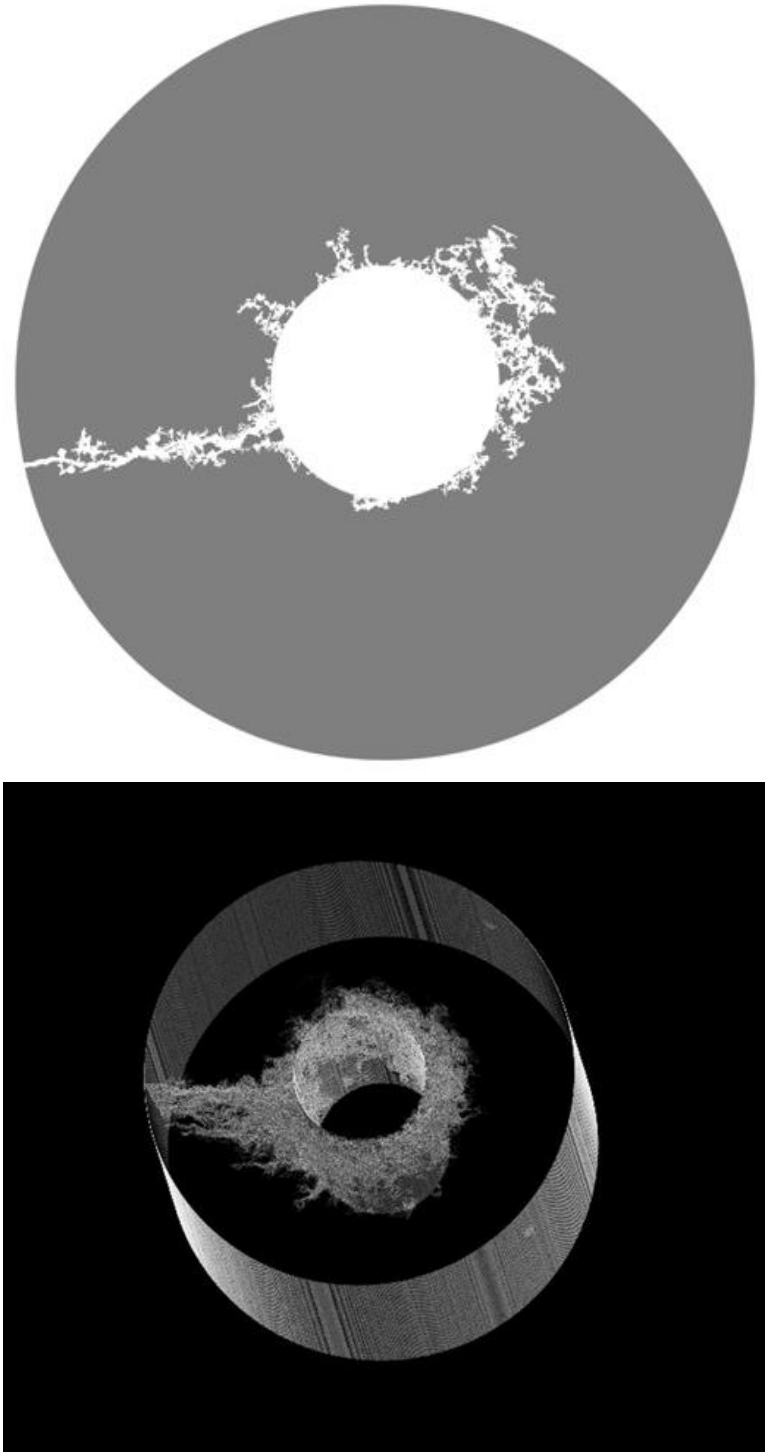

Figure 44 – A cross section slice (above) and 3d reconstructed image (below) of the cracked section obtained from X-ray CT imaging.

5.1.4 Results

Both the methods were very inconsistent in giving a clear answer to the question at hand. Based on where the initial threshold was set for the binarizing function the results varied significantly. The sensitivity to the threshold value on the Binarizing function was too high and there is no definite method to ascertain that the chosen value clearly represents what is observed in the actual image. Certain specimen scans showed that the damaged specimen has less crack pixels than the healed ones which is contrary to the observed experiments results. By changing the threshold value to a different graylevel this result could be reversed. Therefore, the validity of the technique could be considered questionable.

This was primarily a result of the limitations of the X-Ray CT method. The presence of the middle hole tends to create image artifacts like rings and blurriness around the inner surface of the specimen therefore image clarity varied significantly from one slice to another. However, qualitatively observing the X-Ray CT images all showed that there was no significant crack filling between the images taken before and after healing. This led us to believe the bulk of the precipitation of calcium carbonate was occurring at the inner surface of the cylinder.

5.2 SEM-EDS imaging and characterization

Due to the inconclusiveness of the X-ray CT scans and the hypothesis that precipitation might only have occurred in the inner surface and close to the crack mouth opening on the inner surface of the cylinder. SEM EDS was considered as an option to characterize the actual deposition on the surface

of the cylinder. SEM is a tyEnerpe of electron microscope that images surfaces of a target sample by using focused beam of electrons. The electrons interact with the atoms in the sample and produces a signal which is used to image the sample. SEM can achieve better than 1nm resolution. SEM-EDS is a technique used to measure the elemental composition of a material. High energy charged particles like electrons are focused on the sample. The electrons in the target are excited to higher energy level creating a hole where the electron was originally located. A higher energy electron fills this hole and the difference in energy between the electron shell levels is released in the form of an X-ray. The energy and number of X-rays emitted can be measured with an Energy Dispersive Spectrometer. The X-rays are characteristic of the atomic structure of the element that releases it and is used in determining the elemental composition of the material.

5.2.1 Sample preparation

The SEM used for the EDS analysis was a Field Emission Scanning Electron Microscope (FE-SEM). The healed samples were broken apart at the crack and cut into smaller pieces for the SEM imaging. These pieces were the oven dried at 100 degrees Celsius for 24 hours. This process was essential to remove any residual humidity within the pore network of the cement mortar samples. First look at the inner surface of the healed cylinder under the SEM showed crystalline deposits that were uncharacteristic of cement mortar. The specimen used here is the one healed with the supersaturated healing solution.

EDS analysis was performed on the control, saturated and supersaturated specimens. The precipitate deposited by the healing solutions was calcium carbonate. However, calcium and

oxygen are present abundantly in products of hydration. carbon is also present due to the natural carbonation of cement mortar and abundantly present in nature. Therefore, another way of determining if calcium carbonate (calcite) is truly present is needed. For this purpose, EDS analysis of the surface of a control specimen that wasn't treated with healing solutions and a specimen treated with Solution 4 (super saturated with Ca^{2+} ions) were done to compare the elemental distribution and composition of the two surfaces. Figure 45 and Figure 47 shows the elemental makeup of the surfaces of the surfaces of specimen treated with no healing solution and the specimen treated with Solution 4 (super saturated with Ca^{2+} ions). The detection of silicon is the critical in determining the presence of calcium carbonate. On surfaces that have very good precipitation of clacite the silicon count will be close to zero. On surfaces with partial coating silicon count will be significantly lower than surfaces with no precipitation. This technique was used as the basis for determining where the healing solutions precipitated the calcium carbonate on the cylindrical pipe section specimens.

5.2.2 EDS analysis and discussion

For the reduction in permeability precipitation of the calcite crystals had to have occurred on the inner surface or the cracked surface of the hollow cylindrical pipe section specimens. For the purposes of the study specimens having the cracked and inner surfaces were analyzed using the SEM-EDS method. For the inner surface a control specimen that wasn't treated with healing solution was used as the base then specimens treated with the Control Solution, Solution 3 and Solution 4 were analyzed. Based on the results of the inner surface analysis for the cracked surface

analysis one specimen treated with no healing water and 3 specimens treated with Solution 4 were analyzed and the results were compiled.

5.2.2.1 Specimen 1 – Inner cylindrical surface (No healing treatment)

The control specimen that wasn't treated with any solution was analyzed first to get a base line for the distribution of elements in cement mortar. Figure 45 shows the SEM image and the EDS analysis of the specimen section. The SEM image shows the surface of the mortar specimen used to do the EDS analysis. The distribution of the elemental composition on the surface obtained from the EDS analysis is shown in Table 9

Table 9 – Weight percentage distribution of the elemental composition of the inner surface of Specimen 1.

Element	**Weight %**
Carbon	7.67
Oxygen	63.15
Magnesium	0.29
Aluminum	1.21
Silicon	3.97
Sulfur	0.64
Calcium	22.44
Iron	0.63

Since this analysis was performed on a specimen with no interaction with the healing solutions, the result of the analysis of this specimen will be used as the baseline to compare other EDS analyses performed on the specimens treated with the healing solutions.

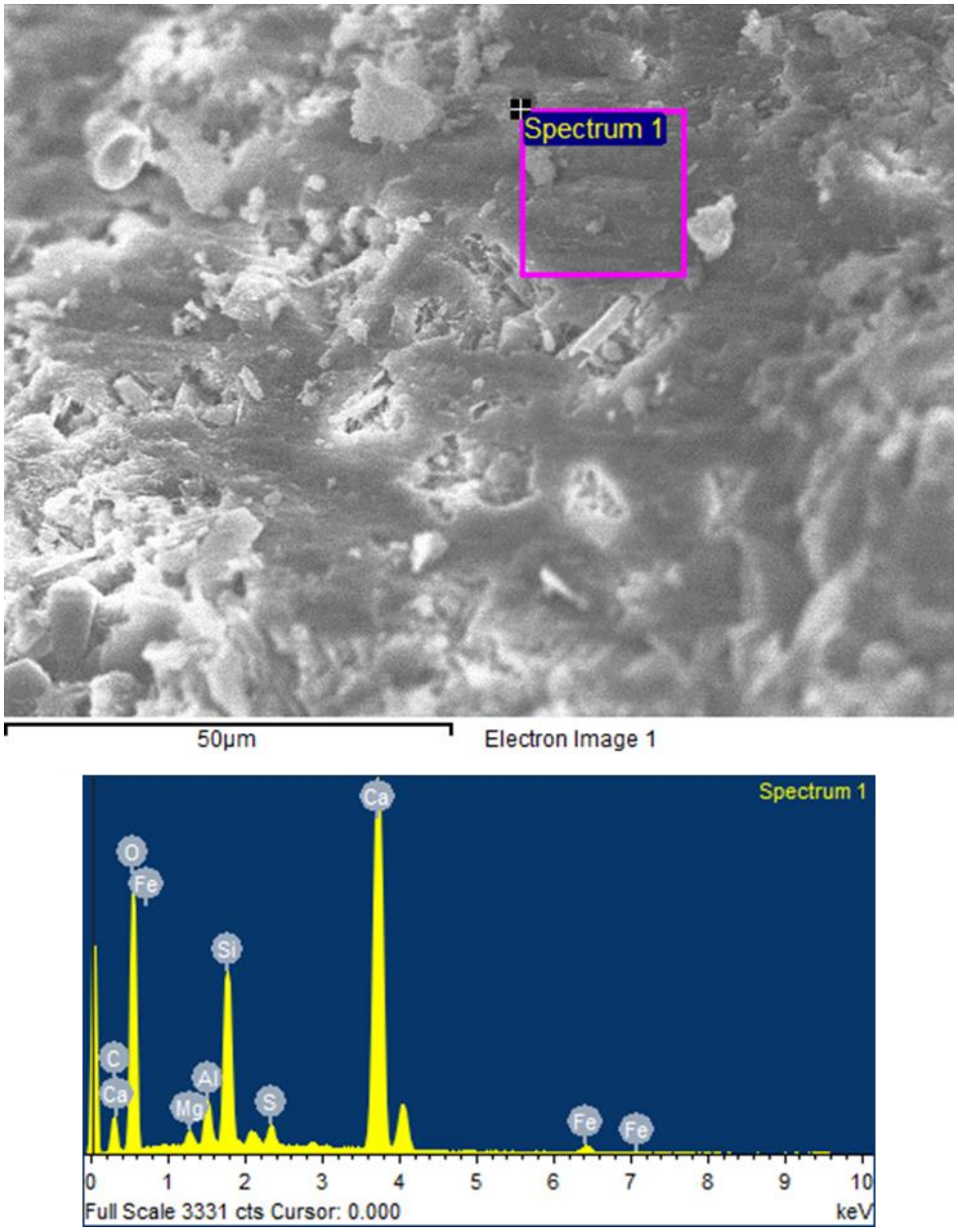

Figure 45 – SEM image and EDS analysis spectrum of the inner surface of a mortar sample that was not treated with any healing solution. The EDS spectrum shows that the analyzed surface is comprised of Carbon, Oxygen, Calcium, Silicon, Magnesium, Iron, Sulfur, and Aluminum.

5.2.2.2 Specimen 2 – Inner cylindrical surface (treated with the Control Solution)

The specimen that was treated with the Control Solution used as a baseline for the healing tests. This specimen was chosen for analysis using EDS to see if there is any difference seen by just the treatment with the control solution. Figure 46 shows the SEM image and the EDS analysis of the specimen section. The SEM image shows the surface of the mortar specimen used to do the EDS analysis. The distribution of the elemental composition on the surface obtained from the EDS analysis is shown in Table 10

Table 10 – Weight percentage distribution of the elemental composition of the inner surface of Specimen 2.

Element	**Weight %**
Carbon	8.31
Oxygen	59.35
Magnesium	0.71
Aluminum	1.56
Silicon	6.86
Sulfur	0.95
Calcium	21.26
Iron	1.01

The result of this analysis shows that Specimen 1's elemental composition is very similar to that of the control specimen. Therefore, from the result we can infer that there is no deposition of any additional chemicals on the surface of the specimen.

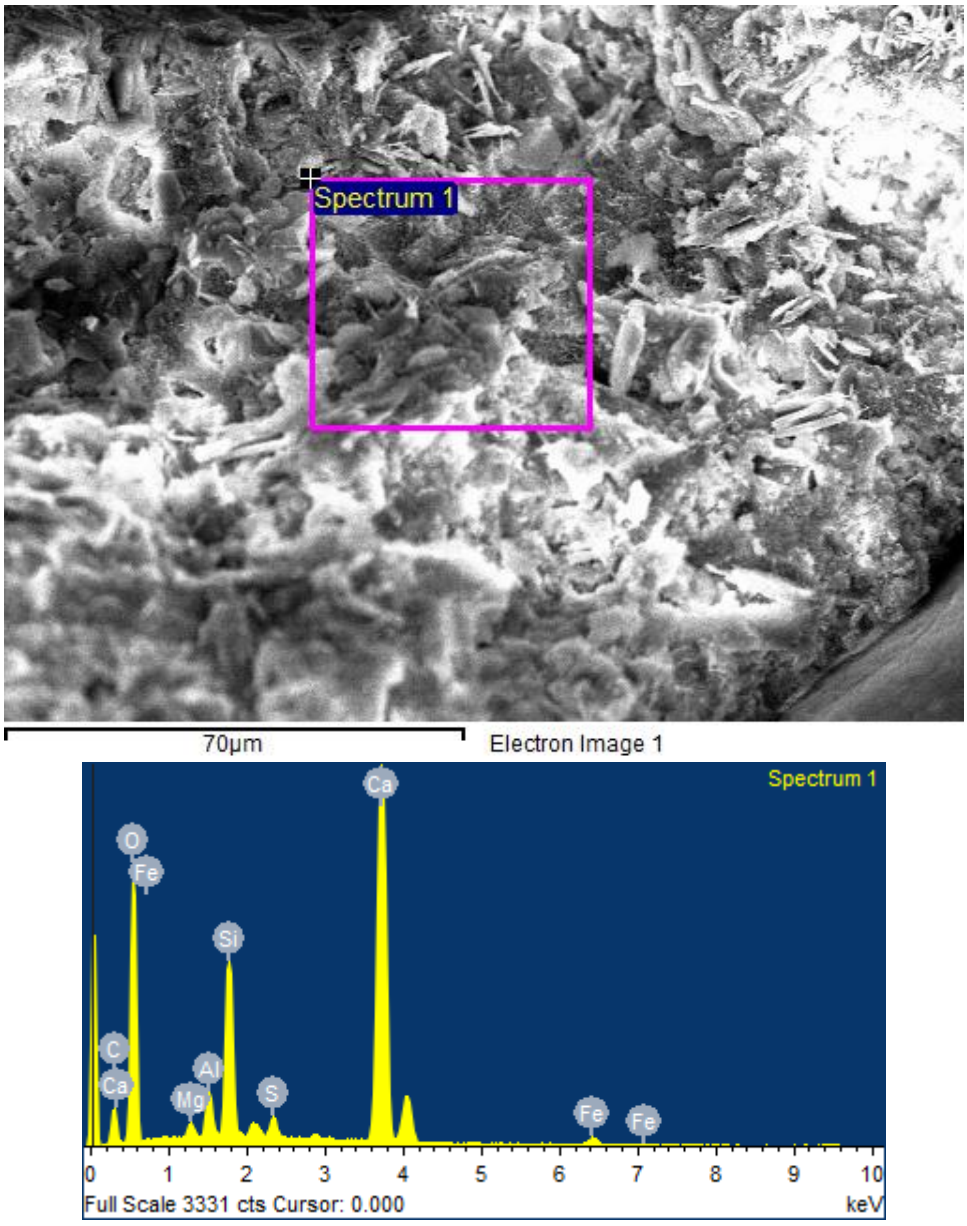

Figure 46 – SEM image and EDS analysis spectrum of the surface of a mortar sample that was treated with control solution used for healing. The EDS spectrum shows that the analyzed surface is comprised of Carbon, Oxygen, Calcium, Silicon, Magnesium, Iron, Sulfur, and Aluminum.

5.2.2.3 Specimen 3 – Inner cylindrical surface (treated with Solution 3)

The specimen treated with Solution 4 (highly super saturated) was analyzed next. Figure 47 shows the SEM image of the surface analyzed with its frequency spectrum. From the spectrum it is observed that the composition is the surface is made up of calcium oxygen and carbon only. The surface is coated with the precipitate from the healing solution. The elemental composition is explained in detail in Table 11

Table 11 – Weight percentage distribution of the elemental composition of the inner surface of Specimen 3.

Element	**Weight %**
Carbon	13.28
Oxygen	56.27
Silicon	0.12
Calcium	30.33

From the elemental composition of the analysis we can see that that there are only 4 elements that are observed on the surface. The predominant presence of only calcium, oxygen and carbon coupled with the absence of the other elements present on the surface of the Specimen 1 and 2 shows that there is layer of coating of on the surface of the mortar. This is from the calcite crystals precipitated on the surface from calcium carbonate in the healing solution. There is a negligible amount of silicon also detected from the surface.

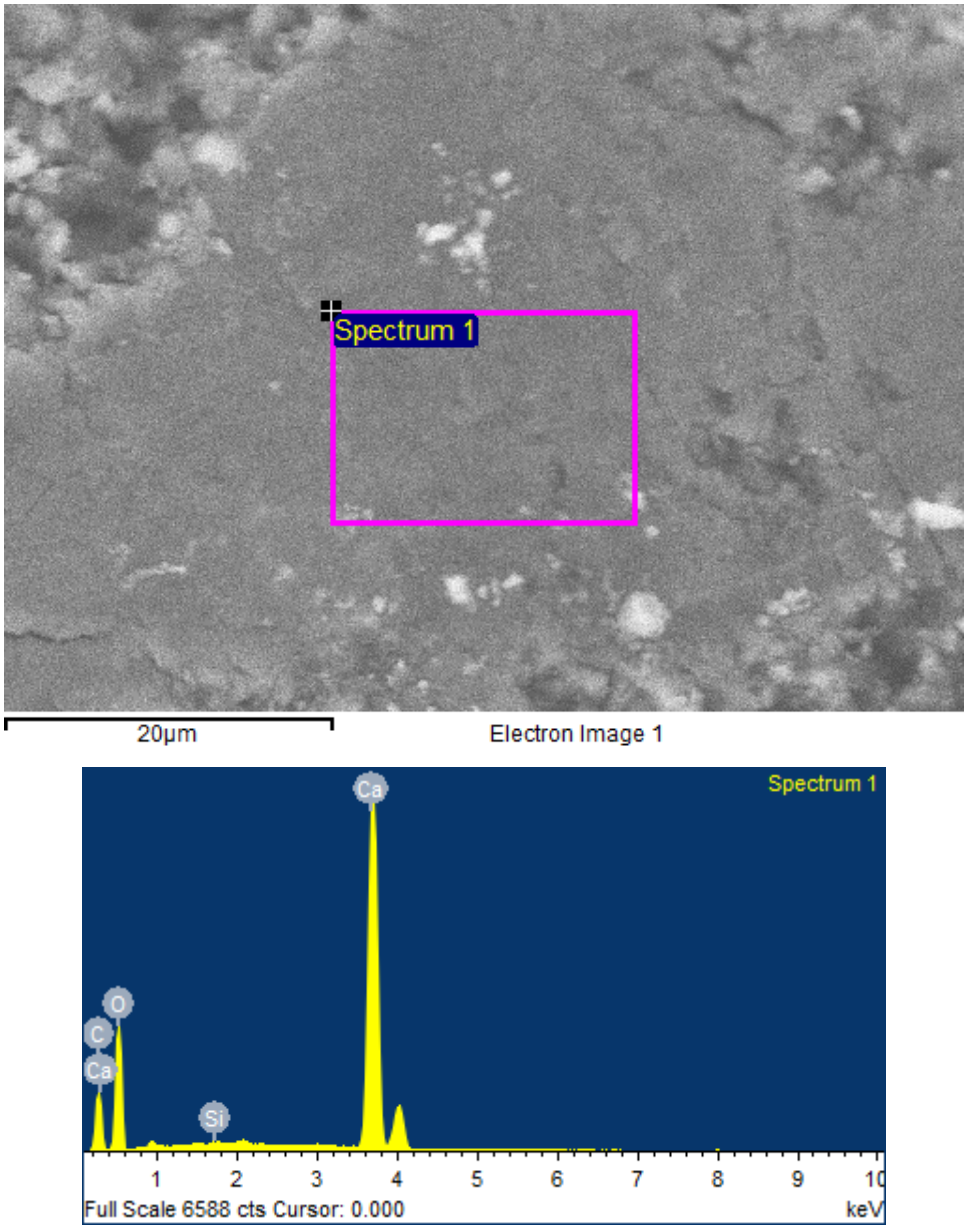

Figure 47 – SEM image and EDS analysis spectrum of the surface of a mortar sample that was treated with Solution 3 used for healing. The EDS spectrum shows that the analyzed surface is comprised of Carbon, Oxygen, and Calcium.

5.2.2.4 Specimen 4 – Inner cylindrical surface (treated with Solution 4)

The specimen treated with Solution 4 (slightly supersaturated solution) was analyzed next. Figure 48 shows the SEM image of the surface analyzed with its frequency spectrum. From the spectrum it is observed that the composition is the surface is made up of calcium oxygen and carbon. Table 12 details the elemental composition of the surface.

Table 12 – Weight percentage distribution of the elemental composition of the inner surface of Specimen 4.

Element	**Weight %**
Carbon	12.64
Oxygen	59.04
Calcium	28.32

From the elemental composition of the analysis we can see that that there are only 3 elements that are observed on the surface. The result is similar to Specimen 3 thus, it can be inferred that there is layer of precipitate coating over the mortar surface and that masks the other elements found on the surface. This is from the calcite crystals precipitated on the surface from calcium carbonate in the healing solution.

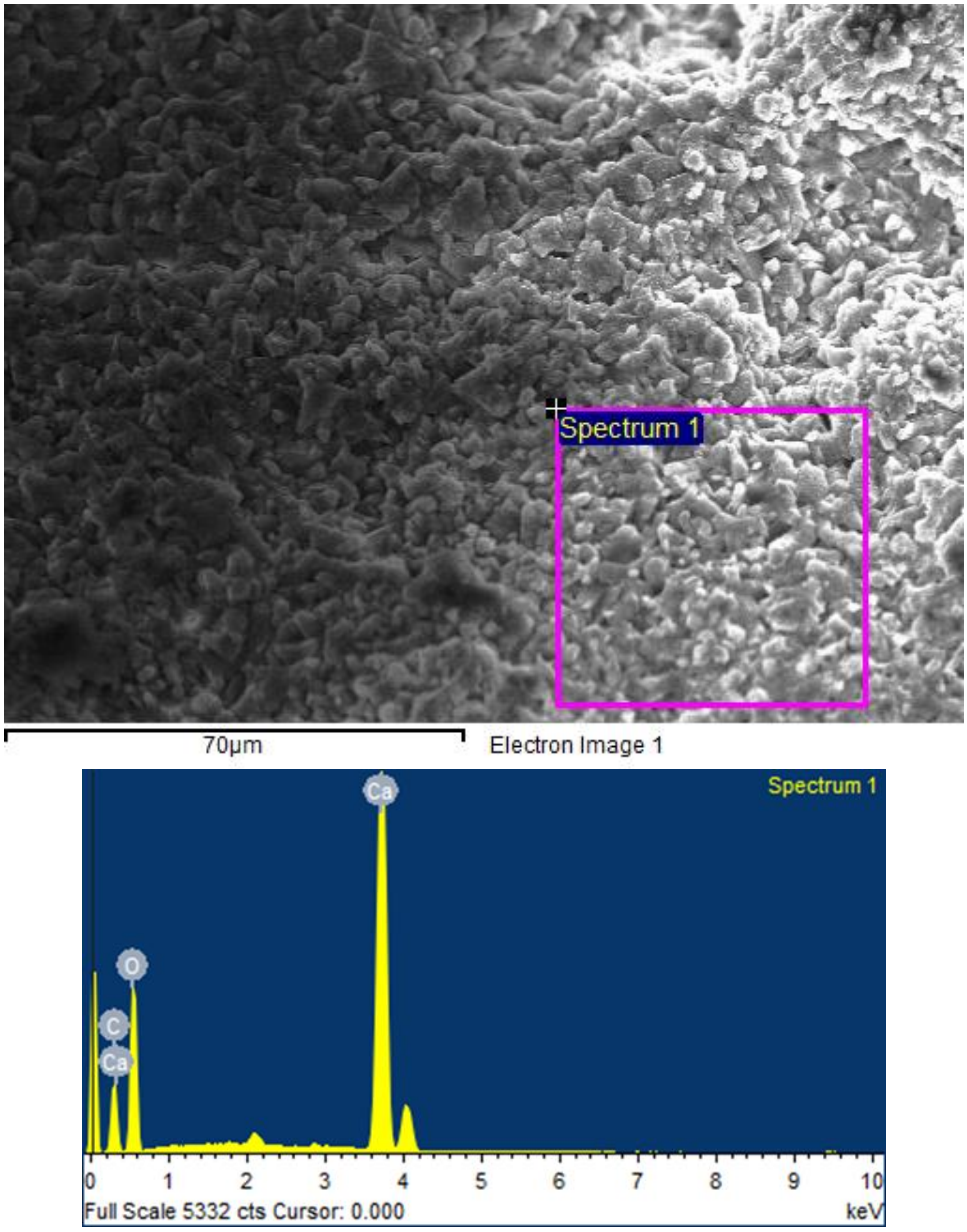

Figure 48 – SEM image and EDS analysis spectrum of the surface of a mortar sample that was treated with Solution 4 used for healing. The EDS spectrum shows that the analyzed surface is comprised of Carbon, Oxygen, Silicon, and Calcium.

5.2.2.5 Specimen 5 - Crack surface (No healing treatment).

Specimens 3 and 4 confirmed that the deposition of calcium carbonate occurs on the inner surface of the hollow cylindrical pipe section specimen. It is also important to see if there is a similar amount of deposition in the cracked surfaces of the specimens. Specimen 4 consisted of a cracked surface that had been treated with the control solution. Figure 49 shows the SEM image and the EDS analysis of the specimen section. The SEM image shows the surface of the mortar specimen used to do the EDS analysis. Table 13 details the elemental composition of the surface.

Table 13 – Weight percentage distribution of the elemental composition of the crack surface of Specimen 5.

Element	**Weight %**
Carbon	8.20
Oxygen	55.80
Magnesium	0.78
Aluminum	2.18
Silicon	6.10
Sulfur	1.65
Calcium	21.23
Iron	2.10

From the elemental composition that was determined from the surface EDS analysis it is seen that the surface is essentially similar to the Specimens 1 and 2 distributions and no deposition is observed on the surface. This specimen will be treated as the control comparison for all the cracked surface analysis.

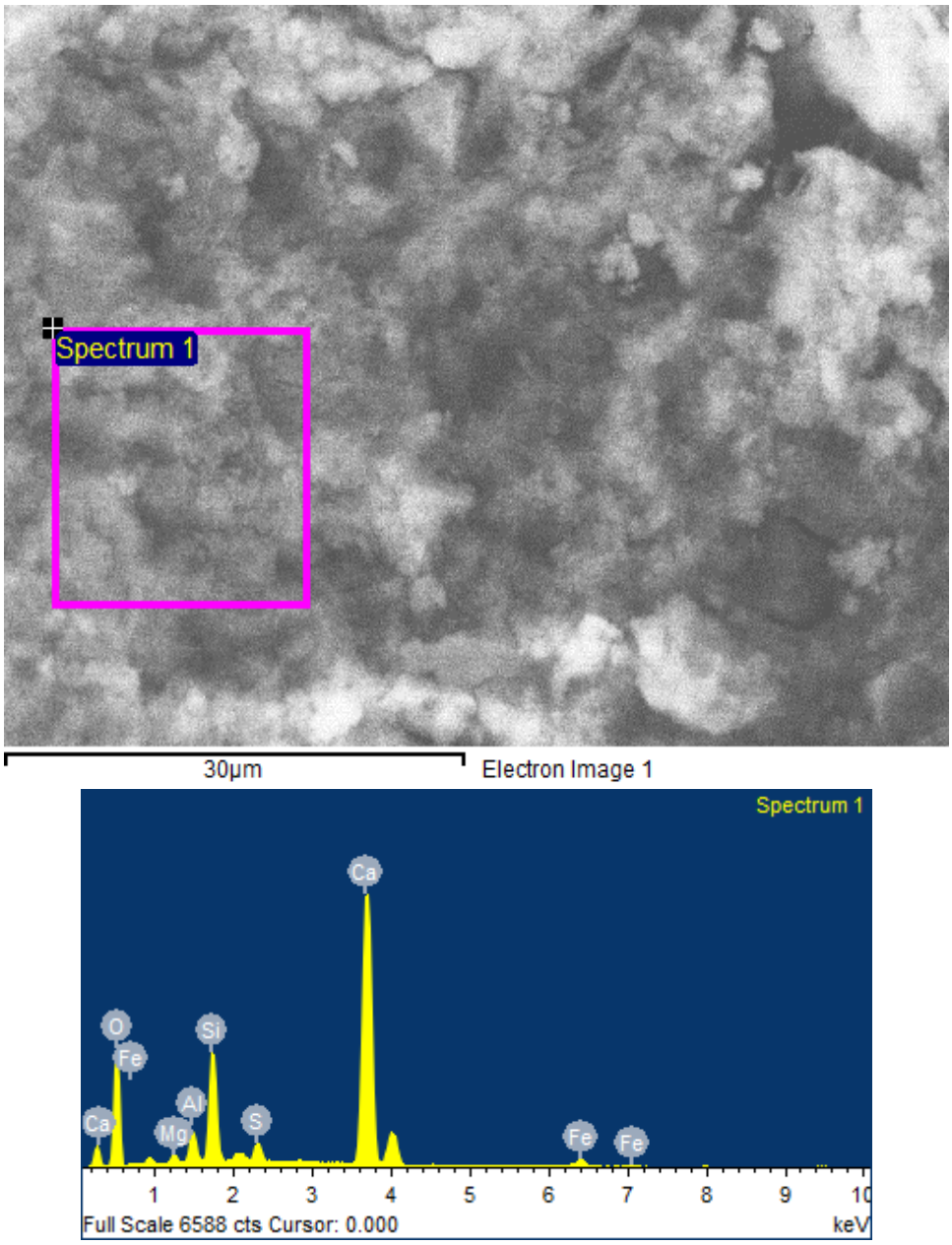

Figure 49 – SEM image and EDS analysis spectrum of the cracked surface of a mortar sample that was treated with control solution used for healing. The EDS spectrum shows that the analyzed surface is comprised of Carbon, Oxygen, Calcium, Silicon, Magnesium, Iron, Sulfur, and Aluminum.

5.2.2.6 Specimen 6 - Crack surface treated with Solution 4.

The crack surface of specimens treated with the healing solution was observed and analyzed next to see if any deposition is observed on the cracked surfaces. Figure 50 shows the SEM image and the EDS analysis of the specimen section. The SEM image shows the surface of the mortar specimen used to do the EDS analysis. Table 14 details the elemental composition of the surface.

Table 14 – Weight percentage distribution of the elemental composition of the crack surface of Specimen 6.

Element	**Weight %**
Oxygen	65.58
Magnesium	0.23
Aluminum	0.54
Silicon	27.38
Sulfur	0.2
Calcium	5.80
Iron	0.27

From the elemental composition that was determined from the EDS analysis it is seen that almost all the elements that were present in specimen 5 are present in specimen 6. Carbon is not detected and there is also a significantly higher silicon concentration in this region compared to the control specimen.

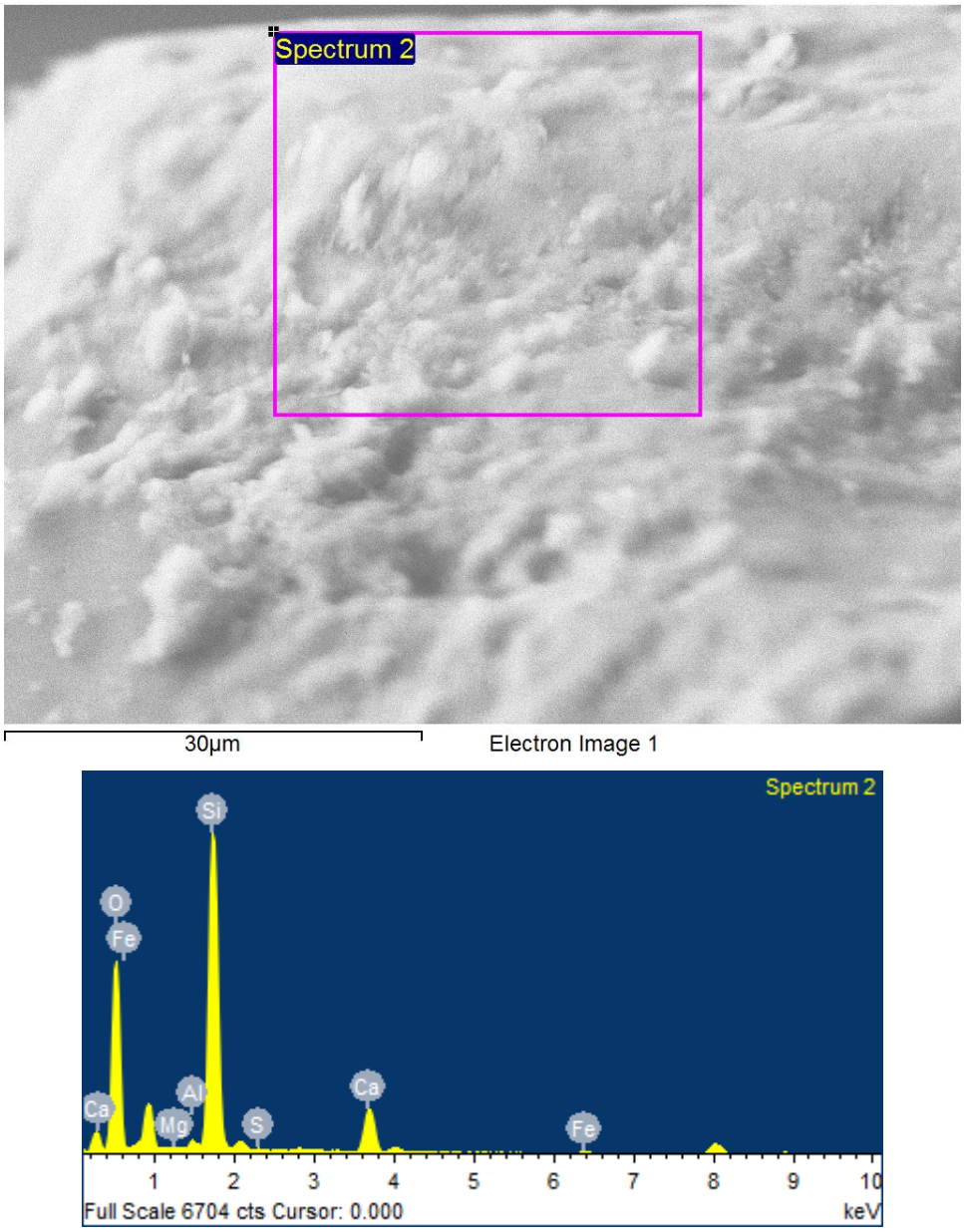

Figure 50 – SEM image and EDS analysis spectrum of the cracked surface of a mortar sample that was treated with Solution 4 used for healing. The EDS spectrum shows that the analyzed surface is comprised of Oxygen, Calcium, Silicon, Magnesium, Iron, Sulfur, and Aluminum.

5.2.2.7 Specimen 7 - Crack surface treated with Solution 4.

Specimen 6 was the second specimen of a cracked surface treated by healing solution 4 observed under SEM and analyzed with EDS. Figure 51 shows the SEM image and the EDS analysis of the specimen section. The SEM image shows the surface of the mortar specimen used to do the EDS analysis. Table 15 details the elemental composition of the surface.

Table 15 – Weight percentage distribution of the elemental composition of the crack surface of Specimen 7.

Element	**Weight %**
Carbon	18.12
Oxygen	55.83
Magnesium	0.23
Aluminum	0.21
Silicon	3.39
Sulfur	0.12
Potassium	0.27
Calcium	22.06

The elemental composition of specimen 6 is similar to that of specimens 5 and 6. As far as weight percentage is concerned the distribution is similar to the specimen 5. Higher carbon content could mean localized deposition of calcite crystals.

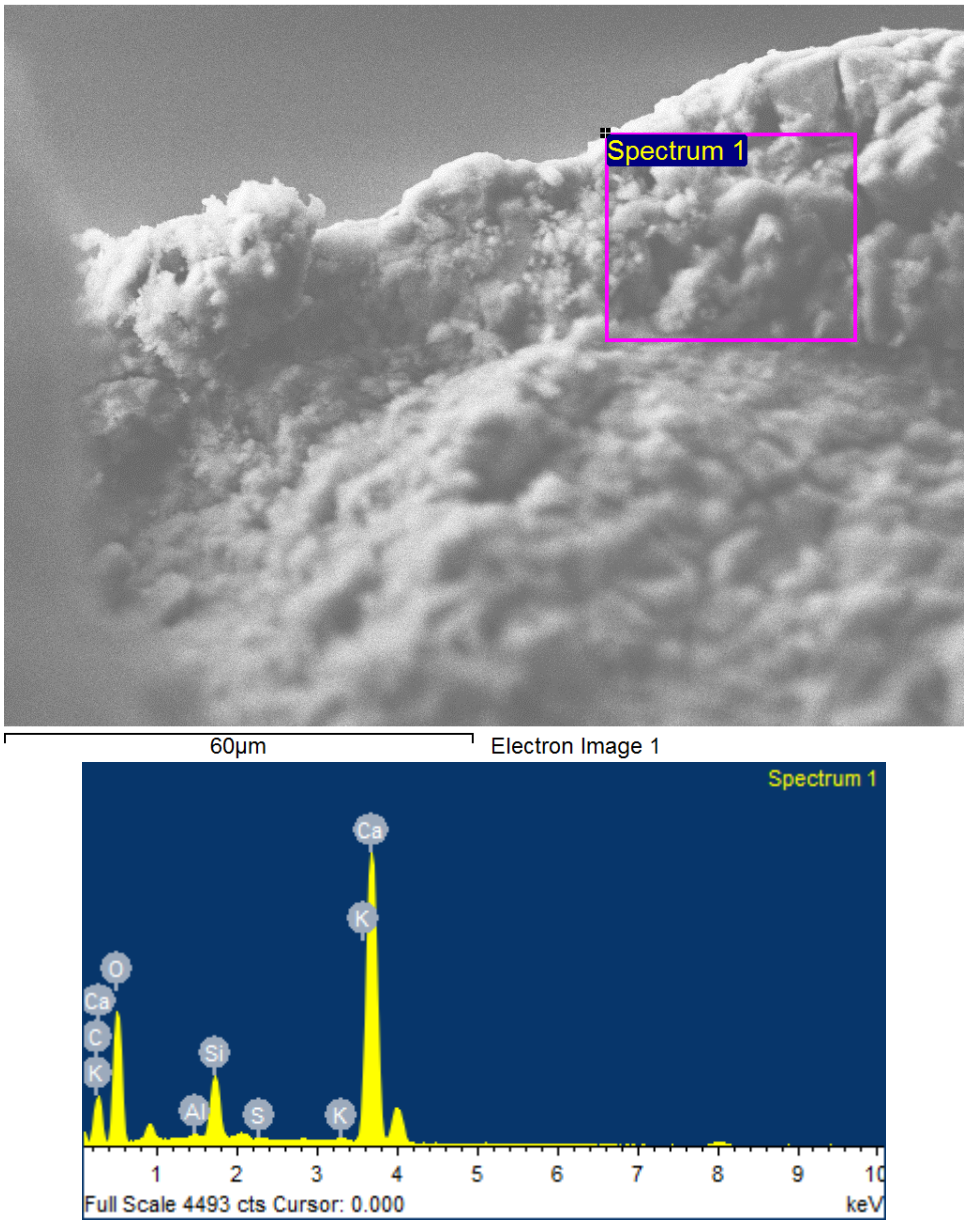

Figure 51 – SEM image and EDS analysis spectrum of the cracked surface of a mortar sample that was treated with Solution 4 used for healing. The EDS spectrum shows that the analyzed surface is comprised of Oxygen, Calcium, Silicon, Magnesium, Iron, Sulfur, and Aluminum.

5.2.2.8 Specimen 8 - Crack surface treated with Solution 4.

Specimen 7 was the second specimen of a cracked surface treated by healing solution 4 observed under SEM and analyzed with EDS. Figure 52 shows the SEM image and the EDS analysis of the specimen section. The SEM image shows the surface of the mortar specimen used to do the EDS analysis. Table 16 details the elemental composition of the surface.

Table 16 – Weight percentage distribution of the elemental composition of the crack surface of Specimen 8.

Element	**Weight %**
Carbon	9.15
Oxygen	58.83
Magnesium	0.62
Aluminum	2.05
Silicon	7.81
Sulfur	0.97
Iron	1.72
Calcium	18.86

The analysis results show similarity to the specimens 4, 5 and 6 in elemental composition. The distribution is also very close to specimens 4 and 6. This result is much closer to the control cracked specimen than the other 2 specimens. Thus, it can be inferred that there was no deposition of calcium carbonate observed in this region of the specimen.

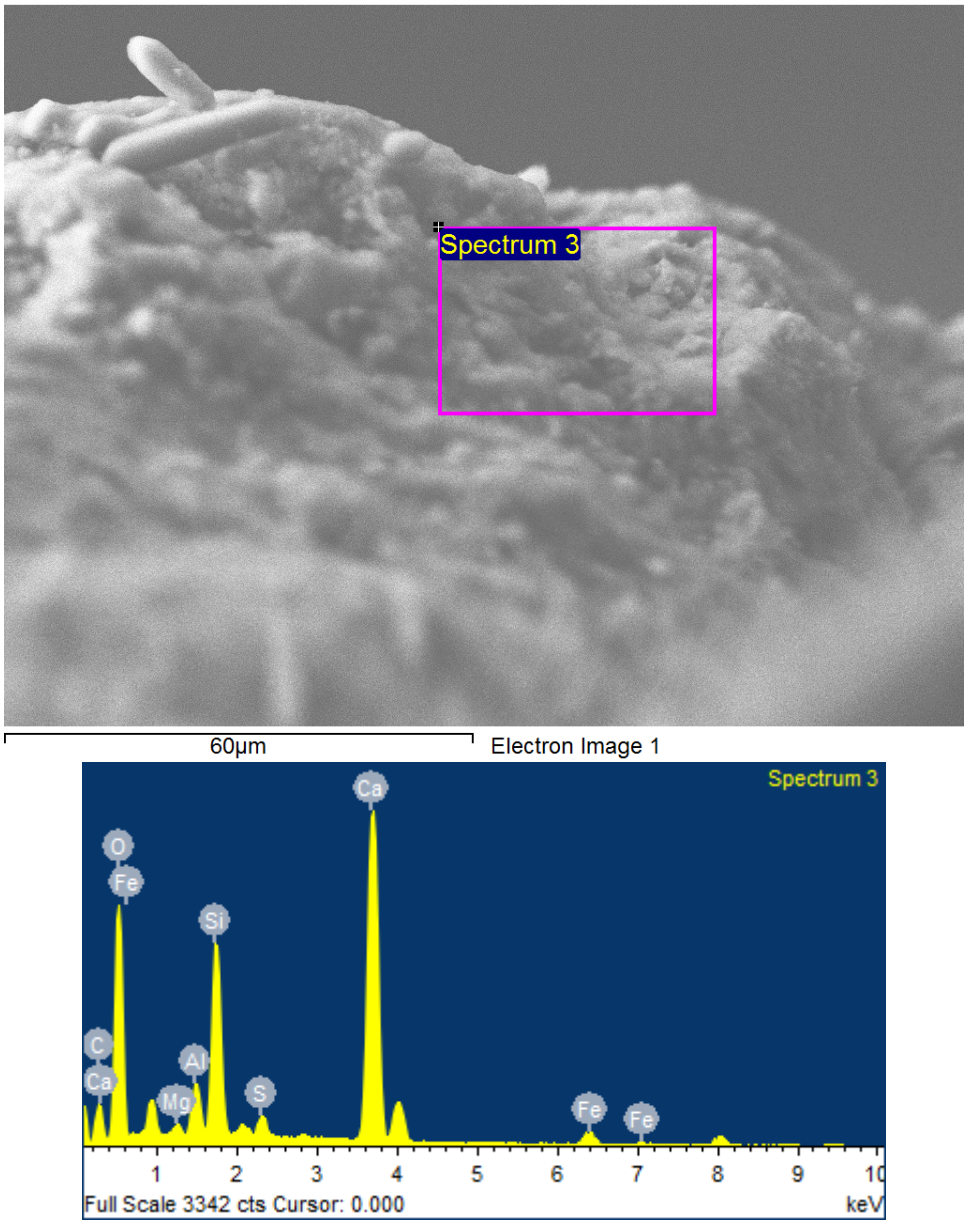

Figure 52 – SEM image and EDS analysis spectrum of the cracked surface of a mortar sample that was treated with Solution 4 used for healing. The EDS spectrum shows that the analyzed surface is comprised of Oxygen, Calcium, Silicon, Magnesium, Iron, Sulfur, and Aluminum.

5.2.3 Results

Figure 53 shows a bar chart that compares the elemental distribution between Specimen 1 and Specimen 2. From Figure 53 it can be observed that the Specimen 1 which was not treated with any shows almost identical results to a specimen which had healing treatment done with the Control Solution (no healing salts added). Specimens 1 and 2 were expected to have no precipitation of calcite on its surfaces and the EDS results agree with the expected result.

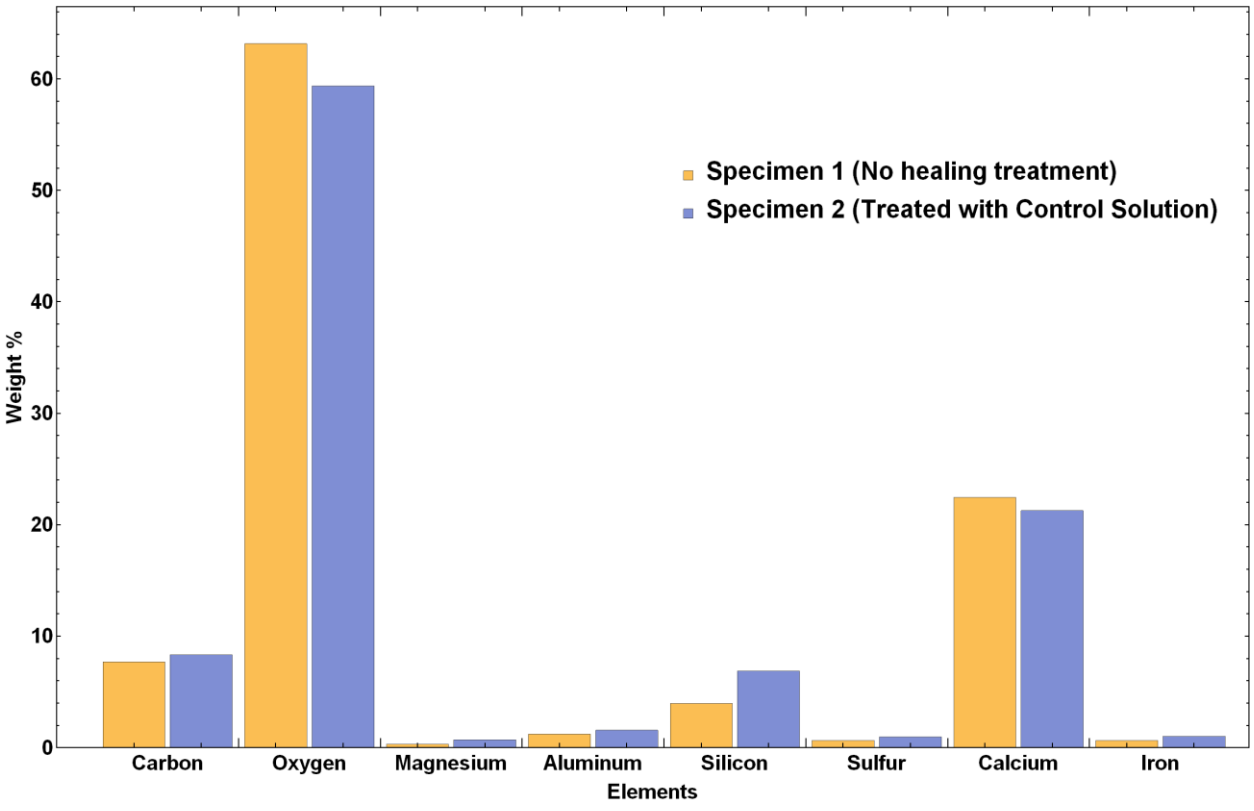

Figure 53 – Comparison of the elemental composition distribution obtained from SEM-EDS analysis performed on Specimen 1 and Specimen 2. The elemental distribution is essentially the same which was the expected result on the two surfaces without any calcite precipitation.

Figure 54 shows the comparison of SEM - EDS elemental composition analysis results for Specimen 3 and Specimen 4. These specimens as were treated with Solution 3 and Solution 4 respectively. We can observe that the elements that are dominantly present on these surfaces are calcium, carbon, and oxygen. This is a result of the precipitation of the calcium carbonate from the healing solutions as calcite crystals on the surface. However, there is a small difference between the elemental composition and distribution observed between the two surfaces. The surface treated with solution 4 only contains calcium, carbon and oxygen which are the elements present in calcium carbonate. The surface treated with solution 3 has additional trace amounts of silicon present on the surface. Less than 1% compared by weight. There are two possible explanations to this occurrence.

Solution 4 has more deposition compared to Solution 3 as evidenced by the permeability change measurements from both the decalcified and cracked specimens. With more deposition the surface of concrete was completely covered to a depth higher than that of what the X-rays of EDS can penetrate through. However, on specimen 3 either the deposition layer thickness was low enough to allow some silicon atoms also to be reached by the X-rays of the EDS equipment. The second reason for this could be that there was an aggregate protrusion on the surface that was scanned. Aggregates are primarily made up of silicon and oxygen and hence the presence of silicon in the analysis. However, the thickness of coating is the more logical solution in this scenario as it is in accordance with the permeability results of the healed hollow cylindrical specimens by the two solutions used in the healing process.

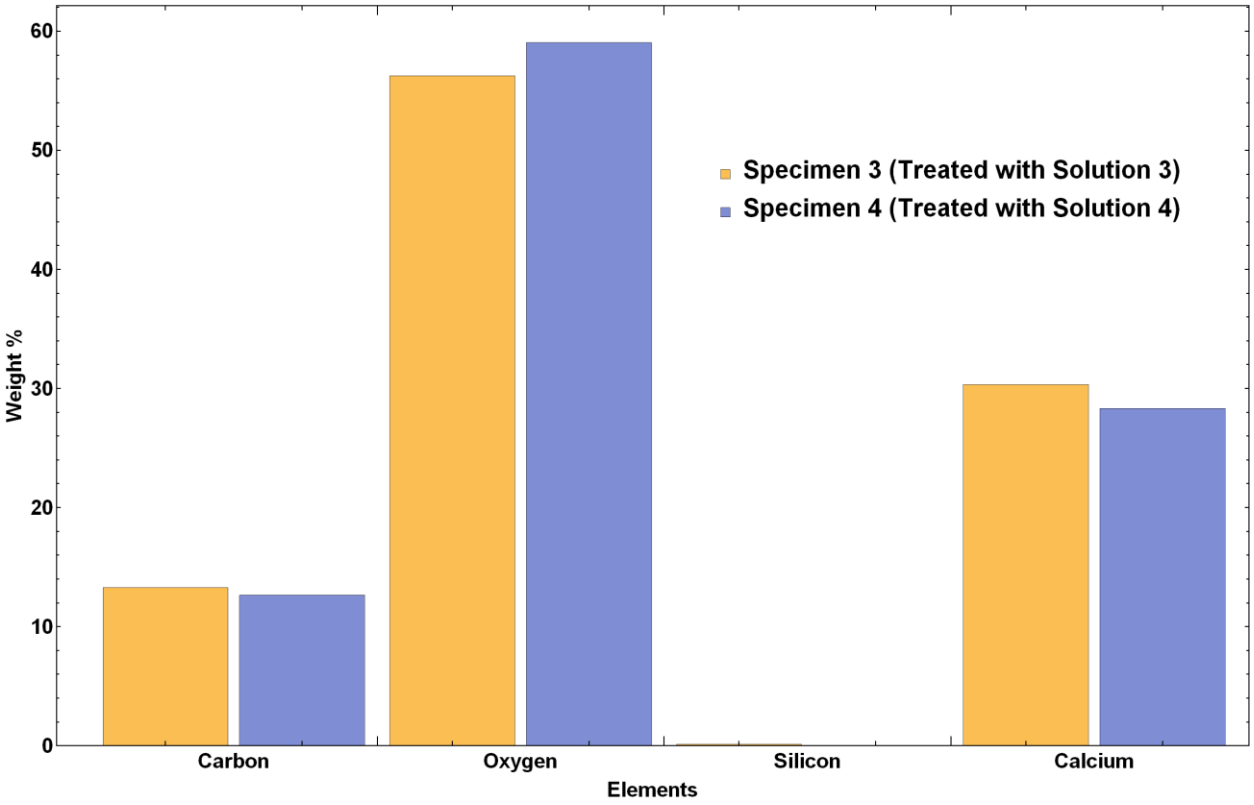

Figure 54 – Comparison of results of SEM - EDS elemental composition of inner surface of the hollow cylindrical specimen treated with Solution 3 (Specimen 3) and a specimen treated with Solution 4 (Specimen 4). Results that both surfaces are coated with calcium carbonate with Specimen 3 possibly having lower coating thickness.

Figure 55 shows comparison of SEM - EDS elemental composition analysis results for Specimen 5 and Specimen 6. The results show that the elemental composition of these two specimen surfaces are the same. However, weight percentage distribution of elements on Specimen 5 is completely different from that on Specimen 4. The surface of Specimen 5 seems to be devoid of carbon and there is also a significant increase in the weight percentage of silicon on it. The explanation for this result would be that Specimen 5 is comprised of a significant number of exposed aggregates.

Aggregates typically don't have carbon and are primarily comprised of silicon and oxygen in case of river sand or calcium and oxygen in case of limestone aggregates. The absence of carbon and the significantly higher presence of silicon on the surface shows that there is no coating layer of precipitated calcite crystals from the healing solution.

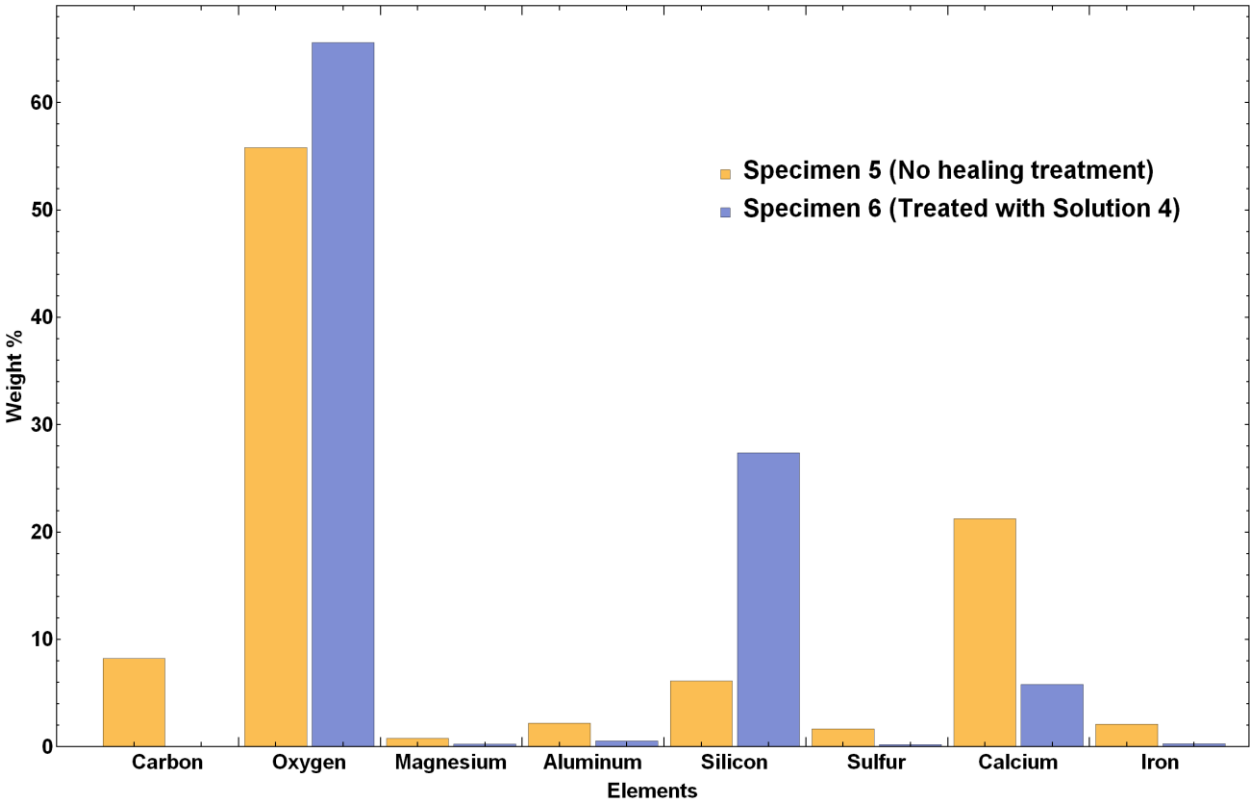

Figure 55 – Comparison of results of SEM - EDS elemental composition of cracked surface of the hollow cylindrical specimen treated with no healing treatment (Specimen 3) and a specimen treated with Solution 4 (Specimen 5). Results show no coating on the surface.

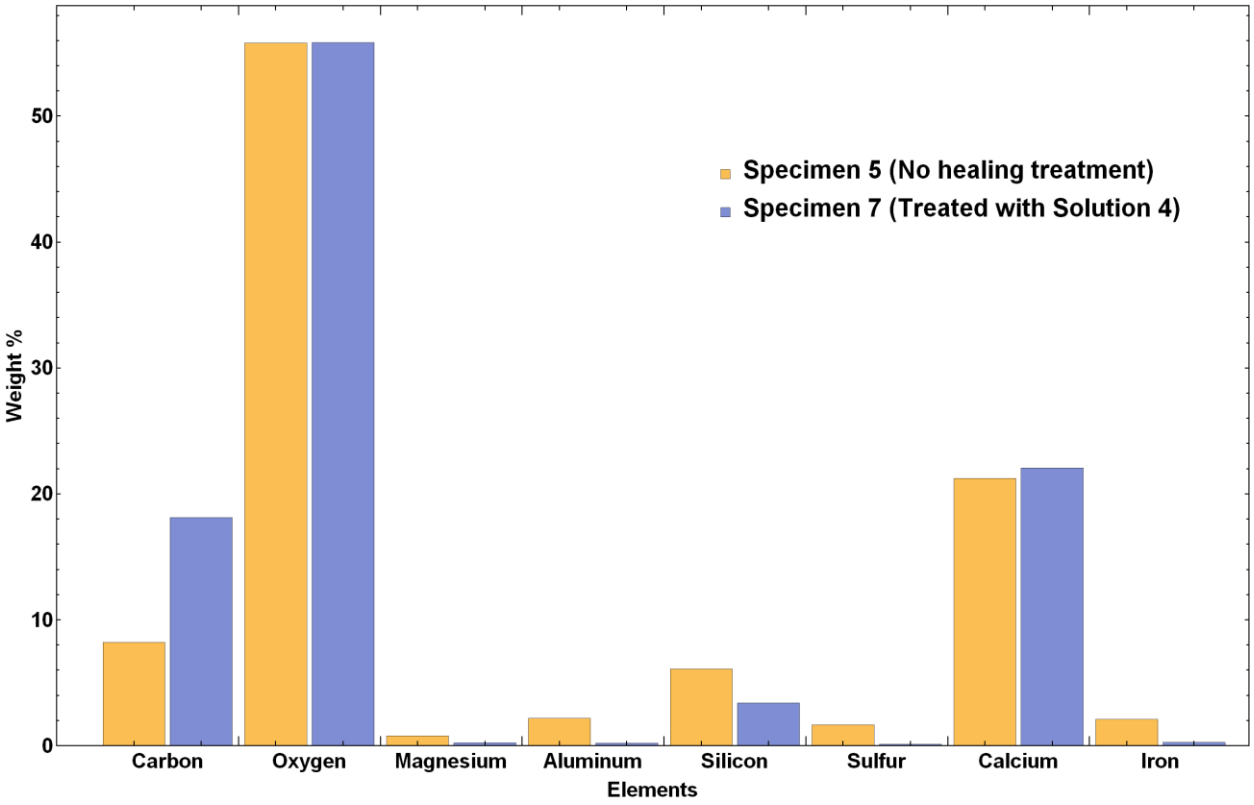

Figure 56 – Comparison of results of SEM -EDS elemental composition of cracked surface of the hollow cylindrical specimen treated with no healing treatment (Specimen 3) and a specimen treated with Solution 4 (Specimen 5). Results show no coating on the surface.

Figure 56 shows comparison of SEM - EDS elemental composition analysis results for Specimen 5 and Specimen 7. The results show that the elemental composition of these two specimen surfaces are the same. There is no significant abnormality in the weight percentage distribution comparison between the two specimens as with the comparison between Specimens 5 and 6. However, the carbon content of Specimen 6 is higher than the control specimen (Specimen 5). Also, the elements like silicon, magnesium, aluminum, sulfur, and iron have a lower weight percentage compared to the control specimen. The difference could be attributed to presence of some calcite crystals on

the surface masking the other elements but not completely coating the surface to dominate the elemental distribution as with Specimens 3 and 4. It is highly likely that there was sporadic precipitation of the calcite crystals from the healing solution on this surface when the healing solution passed through the cracked region, but the flow wasn't enough to coat the entire surface

.

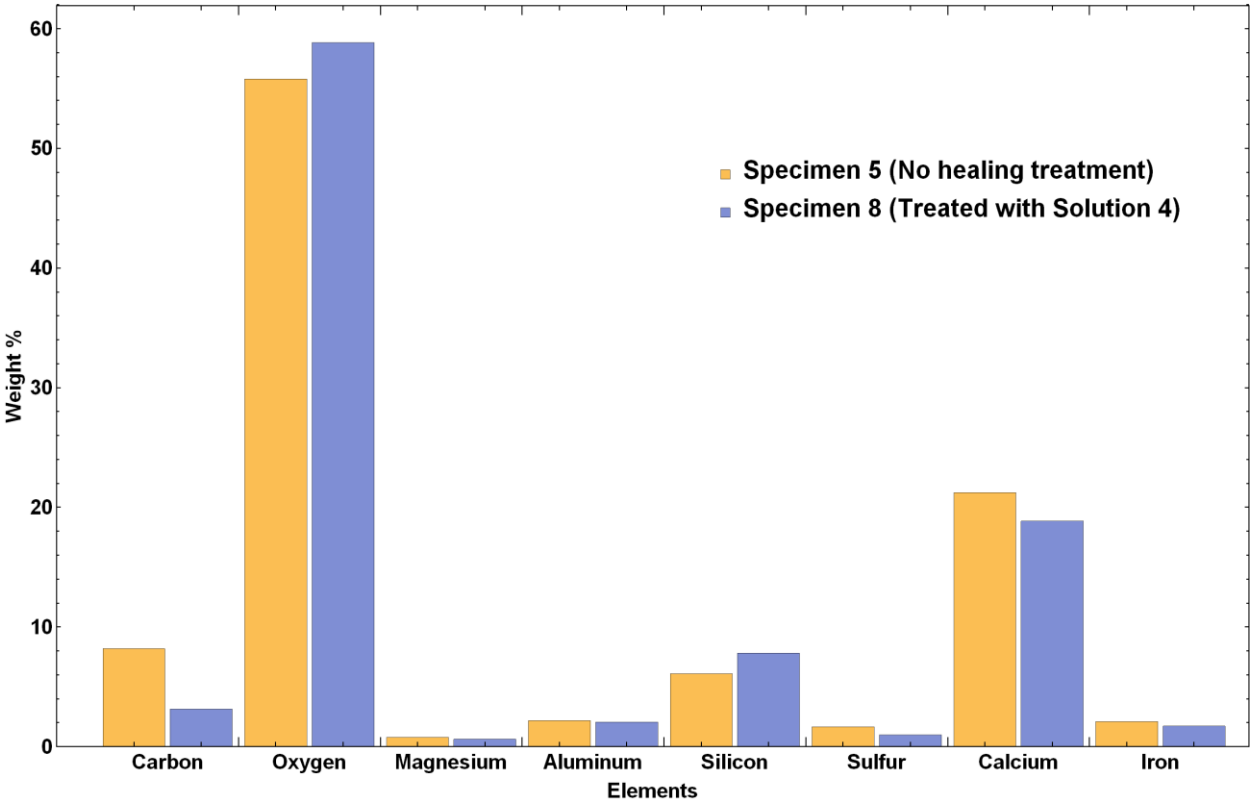

Figure 57 – Comparison of results of EDS elemental composition of cracked surface of the hollow cylindrical specimen treated with no healing treatment (Specimen 3) and a specimen treated with Solution 4 (Specimen 5). Results show no coating on the surface.

Figure 57 shows comparison of SEM - EDS elemental composition analysis results for Specimen 5 and Specimen 8. The results show that the elemental composition of these two specimen surfaces are the same. The weight percentage distribution is also comparably the same between the two specimens. There is no coating of calcite on the surface of Specimen 8.

5.3 Conclusion

The results obtained from the X-ray CT analysis show that there is no visible change between the cracked sample and healed sample from visual observation of the images obtained from tomographic reconstruction of the images. The resolution of the images obtained from the reconstruction is low enough that the thickness of the coated healing precipitates is not shown clearly in the images. Processing the reconstructed images by accentuating the cracked region and comparing the reconstructed parts of the images was also no feasible as the images were too sensitive to the thresholding function because of their low quality.

The X-ray CT reconstruction however showed clearly how the cracks had propagated in the specimen as a result of the freeze cracking performed on the hollow cylindrical pipe section specimens. The reconstructed images we used to obtain a 3-D model of the cracked specimen which showed the clear pathways for water leaks.

SEM-EDS analysis performed on the different surfaces of the pipe section specimens showed the mechanism behind the calcite precipitate coating from running the healing solution through those specimens. The key findings are listed below

- The calcite coating on the specimens are found predominantly on the inner curved surface of the specimens. The cracked surfaces do not get coated with the precipitate as compared to the inner surface. These can be attributed to the amount of water flow these surfaces receive.

- The precipitation starts in the inner curved surface and closes the crack mouth of the radial crack in the cylindrical specimen starting from the inner surface. Once the crack mouth is closed the flow of water to the cracked surface completely stops and therefore the chances of precipitates forming are completely removed on the cracked surface.

6 CONCLUSION AND FUTURE WORK

6.1 Summary of dissertation

The research compiled in this dissertation was aimed towards the objective of attempting to repair/heal the failing water distribution systems in the country. With conventional repair being too expensive or not feasible due to other external limiting factors alternative methods were investigated. Self-healing techniques in concrete had been made prevalent in the past couple of decades and the techniques were used in this research to help achieve the objectives. Accelerated autogenous healing has been studied in recent years to provide healing effect in concrete exposed to water that has its calcium carbonate saturation index altered chemically. Accelerated autogenous healing was chosen as the technique to heal the damaged concrete pipe water distribution systems. Permeability of the pipe sections would be used as the metric for measuring damage in the system. Two types of damage were considered namely, cracking and decalcification of concrete.

The first part of the research was to establish the test methods for the permeability testing. Hollow Dynamic Pressurization (HDP) technique was used for poromechanical measurement and Radial Flow Through (RFT) technique was used for the accelerated flow through method. The measured permeabilities obtained from the poromechanical HDP method and the RFT method were compared for both cement paste, mortar and concrete. The two methods allow measurement of a material resistance to pressurized fluid flow *into* (HDP) and *through* (RFT) a sample. For the first time, it was shown that for mortars and concrete, the material resistance to these two different pressurized fluid flows are different. There was no difference in permeability measurements

observed between the two techniques for cement paste specimens. A significant difference between the resistance to permeation through and into the pore network of the mortar and concrete was observed. This was attributed to the connectivity established in the pipe section wall by interconnect ITZ sections in the case of mortar and concrete.

To test the healing of damaged specimens, controlled damage that could be replicated easily needed to be established. Different methods to achieve controlled cracking and controlled decalcification were used and the method which provided the most severe damage while retaining the stability of the hollow cylinder pipe section specimens were selected. Permeability of cracked sections were measured using RFT method and the permeability of decalcified specimens were measured using HDP method. The damaged specimens were then separated into 5 sets and then treated with four different healing solutions and a control solution using a healing rig for three days. Permeability of the healed samples were measured again with their respective techniques to measure the loss of permeability due to the healing effect. It was observed that the healing solutions super-saturated with calcium carbonate performed best towards helping the healing process.

The accelerated autogenous healing technique was shown to work helping reduce the damage in hollow cylindrical pipe section specimens. The mechanism behind the healing process was studied next. The hypothesis for the process was that the healing solutions precipitate calcite crystals on the surface of the specimens exposed to the water and thereby sealing the pores and cracks in the process. X-ray computed micro-tomography (CT) technique was used to obtain a 3-dimensional image of the cracked specimens before and after the healing was performed. The X-ray CT image resolution was too low to identify the calcite coating in the reconstructed images. Scanning

electron microscopy (SEM) was used in tandem with electron dispersive spectroscopy (EDS) on the inner surface and the cracked surfaces of the hollow cylindrical pipe section specimen. The SEM-EDS analysis showed the presence of calcite coating on the inner surface of the cylindrical specimen but no coating on the cracked surfaces. This lead to the conclusion that the coating happens on the inner surface and grows into the crack eventually closing the crack opening to seal it up from the inside of the pipe.

6.2 Dissertation conclusions

The primary objective of the research compiled in this dissertation was to investigate a method to repair/heal damage in concrete pipe water distribution systems autogenously without external effort or very minimal external effort. The secondary objective was to accomplish the primary objective with minimal disruption of the functioning of the water distribution systems. The objectives were achieved and the conclusions that could be drawn from the research are listed below:

- For cement pastes, the permeabilities measured using the poromechanical (HDP) and the accelerated flow (RFT) method are equivalent, indicating that the resistances to flow into and flow through cement paste are equivalent.

- For a mortar with an aggregate volume fraction of about 46%, the permeability measured via RFT was about an order of magnitude greater than that measured via HDP (which was equal to the paste permeability). This result indicates that the presence of the aggregates served to increase the flow through the material but did not significantly affect the flow

into the material. For concrete with an aggregate volume fraction of about 62% the permeability measured via RFT was greater than that measured via HDP (which was greater than the paste and mortar permeability). This result indicates that percolation of ITZ increases the flow into the material while the flow through the material is similar to that of mortar (pathways dominating the permeability).

- The difference in permeability when aggregates are introduced can be attributed to the interconnected ITZ forming a short circuit in the transport network. In mortars the ITZ is not fully percolated therefore the flow into permeability is still lower than the flow through permeability. In concrete where the ITZ is fully percolated the flow into permeability is greater than cement paste. However, by having more connected pathways in the ITZ due to the percolation the flow through permeability remains relatively high.

- The flow into permeability of cement mortar increases by up to a factor of 250 when decalcified by exposure to 6M ammonium nitrate solution. The permeability of the cement mortar specimen increases exponentially with increase of exposure time to the decalcifying reagent.

- The flow through permeability of cracked cement mortar samples increase by up to a factor of 38000 when cracked radially by freezing with the middle hole of the cylindrical specimen filled with water.

- Accelerated autogenous healing technique was able to reduce the permeability of cracked and decalcified hollow cylindrical cement mortar pipe section specimens.

- Four iterations of healing solutions were tested with varying degrees of saturation for calcium carbonate in the solutions. Solution 4 which was super saturated with calcium ions and calcium carbonate (12.5mg/L) showed the best results towards decreasing the permeability of the pipe section specimens.

- Cracked specimens that were healed with Solution 4 showed a permeability decrease of up to a factor of 12.5 measured using the Radial Flow Through test. Decalcified specimens that were healed with Solution 4 showed a permeability decrease of up to a factor of 3.5 measured using the Hollow Dynamic Pressurization test.

- The effect of altering potable water chemistry to induce accelerated autogenous healing in damage cement mortar has been investigated successfully proving that the method is a viable solution to achieve the primary objective of the research.

- X-ray CT analysis used to reconstruct 3d images of the cracked and healed specimens was unable to discern the calcite coating done in the cracked region by the healing process. Thus, leading to the conclusion that there is no coating in the cracked region or the coating thickness is small enough to not show up on the X-ray CT analysis.

- SEM – EDS analysis performed on the inner surfaces and cracked surfaces of the healed cylindrical specimens proved that the calcite coating from the accelerated autogenous healing is done primarily on the inner surface of the cylinder. There is very minimal or no deposition or coating of the precipitates on the cracked surface.

- The calcite coating precipitated by the autogenous healing was precipitated on the inner surface of the cylinder works by closing the crack mouth opening from the inside of the cylindrical pipe thereby reducing the permeability of the specimen and prevents water from leaking out of the pipes.

6.3 Summary of contributions

The research presented in this dissertation has several unique contributions to the field of civil engineering research. These contributions are listed out below

- The difference in permeability measurement between poromechanical and conventional methods for materials involving multimodal porous network had never been studied previously. The work done in this research explores the differences in detail and lists the differences and the uses for both the techniques used in permeability measurement.

- The use of external agents to trigger autogenous healing in concrete had not been explored before this research. This method does not rely on using the calcium hydroxide provided

by concrete hydration products and uses calcium ions and carbonate ions supplied to the water in the form of salts added to the healing solutions.

- The effect of decalcification on the flow into permeability of cementitious materials was documented in detail in this research.

- The high variability of low resolution X-ray CT images when compared with one another and its high sensitivity to thresholding effects were not documented previously and has been studied in detail in this research.

6.4 Future work

The research presented in this dissertation is investigative in nature and therefore was applied to miniaturized scale specimens. Future work is required to apply the findings of the research to practical use in concrete pipe water distribution systems. Some of the possible avenues for future research are

- *Investigate the effect of healing for greater periods of time.* The healing process in this study was done for a period of 3 days since the calcium carbonate content in the solution would be depleted by that time. Healing for greater periods of time could be done by replenishing the solution after specific periods of time to keep the ion supply in the solution needed for the calcite precipitation.

- *Investigate the effect of healing on larger scale specimens.* This study was focused on the healing mechanism and its viability. So highly miniaturized scale was used for the testing purposes as it facilitated faster tests and easier test setups. The next step would be to use the healing process on specimens of a larger scale to investigate the changes that would have to be adopted to use the technique on actual concrete pipe water distribution systems.

- *Investigate the stability of the healing precipitate.* This study proved that the healing precipitates reduce the permeability and heals the damage caused by decalcification and cracking. The long-term stability and durability of the precipitates is however unknown and further study has to be conducted on the topic to ensure that the healing leads to a lasting long-term solution for the concrete pipe water distribution systems.

- *Further in-depth study on the precipitation mechanism.* The mechanism behind the calcite precipitation was studied using the SEM-EDS and X-ray CT analysis. A more comprehensive study on the mechanism would help significantly in understanding the nature of the precipitation. This could be used tailor the precipitates based on the requirements of the system that is damaged.

- *Investigate the autogenous healing effects on regular structural members.* The accelerated autogenous healing technique proved to be successful in reducing permeability of pipe section specimens. Most reinforced concrete structures fail due to durability and serviceability related issues. The viability of the technique in sealing cracks and other

durability related issues for structural members like bridge girders, beams columns and slabs must be studied.

REFERENCES

1. Jackson, M.D., et al., *Mechanical resilience and cementitious processes in Imperial Roman architectural mortar.* Proceedings of the National Academy of Sciences, 2014. **111**(52): p. 18484-18489.
2. Aldea, C.-M., S.P. Shah, and A. Karr, *Permeability of cracked concrete.* Materials and Structures, 1999. **32**(5): p. 370-376.
3. Aldea, C.-M., S.P. Shah, and A. Karr, *Effect of cracking on water and chloride permeability of concrete.* Journal of materials in civil engineering, 1999. **11**(3): p. 181-187.
4. Gérard, B., et al., *Cracking and permeability of concrete under tension.* Materials and Structures, 1996. **29**(3): p. 141-151.
5. Hearn, N., *Effect of shrinkage and load-induced cracking on water permeability of concrete.* Materials Journal, 1999. **96**(2): p. 234-241.
6. Phung, Q.T., et al., *Microstructural and permeability changes due to accelerated Ca leaching in ammonium nitrate solution.* Concrete Solutions 2014, 2014: p. 431.
7. De Rooij, M., et al., *Self-healing phenomena in cement-based materials.* Draft of State-of-the-Art report of RILEM Technical Committee, 2011.
8. Hearn, N., *Self-sealing, autogenous healing and continued hydration: What is the difference?* Materials and Structures, 1998. **31**(8): p. 563.
9. Zhong, W. and W. Yao, *Influence of damage degree on self-healing of concrete.* Construction and building materials, 2008. **22**(6): p. 1137-1142.
10. Moore, N.C. and V. Li, *Self-healing concrete.* 2009.

11. Vandine, R., C. West, and M. Hansen. *Self-Healing Concrete*. in *Sixth International Conference on Concrete under Severe Conditions: Environment and Loading*. 2010.

12. Wang, J., et al., *Self-healing concrete by use of microencapsulated bacterial spores.* Cement and Concrete Research, 2014. **56**: p. 139-152.

13. Li, V.C. and E. Herbert, *Robust self-healing concrete for sustainable infrastructure.* Journal of Advanced Concrete Technology, 2012. **10**(6): p. 207-218.

14. Wang, J., et al., *Use of silica gel or polyurethane immobilized bacteria for self-healing concrete.* Construction and building materials, 2012. **26**(1): p. 532-540.

15. Bundur, Z.B., M.J. Kirisits, and R.D. Ferron, *Biomineralized cement-based materials: Impact of inoculating vegetative bacterial cells on hydration and strength.* Cement and Concrete research, 2015. **67**: p. 237-245.

16. Başaran Bundur, Z., et al., *Biomineralization in Self-Healing Cement-Based Materials: Investigating the Temporal Evolution of Microbial Metabolic State and Material Porosity.* Journal of Materials in Civil Engineering, 2017. **29**(8): p. 04017079.

17. Williams, S.L., M.J. Kirisits, and R.D. Ferron, *Influence of concrete-related environmental stressors on biomineralizing bacteria used in self-healing concrete.* Construction and Building Materials, 2017. **139**: p. 611-618.

18. De Muynck, W., et al., *Bacterial carbonate precipitation improves the durability of cementitious materials.* Cement and concrete Research, 2008. **38**(7): p. 1005-1014.

19. Jonkers, H.M., et al., *Application of bacteria as self-healing agent for the development of sustainable concrete.* Ecological engineering, 2010. **36**(2): p. 230-235.

20. Jonkers, H.M. and E. Schlangen, *Self-healing of cracked concrete: a bacterial approach.* Proceedings of FRACOS6: fracture mechanics of concrete and concrete structures. Catania, Italy, 2007: p. 1821-1826.

21. Han, B., L. Zhang, and J. Ou, *Self-Healing Concrete*, in *Smart and Multifunctional Concrete Toward Sustainable Infrastructures*. 2017, Springer. p. 117-155.

22. Edvardsen, C., *Water permeability and autogenous healing of cracks in concrete.* ACI Materials Journal-American Concrete Institute, 1999. **96**(4): p. 448-454.

23. Phillips, M., *Healed concrete is strong.* Concrete, 1925. **10**: p. 36.

24. Lauer, K.R. *Autogenous healing of cement paste*. in *Journal Proceedings*. 1956.

25. Munday, J., C. Sangha, and R. Dhir, *Comparative study of autogenous healing of different concretes*. 1976.

26. Clear, C., *The effects of autogenous healing upon the leakage of water through cracks in concrete*. 1985.

27. Yang, Y., et al., *Autogenous healing of engineered cementitious composites under wet–dry cycles.* Cement and Concrete Research, 2009. **39**(5): p. 382-390.

28. Parks, J., et al., *Effects of bulk water chemistry on autogenous healing of concrete.* Journal of Materials in Civil Engineering, 2010. **22**(5): p. 515-524.

29. Edwards, M., J.L. Parks, and P.J. Vikesland. *Autogenous Healing of Concrete.* in *American Water Works Association Water Quality Technology Conference.* 2005. Quebec City, Canada.

30. Ulm, F.-J., J.-M. Torrenti, and F. Adenot, *Chemoporoplasticity of calcium leaching in concrete.* Journal of Engineering Mechanics, 1999. **125**(10): p. 1200-1211.

31. Von Beton, T.D.A., E.L.T.E. LA RELATION, and L. LIXIVATION, *Leaching of concrete under thermal influence.* Otto-Graf-Journal, 2001. **12**: p. 51.

32. Gérard, B., C. Le Bellego, and O. Bernard, *Simplified modelling of calcium leaching of concrete in various environments.* Materials and Structures, 2002. **35**(10): p. 632-640.

33. Nguyen, V., et al., *A separation of scales homogenization analysis for the modelling of calcium leaching in concrete.* Computer Methods in Applied Mechanics and Engineering, 2006. **195**(52): p. 7196-7210.

34. Kurdowski, W., *The protective layer and decalcification of CSH in the mechanism of chloride corrosion of cement paste.* Cement and Concrete Research, 2004. **34**(9): p. 1555-1559.

35. Brown, P., R. Hooton, and B. Clark, *Microstructural changes in concretes with sulfate exposure.* Cement and Concrete Composites, 2004. **26**(8): p. 993-999.

36. Carde, C., G. Escadeillas, and A. François, *Use of ammonium nitrate solution to simulate and accelerate the leaching of cement pastes due to deionized water.* Magazine of Concrete Research, 1997. **49**(181): p. 295-301.

37. Hooton, R.D., *Permeability and pore structure of cement pastes containing fly ash, slag, and silica fume,* in *Blended cements*. 1986, ASTM International.

38. Ye, G., P. Lura, and v.K. van Breugel, *Modelling of water permeability in cementitious materials.* Materials and Structures, 2006. **39**(9): p. 877-885.

39. El-Dieb, A. and R. Hooton, *A high pressure triaxial cell with improved measurement sensitivity for saturated water permeability of high performance concrete.* Cement and concrete research, 1994. **24**(5): p. 854-862.

40. Hearn, N. and R. Mills, *A simple permeameter for water or gas flow.* Cement and Concrete Research, 1991. **21**(2-3): p. 257-261.

41. Scherer, G.W., J.J. Valenza, and G. Simmons, *New methods to measure liquid permeability in porous materials.* Cement and concrete research, 2007. **37**(3): p. 386-397.

42. Scherer, G.W., *Measuring Permeability of Rigid Materials by a Beam-Bending Method: I, Theory.* Journal of the American Ceramic Society, 2000. **83**(9): p. 2231-2239.

43. Vichit-Vadakan, W. and G.W. Scherer, *Measuring permeability and stress relaxation of young cement paste by beam bending.* Cement and concrete research, 2003. **33**(12): p. 1925-1932.

44. Vichit-Vadakan, W. and G.W. Scherer, *Measuring Permeability of Rigid Materials by a Beam-Bending Method: II, Porous Glass.* Journal of the American Ceramic Society, 2000. **83**(9): p. 2240-2246.

45. Vichit-Vadakan, W. and G.W. Scherer, *Measuring Permeability of Rigid Materials by a Beam-Bending Method: III, Cement Paste.* Journal of the American Ceramic Society, 2002. **85**(6): p. 1537-1544.

46. Ai, H., J.F. Young, and G.W. Scherer, *Thermal expansion kinetics: method to measure permeability of cementitious materials: II, application to hardened cement pastes.* Journal of the American Ceramic Society, 2001. **84**(2): p. 385-91.

47. Ciardullo, J., D. Sweeney, and G. Scherer, *Thermal expansion kinetics: Method to measure permeability of cementitious materials, IV. Effect of thermal gradients and viscoelasticity.* Journal of the American Ceramic Society, 2005. **88**(5): p. 1213-1221.

48. Scherer, G.W., *Thermal expansion kinetics: method to measure permeability of cementitious materials: I, theory.* Journal of the American Ceramic Society, 2000. **83**(11): p. 2753-2761.

49. Gross, J. and G.W. Scherer, *Dynamic pressurization: novel method for measuring fluid permeability.* Journal of non-crystalline solids, 2003. **325**(1): p. 34-47.

50. Scherer, G.W., *Dynamic pressurization method for measuring permeability and modulus: I. Theory.* Materials and Structures, 2006. **39**(10): p. 1041-1057.

51. Grasley, Z., et al., *Dynamic pressurization method for measuring permeability and modulus: II. cementitious materials.* Materials and Structures, 2007. **40**(7): p. 711-721.

52. Scherer, G.W., *Poromechanics analysis of a flow-through permeameter with entrapped air.* Cement and Concrete Research, 2008. **38**(3): p. 368-378.

53. Jones, C.A. and Z.C. Grasley, *Correlation of hollow and solid cylinder dynamic pressurization tests for measuring permeability.* Cement and Concrete Research, 2009. **39**(4): p. 345-352.

54. Jones, C.A. and Z.C. Grasley, *Comparison of Dynamic Pressurization (DP) Measurement of Permeability Versus Flow-Through Measurement for Permeability of Cementitious Materials*. 2008.

55. Jones, C.A. and Z.C. Grasley. *Measuring concrete permeability using dynamic pressurization: achieving saturation*. in *2009 NRMCA Concrete Technology Forum*. 2009. Cincinnati, OH: National Ready Mix Concrete Association.

56. Bhargava, A. and N. Banthia, *Measurement of concrete permeability under stress.* Experimental Techniques, 2006. **30**(5): p. 28-31.

57. Hoseini, M., V. Bindiganavile, and N. Banthia, *The effect of mechanical stress on permeability of concrete: a review.* Cement and Concrete Composites, 2009. **31**(4): p. 213-220.

58. El-Dieb, A. and R. Hooton, *Water-permeability measurement of high performance concrete using a high-pressure triaxial cell.* Cement and Concrete Research, 1995. **25**(6): p. 1199-1208.

59. Jones, C.A. and Z.C. Grasley, *Novel and flexible dual permeability measurement device for cementitious materials.* ACI Materials Journal, 2009. **106**(2).

60. Landis, E.N. and D.T. Keane, *X-ray microtomography.* Materials Characterization, 2010. **61**(12): p. 1305-1316.

61. Lenoir, N., et al., *Volumetric digital image correlation applied to X-ray microtomography images from triaxial compression tests on argillaceous rock.* Strain, 2007. **43**(3): p. 193-205.

62. Cnudde, V. and M.N. Boone, *High-resolution X-ray computed tomography in geosciences: A review of the current technology and applications.* Earth-Science Reviews, 2013. **123**: p. 1-17.

63. You, Z., S. Adhikari, and M.E. Kutay, *Dynamic modulus simulation of the asphalt concrete using the X-ray computed tomography images.* Materials and Structures, 2009. **42**(5): p. 617-630.

64. Brooks, R.A. and G. Di Chiro, *Beam hardening in x-ray reconstructive tomography.* Physics in medicine and biology, 1976. **21**(3): p. 390.

65. Garboczi, E.J., *Three-dimensional mathematical analysis of particle shape using X-ray tomography and spherical harmonics: Application to aggregates used in concrete.* Cement and concrete research, 2002. **32**(10): p. 1621-1638.

66. Stock, S., et al., *X-ray microtomography (microCT) of the progression of sulfate attack of cement paste.* Cement and Concrete Research, 2002. **32**(10): p. 1673-1675.

67. Wang, L., et al., *Quantification of damage parameters using X-ray tomography images.* Mechanics of Materials, 2003. **35**(8): p. 777-790.

68. De Graef, B., et al., *A sensitivity study for the visualisation of bacterial weathering of concrete and stone with computerised X-ray microtomography.* Science of the total environment, 2005. **341**(1): p. 173-183.

69. Rattanasak, U. and K. Kendall, *Pore structure of cement/pozzolan composites by X-ray microtomography.* Cement and concrete research, 2005. **35**(4): p. 637-640.

70. Gallucci, E., et al., *3D experimental investigation of the microstructure of cement pastes using synchrotron X-ray microtomography (μCT).* Cement and Concrete Research, 2007. **37**(3): p. 360-368.

71. Provis, J.L., et al., *X-ray microtomography shows pore structure and tortuosity in alkali-activated binders.* Cement and Concrete Research, 2012. **42**(6): p. 855-864.

72. Flannery, B.P., et al., *Three-dimensional x-ray microtomography.* Science, 1987. **237**(4821): p. 1439-1444.

73. Deckman, H.W., et al., *Development of quantitative X-ray microtomography.* Mater. Res. Soc. Symp. Proc., 1991. **217**: p. 97-110.

74. Kinney, J.H. and M.C. Nichols, *X-ray tomographic microscopy (XTM) using synchrotron radiation.* Annual Review of Materials Science, 1992. **22**(1): p. 121-152.

75. Knoll, M., *Aufladepotentiel und sekundäremission elektronenbestrahlter körper.* Z. tech. Phys, 1935. **16**: p. 467-475.

76. Von Ardenne, M., *Improvements in electron microscopes.* British patent, 1937(511204).

77. Danilatos, G., *Foundations of environmental scanning electron microscopy.* Advances in electronics and electron physics, 1988. **71**: p. 109-250.

78. Reichelt, R., *Scanning electron microscopy*, in *Science of microscopy*. 2007, Springer. p. 133-272.

79. Asaad, W. and E. Burhop, *The K Auger Spectrum.* Proceedings of the Physical Society, 1958. **71**(3): p. 369.

80. Burhop, E. and W. Asaad, *The Auger Effect.* Advances in Atomic and Molecular Physics, 1972. **8**: p. 163-284.

81. Åberg, T. and G. Howat, *Theory of the Auger effect.* Handbuch der Physik, 1982. **31**: p. 469-619.

82. Brandt, W., R. Laubert, and I. Sellin, *Characteristic X-Ray Production in Magnesium, Aluminum, and Copper by Low-Energy Hydrogen and Helium Ions.* Physical Review, 1966. **151**(1): p. 56.

83. Cherns, D., A. Howie, and M. Jacobs, *Characteristic X-ray production in thin crystals.* Zeitschrift für Naturforschung A, 1973. **28**(5): p. 565-576.

84. Cliff, G. and G.W. Lorimer, *The quantitative analysis of thin specimens.* Journal of Microscopy, 1975. **103**(2): p. 203-207.

85. Bederson, B. and L. Kieffer, *Total Electron—Atom Collision Cross Sections at Low Energies—A Critical Review.* Reviews of Modern Physics, 1971. **43**(4): p. 601.

86. Bai, J., et al., *The BES upgrade.* Nuclear Instruments and Methods in Physics Research Section A: Accelerators, Spectrometers, Detectors and Associated Equipment, 2001. **458**(3): p. 627-637.

87. Yuan, L., et al., *Ethylene flame synthesis of well-aligned multi-walled carbon nanotubes.* Chemical physics letters, 2001. **346**(1): p. 23-28.

88. Jones, C. and Z. Grasley, *Correlation of Radial Flow-Through and Hollow Cylinder Dynamic Pressurization Test for Measuring Permeability.* Journal of Materials in Civil Engineering, 2009. **21**(10): p. 594-600.

89. Elmer, T.H., *Porous and reconstructed glasses.* ASM International, Engineered Materials Handbook., 1991. **4**: p. 427-432.

90. Chen, X., S. Wu, and J. Zhou, *Influence of porosity on compressive and tensile strength of cement mortar.* Construction and Building Materials, 2013. **40**: p. 869-874.

91. Lafhaj, Z., et al., *Correlation between porosity, permeability and ultrasonic parameters of mortar with variable water / cement ratio and water content.* Cement and Concrete Research, 2006. **36**(4): p. 625-633.

92. Narayanan, N. and K. Ramamurthy, *Structure and properties of aerated concrete: a review.* Cement and Concrete Composites, 2000. **22**(5): p. 321-329.

93. Scrivener, K.L., A.K. Crumbie, and P. Laugesen, *The Interfacial Transition Zone (ITZ) Between Cement Paste and Aggregate in Concrete.* Interface Science. **12**(4): p. 411-421.

94. Shane, J.D., et al., *Effect of the interfacial transition zone on the conductivity of Portland cement mortars.* Journal of the American Ceramic society, 2000. **83**(5): p. 1137-1144.

95. Wang, R., P.-M. Wang, and X.-G. Li, *Physical and mechanical properties of styrene–butadiene rubber emulsion modified cement mortars.* Cement and Concrete Research, 2005. **35**(5): p. 900-906.

96. Bentz, D.P., *Influence of internal curing using lightweight aggregates on interfacial transition zone percolation and chloride ingress in mortars.* Cement and concrete composites, 2009. **31**(5): p. 285-289.

97. Coussy, O., *Poromechanics*. 2004: John Wiley & Sons.

98. Grasley, Z.C., *Measuring and modeling the time-dependent response of cementitious materials to internal stresses*. 2006, University of Illinois at Urbana-Champaign.

99. Sant, G., *Effect of Inclusions in Diffusion Rates in Cementitious Materials*. 2016.

100. *Standard Practice for Mechanical Mixing of Hydraulic Cement Pastes and Mortars of Plastic Consistency*. ASTM International.

101. Bazant, Z.P., S. Sener, and J.-K. Kim, *Effect of cracking on drying permeability and diffusivity of concrete.* ACI materials journal, 1987. **84**(5): p. 351-357.

APPENDIX A

MATHEMATICA CODE FOR HDP PERMEABILITY CALCULATION

```
(*Input Parameters*)

Pa = 6894.757 * (1164);(*applied pressure change, Pa*)

Kl = 2.2 * 10^9;(*Bulk modulus of the liquid used, Pa*)

e0 = 90 * 10^-6;(*initial peak strain*)

e∞ = 20 * 10^-6;(*final strain after completion of test*)

ϕ = 0.25;(*porosity of the specimen*)

ν = 0.2;(*poissons ratio*)

R0 = 0.0254 * 0.5;(*outer radius, m*)

Ri = 0.0254 * 2 / 16;(*inner radius, m*)

ηl = 0.89 * 10^-3;
(*dynamic viscosity of water at 25deg C*)
```

(*Calculations*)

$$Ks = \frac{Pa}{3 * e\infty};$$ (*bulk modulus of solids, Pa*)

$$Kp = Ks * \frac{\phi - \left(\frac{e0}{e\infty} + \phi - 1\right) * \frac{Kl}{Ks}}{\frac{e0}{e\infty}\phi - \left(\frac{e0}{e\infty} + \frac{e0}{e\infty}\phi - 1\right) * \frac{Kl}{Ks}};$$ (*bulk modulus of the porous body, Pa*)

$$b = 1 - \frac{Kp}{Ks};$$ (*biot coefficient*)

$$M = \frac{Kl * Ks}{(Ks * \phi) + (Kl * (b - \phi))};$$ (*biot modulus*)

$$\lambda = \frac{M * b}{\left(M * b^2 + Kp\right)};$$

$$\beta = \frac{1 + \nu}{3 - 3 * \nu};$$

$$m = 5.6152 * \left(\frac{R0}{Ri}\right)^{-0.19623};$$

$$n = 0.40086 + 0.0056243 * Log\left[\left(\frac{R0}{Ri}\right)^{1.8506}\right];$$

$$\Omega = Simplify\left[E^{\frac{4}{N[\pi]^{1/2}} * (1 - b * \lambda * (1 - \beta)) * \left(\frac{(t/\tau v)^m - \sqrt{(t/\tau v)}}{1 - (t/\tau v)^n}\right)}\right];$$

model = Simplify[e∞ + (e0 − e∞) * Ω]; (*model used to curve fit the strain change*)

$$k = \frac{\eta l * (R0 - Ri)^2}{\tau v} * \left(\frac{\beta * b^2}{Kp} + \frac{1}{M}\right)$$ (*intrinsic permeability of sample*)

```
Data = Import[SystemDialogInput["FileOpen"], "Table"];

DataFinal = Data /. {x_, y_} → {x, -0.000001 y};
(*Note that the negative sign in the {} is only needed if your data is negative strain*)

ListPlot[DataFinal]

fit = FindFit[DataFinal, model, {τv}, t]

modelfitted = Evaluate[model /. fit]

Plot[modelfitted, {t, 0, 4000}]

(*hydrodynamic retardation time (fit parameter)*)
Show[Plot[modelfitted, {t, 0, 4000}], ListPlot[DataFinal], PlotRange → All]

(*permeability of the specimen, in nm^2*)
Evaluate[(k /. fit) * 10^18]
```

APPENDIX B

SEM IMAGES OF CALCITE COATED SURFACES

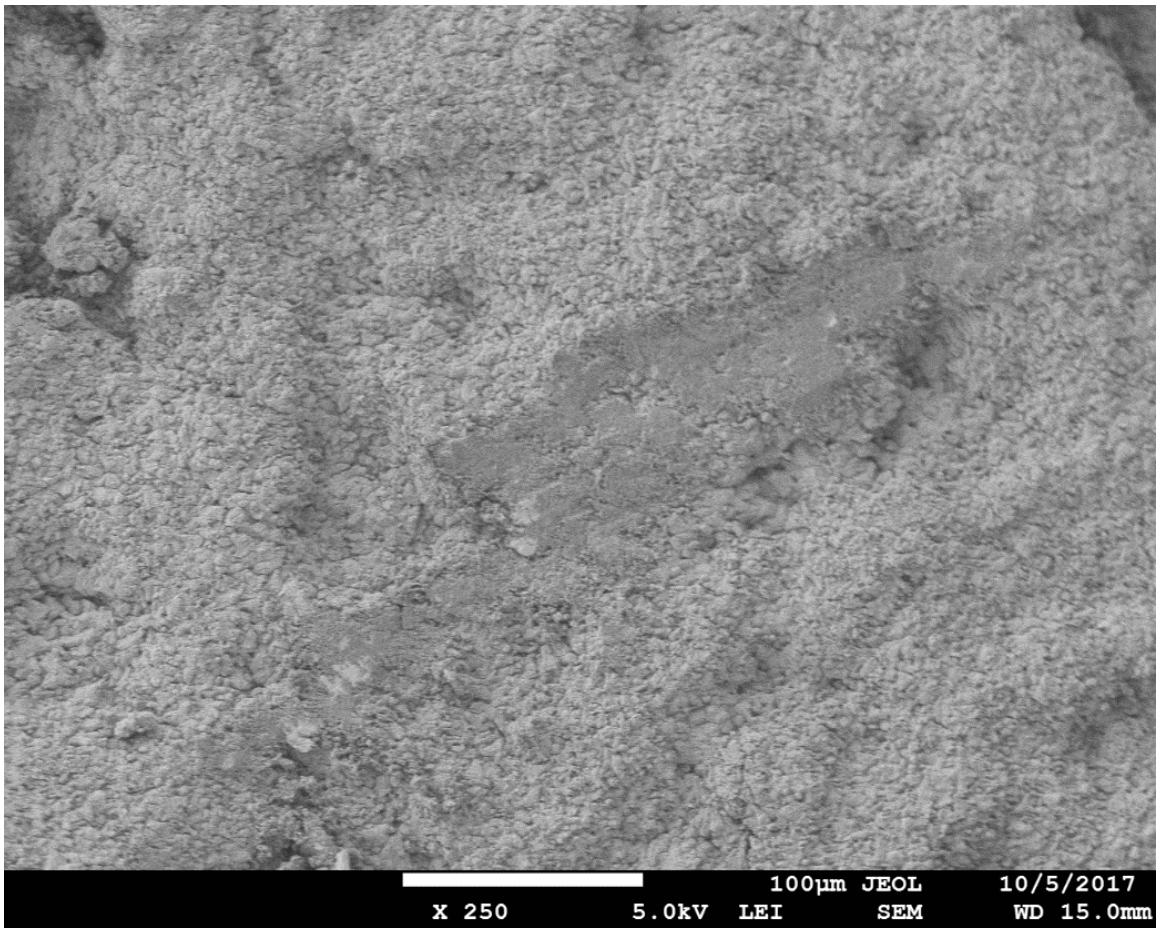

Figure 58 – SEM image of the calcite coated surface zoomed at x250

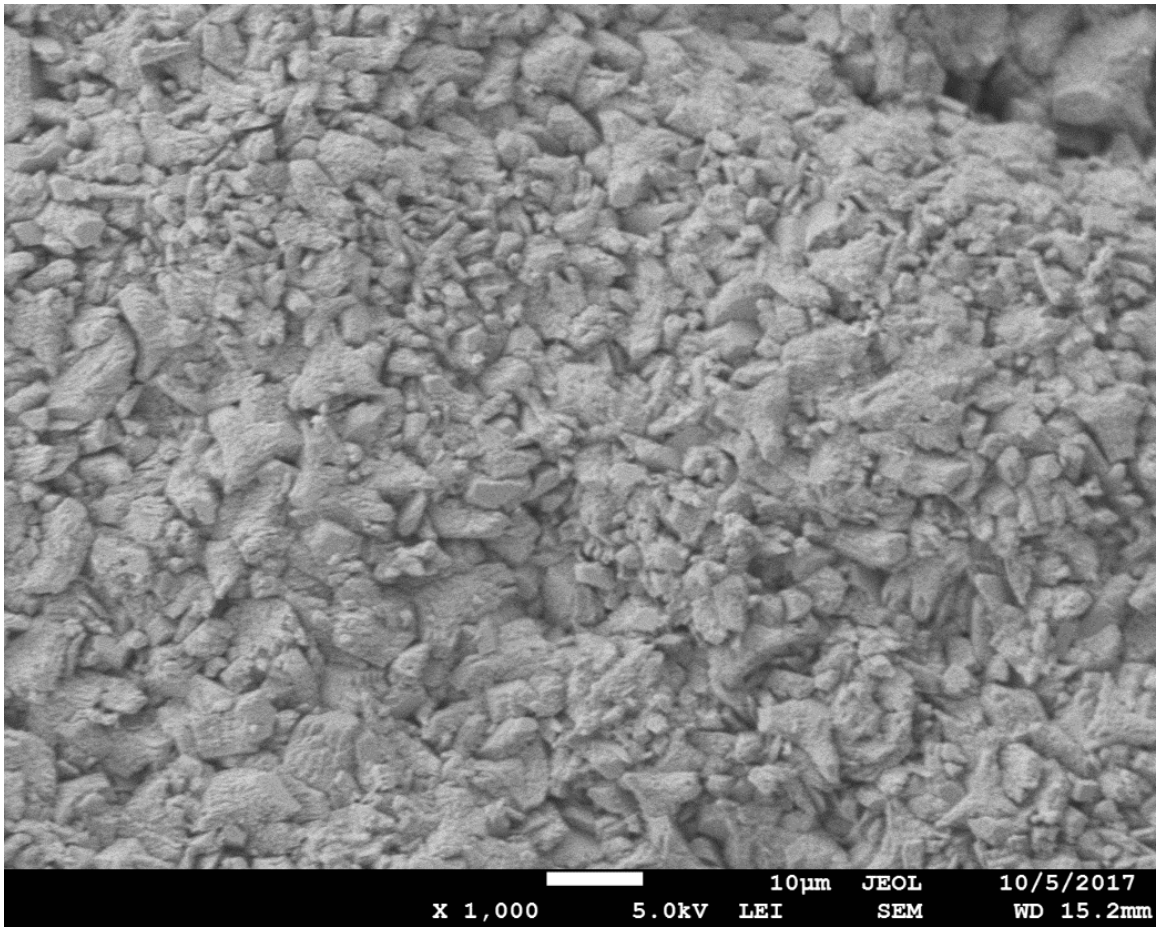

Figure 59 – SEM image of the calcite coated surface zoomed at x1000

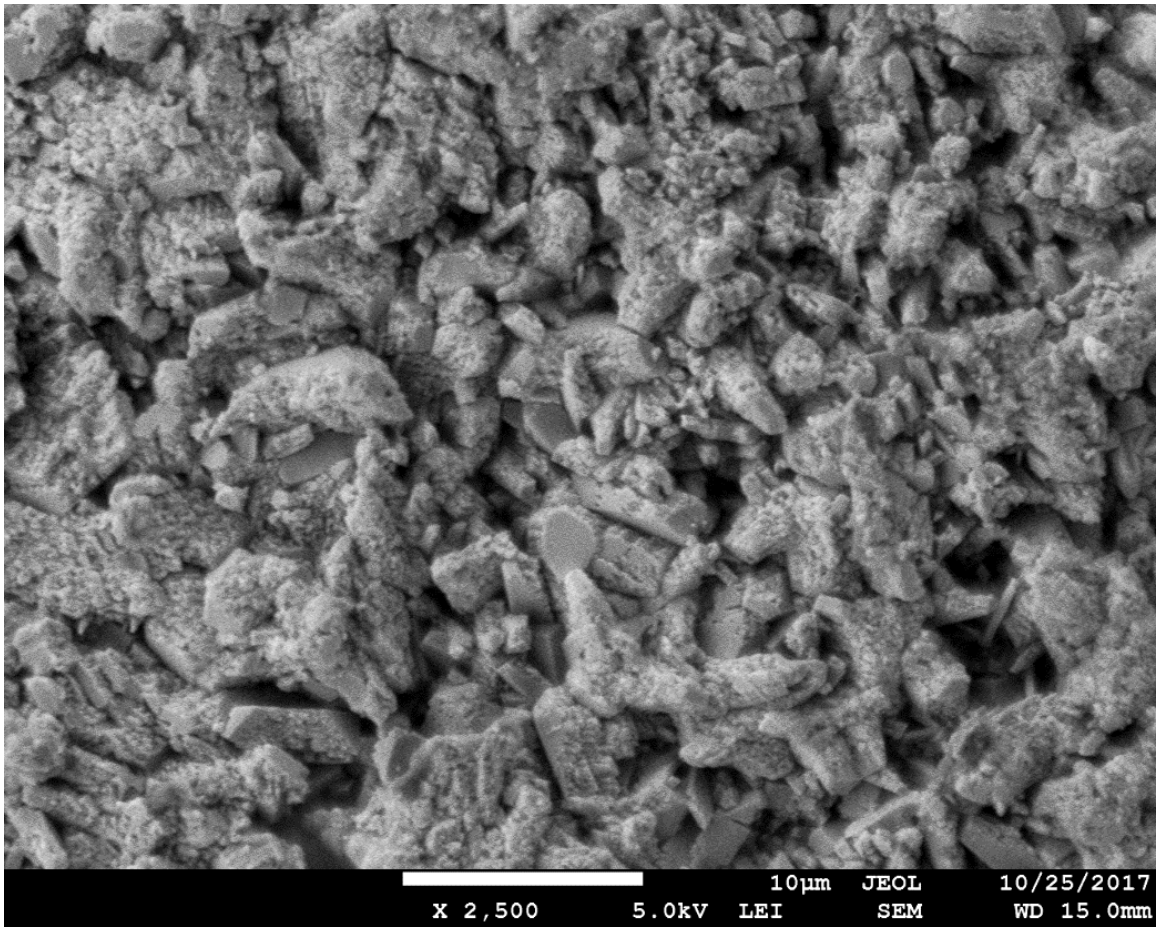

Figure 60 – SEM image of the calcite coated surface zoomed at x2500

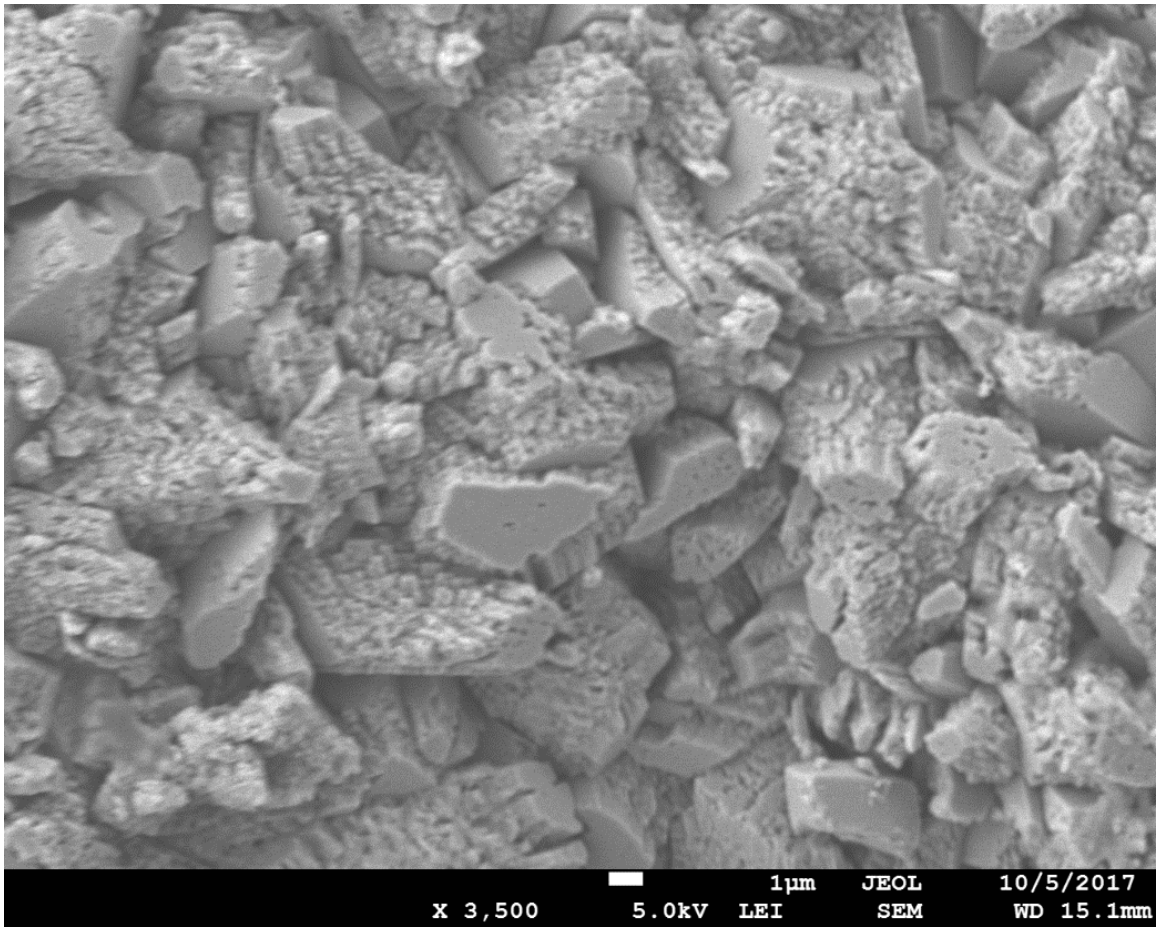

Figure 61 – SEM image of the calcite coated surface zoomed at x3500

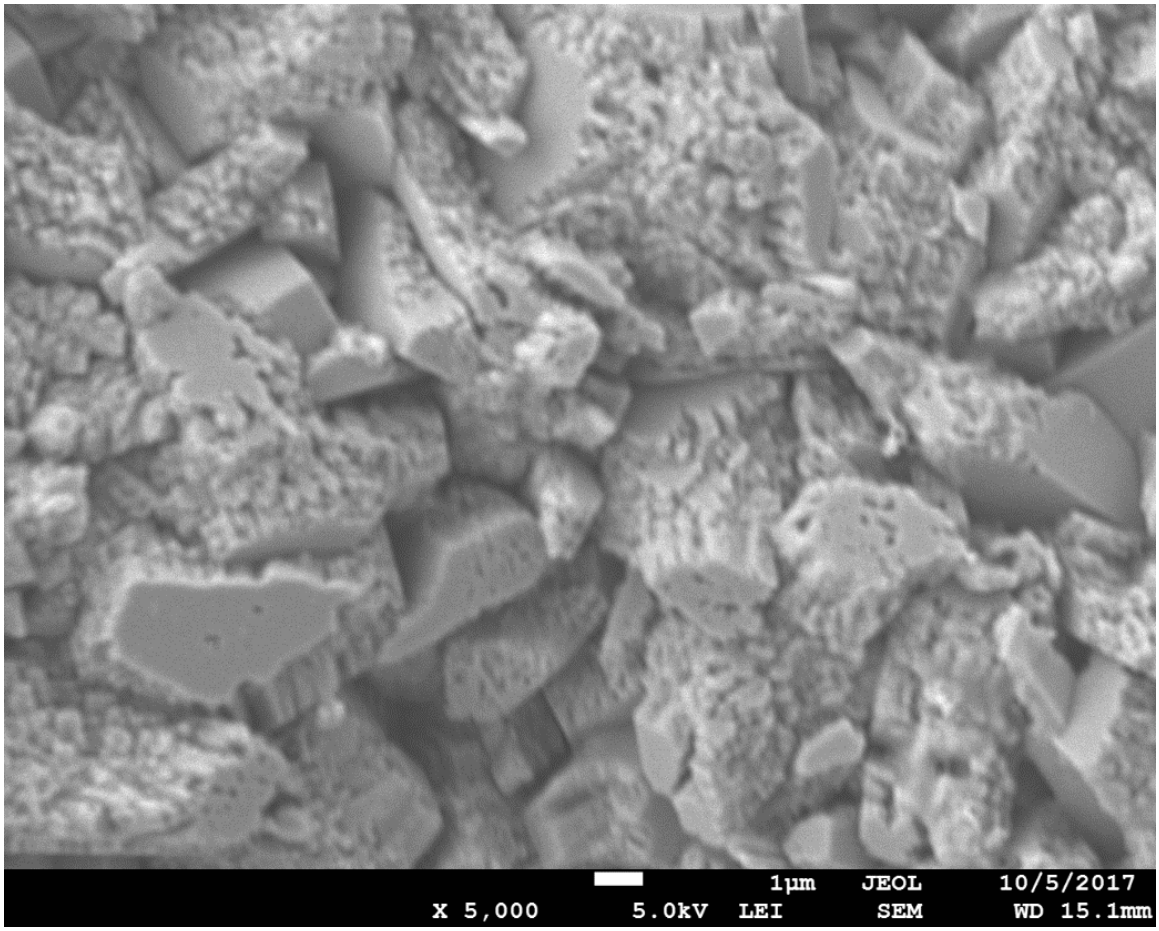

Figure 62 – SEM image of the calcite coated surface zoomed at x5000

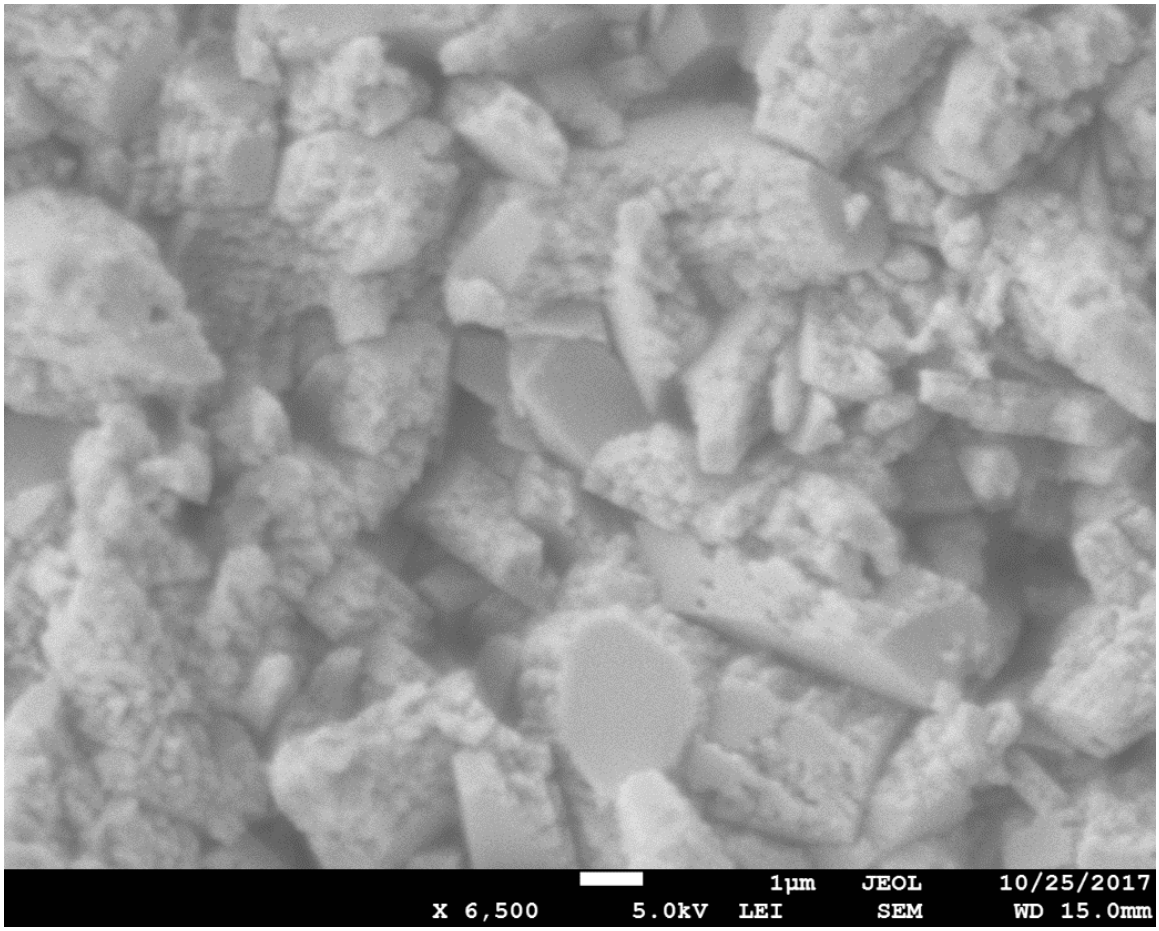

Figure 63 – SEM image of the calcite coated surface zoomed at x6500